Research Square

Preprints are preliminary reports that have not undergone peer review.
They should not be considered conclusive, used to inform clinical practice,
or referenced by the media as validated information.

Estrogen-triggered neutrophil extracellular traps fuel sterile inflammation via NKCC1

Yang Sun

yangsun@nju.edu.cn

Nanjing University https://orcid.org/0000-0003-1425-0089

Jiao Qu

Nanjing University

Wen Fang

Nanjing University

Tao Zhang

Nanjing University

Wei Liu

The State Key Laboratory of Pharmaceutical Biotechnology and MOE Key Laboratory of Model Animals for Disease Study, Model Animal Research Center, Medical School of Nanjing University, Nanjing, China

Yan Ding

Nanjing University

Songjun Liu

Tongde Hospital of Zhejiang Province Affiliated to Zhejiang Chinese Medical University College of Integrated Traditional Chinese and Western Medicine Clinical Medicine

Xinran Cao

Nanjing University

Ning Wan

China Pharmaceutical University https://orcid.org/0000-0003-3314-3967

Hui Ye

China Pharmaceutical University https://orcid.org/0000-0002-7416-1558

Xianjia Qi

Shanghai XuRan Biotechnology Co., Ltd., 1088 Zhongchun Road, Shanghai 201109, China

Tian Xu

Affiliated Hospital of Nanjing University of Chinese Medicine

Yan Li

Nanjing University https://orcid.org/0000-0001-7612-3953

Dijun Chen

Nanjing University https://orcid.org/0000-0002-7456-2511

Wen Lv

Tongde Hospital of Zhejiang Province Affiliated to Zhejiang Chinese Medical University

Qiang Xu

Nanjing University

Article

Keywords: neutrophil extracellular traps; aseptic inflammation; estrogen; NKCC1; endometrial hyperplasia

Posted Date: November 6th, 2026

DOI: https://doi.org/10.21203/rs.3.rs-11368963/v1

License: This work is licensed under a Creative Commons Attribution 4.0 International License. Read Full License

Additional Declarations: There is **NO** Competing Interest.

Estrogen-triggered neutrophil extracellular traps fuel sterile inflammation via NKCC1

Jiao Qu[1#,*], Wen Fang[1#], Tao Zhang[1,2#], Wei Liu[3#], Yan Ding[1], Songjun Liu[4], Xinran Cao[1], Ning Wan[5], Hui Ye[5], Xianjia Qi[6], Tian Xu[7], Qiang Xu[1], Yan Li[3]*, Dijun Chen[1]*, Yang Sun[1,2]*, Wen Lv[4]*

[1]State Key Laboratory of Pharmaceutical Biotechnology and Nanjing Drum Tower Hospital, School of Life Sciences, Chemistry and Biomedicine Innovation Center, Nanjing University, 163 Xianlin Avenue, Nanjing 210023, China; [2]Jiangsu Key Laboratory of New Drug Research and Clinical Pharmacy, Xuzhou Medical University, Xuzhou 221004, China; [3]State Key Laboratory of Pharmaceutical Biotechnology and MOE Key Laboratory of Model Animals for Disease Study, National Resource Center for Mutant Mice, Chemistry and Biomedicine Innovation Center, Model Animal Research Center, Medical School of Nanjing University, Nanjing, China; [4]Department of Gynecology, Tongde Hospital of Zhejiang Province Affiliated to Zhejiang Chinese Medical University (College of Integrated Traditional Chinese and Western Medicine Clinical Medicine), 234 Gucui Road, Hangzhou, 310012, China;[5]State Key Laboratory of Natural Medicines, China Pharmaceutical University, Nanjing 210009, China; [6]Shanghai XuRan Biotechnology Co., Ltd., 1088 Zhongchun Road, Shanghai 201109, China; [7]Affiliated Hospital of Nanjing University of Chinese Medicine, 155 Hanzhong Road, Nanjing 210029, China.

[#]These authors contributed equally to this work.

Running title: Estrogen-triggered NETs fuel sterile inflammation via NKCC1

* Corresponding to

Yang Sun, Ph.D., Professor, Dijun Chen, Ph.D., Associate Professor or Yan Li, Ph.D., Professor

Nanjing University, Nanjing 210023 China, Tel/Fax: +86-25-89687620;

Email: yangsun@nju.edu.cn (Y. Sun) , dijunchen@nju.edu.cn (D. Chen), or yanli@nju.edu.cn (Y. Li)

Wen Lv, Ph.D., Professor

Department of Gynecology, Tongde Hospital of Zhejiang, Hangzhou 310012 China

Email: 20168156@zcmu.edu.cn (W. Lv)

Abstract

Disorders of the menstrual cycle or exposure to external pathogens lead to uterus-related diseases, such as endometrial hyperplasia (EH) and endometritis (EN). We constructed a multiomics method to compare the molecular differences between estrogen-induced hyperplastic endometrium and infection-triggered inflammatory endometrium at the single-cell level. A unique neutrophil subpopulation that expresses Estrogen Receptor 1 (*ESR1*) was newly identified to be involved in EH development. Distinct from the infectious state, estrogen-induced NETs were mainly a consequence of ERα binding to *HMGN2*. Mechanistically, NETs could bind to NKCC1 and promote imbalance of ion homeostasis in endometrial epithelial cells, leading to cell proliferation and EH. Pharmacologically, aspirin was found to inhibit NET formation and alleviated EH in a nonhuman primate model by directly acetylating at K64 and K82 of HMGN2. Collectively, this study highlights neutrophil heterogeneity in sterile inflammation or infectious inflammation, providing a novel nonhormonal treatment strategy for the patients with estrogen abnormalities.

Key words: neutrophil extracellular traps; aseptic inflammation; estrogen; NKCC1; endometrial hyperplasia

Significance Statement

In this study, we compared the cellular and molecular difference of neutrophil extracellular trap (NET) formation between infection-driven inflammatory

endometrium (infectious inflammation) and estrogen-induced hyperplastic endometrium (aseptic inflammation) by multiomics analyses at the single-cell level. A unique neutrophil subpopulation was newly identified to be involved in estrogen-driven NET formation. Distinct from infectious state, estrogen-induced NETs were mainly consequent from ERα binding to HMGN2 and TIMM8B. Functionally, the ablation or inhibition of NETs significantly ameliorated endometrial hyperplasia (EH) in mouse model. Mechanistically, NETs bind to NKCC1 (encoded by Slc12a2) in unciliated epithelial cells and promote cell proliferation. Pharmacologically, a classic drug aspirin was screened to inhibit NET formation and confirmed to alleviate hyperplasia in a nonhuman primate EH model. This treatment regimen proposes a non-hormonal therapeutic strategy for endometrial hyperplasia.

Introduction

Both sterile inflammation and infectious inflammation contribute to disease progression [1, 2]. The pathogenic inflammatory microenvironment is complex and heterogeneous. Understanding the distinction between sterile inflammation and infectious inflammation is critically important for the development of new therapeutic approaches that better manage the potential effects of sterile inflammation and infectious inflammation on disease progression.

The uterus, the largest female reproductive organ, has many important functions, including the menstrual cycle and offspring production [3]. Disorders of the menstrual

cycle or exposure to external pathogens may lead to various uterus-related diseases, such as endometrial hyperplasia (EH, sterile inflammation) and endometritis (EN, bacterial infectious inflammation) [4, 5]. The progression of atypical EH to endometrial carcinoma poses a clinical concern [6]. According to previous reports, the EH and EN processes are accompanied by substantial alterations in the immune microenvironment [7, 8]. A recent study reported a single-cell transcriptomic analysis of the human endometrium during the menstrual cycle, shedding light on this essential physiological process [9]. However, the important impact of immune microenvironment changes on uterine-related diseases, especially on EH, remains unknown. Advances in single-cell multiomics sequencing technologies have allowed the identification of cellular heterogeneity in various diseases [10]. Here, we identified neutrophil heterogeneity by analyzing the differences between EH and EN using single-cell multiomics sequencing.

Neutrophil extracellular traps (NETs) have been identified as innate immune response effectors that bind microorganisms and prevent them from spreading [11]. The formation of NETs is triggered by exposure to bacteria, fungi, viruses, immune complexes, and crystals [12]. In recent years, many studies have confirmed that NETs are mainly involved in the development of inflammatory diseases and cancer [13,14]. The role of NETs in sterile inflammation has been attracting growing attention [15]. Several studies found that NETs leads to atherosclerosis development [16]. NETs can promote endothelial cell dysfunction related to diabetes, and activate the NOD-like receptor thermal protein domain associated protein 3 (NLRP3) inflammasome, damaging glomerular endothelial cells, leading to diabetic nephropathy [17]. Przemyslaw Sapieha *et al.* reported

that target senescent vasculature for tissue remodeling in retinopathy [18]. An excessive production or inadequate clearance of NETs may significantly contribute to autoimmune conditions reactions in autoimmune diseases such as Rheumatoid Arthritis, Systemic Lupus Erythematosus, Idiopathic Inflammatory Myopathies and Psoriasis [19]. A recent study revealed the heterogeneity of neutrophils in the bone marrow, peripheral blood, and spleen in the context of homeostasis and infection, which has substantially advanced our understanding of neutrophil heterogeneity [20]. Another study reported that senescent neutrophils ($CXCR4^+$ $CD62L^{low}$) are more likely to form NETs and facilitate cancer metastasis [21]. This suggests that the neutrophil subsets involved in NET formation differ depending on the specific stimulus conditions. Given the important role of neutrophils and NETs in promoting disease, it is vital to precisely decipher the particular neutrophil subset that induces NET formation in specific pathological circumstances. Although many studies have highlighted the important role of NETs in disease, especially in infectious disease, the role of NETs in diseases caused by sterile inflammation, such as EH, remains unclear.

In this study, we found that Estrogen Receptor 1 ($ESR1^+$) neutrophil-derived NETs interacted with NKCC1 in unciliated epithelial cells and promoted estrogen-triggered sterile inflammation. It is worth mentioning that long-term hormone therapy is the primary treatment option for EH patients. Here, a classic drug aspirin was found to inhibit NET formation and alleviated EH in a nonhuman primate model by directly acetylating at K64 and K82 of HMGN2. Therefore, the therapeutic strategy of targeting NETs may be the first nonhormonal therapy for the treatment of patients with estrogen

abnormalities, including EH.

Results

The interaction between neutrophils and unciliated epithelial cells is involved in the progression of EH

To investigate how the cellular microenvironment varies in different cell subtypes of EH and EN, we performed single-cell RNA sequencing (scRNA-seq), single-cell Assay Transposase Accessible Chromatin sequencing (scATAC-seq), cellular indexing of transcriptomes and epitopes by sequencing (CITE-seq) and spatial transcriptomics sequencing (ST-seq) to profile the cellular landscape in the endometrial tissue of normal donors and patients with EH or EN (**Fig. 1A**). All samples were independently characterized by pathologists (**Supplementary Table 1**). We integrated all of the scRNA-seq data using robust principal component analysis (RPCA) to correct for potential batch effects. Uniform manifold approximation and projection (UMAP) identified the major cell types, including ciliated epithelial cells, unciliated epithelial cells, myeloid cells, T cells, B cells, cycling cells and stromal cells. These cells could be annotated as fifteen transcriptionally distinct clusters with cluster-specific markers (**Fig. 1B**, **Fig. S1A**). The integration of scRNA-seq and CITE-seq further helped us precisely defined the immune cells (**Fig. 1B, Fig. S2**).

Meanwhile, the scATAC-seq experiment was performed in endometrial tissue from normal donors and patients with EH or EN (**Fig. S1B&C**). As ST-seq provided an opportunity to investigate the spatial heterogeneity of the endometrial tissue, we

discovered more comprehensive spatial information concerning the endometrial tissue. The spatial distributions of neutrophils and epithelial cells were visualized by their marker genes (**Fig. S1D**).

Although some studies have revealed increased immune cell infiltration in the progression of EH and EN [7, 22], it is unclear how these immune cells, especially neutrophils, affect EH progression. We detected an increased proportion of neutrophils, B cells and macrophages in the EH and EN groups (**Fig. 1C-E**, **Fig. S3**). Epithelial cells are major effector cells of the EH process [23]. Therefore, to decipher the dynamics of intercellular communication in different groups, we analyzed cell-cell interactions based on scRNA-seq data. Stronger cellular interactions between neutrophils and other nonimmune cells, especially ciliated cells and unciliated cells, were observed in the EH group (**Fig. 1F&G**). We also performed deconvolution analysis on each sample. The results showed a significantly higher proportion of spots containing both neutrophils and unciliated epithelial cells in the EH group compared to the normal group (**Fig. 1H&I**). This could be partly attributed to the higher abundance of both cell types in the EH group, which may explain the observed proximity between neutrophils and unciliated epithelial cells in the EH group. Although we noted that B cells were also increased in EH group, estrogen could still induce typical EH phenotypes in mμMt mice which lack mature B cells, such as enlarged uterus, increased uterine weight and gland/stroma ratio, suggesting B cells are dispensable in the development of EH. However, neutrophil deletion using anti-Ly6G neutralizing antibody could significantly ameliorate EH phenotypes in mμMt mice, indicating neutrophils mainly contribute to

the progression of EH (**Fig. S5**). These results collectively support the critical role of neutrophils in the development of EH.

ESR1^{+} neutrophils are main pathogenic cells in the development of EH

To reveal neutrophil heterogeneity in different pathological circumstances, neutrophils were categorized into five subsets (Neus1-5) in an unsupervised clustering analysis (**Fig. 2A-C**, **Fig. S6**). Interestingly, the proportion of Neus4 (*ESR1*$^{+}$ neutrophils) increased in the EH group, whereas that of Neus2 (*TGM2*$^{+}$ neutrophils) enriched in the EN group (**Fig. 2B**). Stronger cellular interactions between Neus4 and and epithelial cells, were observed in the EH group based on ST-seq (**Fig. S7**). Flow cytometry experiments revealed a higher proportion of *ESR1*$^{+}$ neutrophils in the endometrial tissues of patients with EH (**Fig. S8**). To validate the predicted function of ESR1^{+} human neutrophils *in vivo*, we generated a EH model on human immune system (HIS) mice optimized for human neutrophil engraftment. To eliminate the interference of residual murine neutrophils in HIS mice, we first pre-treated mice with anti-Ly6G neutralizing antibody to ensure that less murine neutrophils are present. Then we found that the EH phenotypes were remarkably ameliorated by treatment with estrogen receptor degrader (Elacestrant) **(Fig. 2D-G**, **Fig. S9)**, indicating that the critical role of neutrophils and estrogen receptor in humanized mice. Importantly, neutrophil-specific *Esr1* conditional KO mice showed an attenuated EH phenotype compared to wild-type littermates following estrogen treatment *in vivo* (**Fig. 2H-K**), indicating *ESR1*$^{+}$ neutrophils are major pathogenic cells of EH.

Estrogen induces the binding of ERα to HMGN2 and promotes NET formation

To further explore the developmental and functional dynamics of neutrophil subtypes, we carried out pseudotime trajectory analysis using both Monocle and CytoTRACE (**Fig. 3A**, **Fig. S10A**). We noticed that Neus2 and Neus4 were localized at different ends of the neutrophil maturation trajectory. This result suggest that neutrophils are in different differentiation states during EN and EH (**Fig. 3A**, **Fig. S10B&C**). To further dissect their functional programs, we applied pseudotime-based gene module analysis, which identified four modules (K1–K4) with distinct dynamic expression patterns. Pseudotime 1 represents the trajectory from normal to EH, along which Neus4 is located at the terminal stage (**Fig. 3B**). Notably, genes in module K3 showed a gradual increase in expression along Pseudotime 1, indicating progressive activation of transcriptional programs during disease transition. The pathways enriched in K3, including integrated stress response, p38MAPK signaling, and steroid hormone response, were predominantly associated with later pseudotime states and specifically enriched in Neus4. These findings suggest that NET-related pathways are progressively engaged as neutrophils advance along the pseudotime trajectory toward hyperplastic states, with Neus4 representing a developmentally distinct subset potentially responsive to estrogen signaling (**Fig. 3B**).

LPS induces NET formation by affecting the TLR4 signaling pathway [24]. However, the mechanism of estrogen-induced NET formation still remains obscure. Therefore, we attempted to elucidate the mechanism of estrogen-induced NET formation. Estrogens usually exert their biological actions through estrogen receptor α (ERα) [25].

213 Consistently, the proportion of *ESR1*$^{+}$ neutrophils was significantly increased in the EH
214 group (**Fig. S11A**). Then, a scATAC-seq analysis to investigate the regulatory activity
215 of ERα in neutrophils from different groups was performed. Consequently, the gene
216 expression levels and gene score of target genes of *ESR1* (the coding gene of ERα) were
217 higher in the EH group than in the EN group (**Fig. S11B&C**, **Fig. S12A**). In addition,
218 estrogen induced the expression of *ESR1* but not *TLR4* in human neutrophils (**Fig.**
219 **S12B-D**). We also found that neutrophils derived from *Esr1* KO mice were not sensitive
220 to estrogen-induced NET formation (**Fig. 3C, Fig. S12E&F, Supplementary Video 1**).
221 Similar results were seen in neutrophils treated with selective ERα inhibitor (**Fig. 3D-**
222 **G**).

223 To further explore the potential role of ERα in NET formation, ChIP-seq analysis
224 was used to predict its target gene. Following scRNA-seq, ChIP-seq analysis and ChIP-
225 qPCR, several genes were identified as ERα potential target genes under estrogen
226 stimulation (**Fig. S11D-F, Fig. S13A&B**), among which *Hmgn2* and *Timm8b* were
227 found to regulate chromatin depolymerization and mitochondrial function in NET
228 formation, respectively [26,27]. Next, we constructed *Hgmn2* or *Timm8b* knockout mice to
229 confirm their role in NET formation. Neutrophils derived from *Timm8b* but not *Hmgn2*
230 knockout mice, could still form NETs upon estrogen induction, suggesting that *Hmgn2*
231 is indispensable for estrogen-induced NET formation (**Fig. S13C&D**, **Fig. S14,**
232 **Supplementary Video 2**). Furthermore, *Hmgn2* KO mice were not sensitive to
233 estrogen-induced EH (**Fig. S13E-J**). Taken together, these data suggest that estrogen-
234 induced binding of ERα to *HMGN2* is a key event in the NET formation of neutrophils.

NETs derived from neutrophils aggravate the progression of EH

To characterize the clinical significance of NETs in EH, the levels of NETs were examined. The results showed that the levels of NE, MPO, cell-free DNA (cfDNA) and MPO-DNA complexes were significantly higher in endometrial tissues from patients with EH than that from the normal group (**Fig. 4A-D**). Furthermore, immunofluorescence staining for citH3 and MPO, specific markers for NET formation and neutrophils, was conducted, and more positive signals in the endometrial tissue of patients with EH were observed (**Fig. 4E**), suggesting abundant NET formation in the endometrial tissues from EH patients. To confirm whether NETs directly promote EH, purified NETs and human endometrial organoids were cocultured *in vitro*. Consequently, exogenous NET supplementation directly accelerated endometrial organoid formation and promoted endometrial epithelial cell proliferation (**Fig. 4F, Fig. S15**). To confirm the role of NETs derived from neutrophils in EH, we generated neutrophil *Pad4* conditional knockout mice and found that *Pad4* deficiency in neutrophil was resistant to estrogen-induced EH in mice and NETs formation (**Fig. 4G-J**). In addition, the NETs inhibitor GSK484 and the NETs degrader DNase I can also alleviate estrogen-induced EH (**Fig. S16&17**). These data indicate that NETs derived from neutrophil exacerbate the progression of EH.

NETs promote epithelial cell proliferation and EH in a NKCC1-dependent manner

To decipher the molecular mechanism by which NETs promote EH, scRNA-seq analysis of uteri tissue from murine EH model treated with NET inhibitor GSK484 was performed (**Fig. 5A&B**). Each cell cluster was characterized according to marker genes

and cell proportions (**Fig. 5C**, **Fig. S18A-E**, **Fig. S19A-C**). As a result, GSK484 treatment decreased the proportion of neutrophils and unciliated epithelial cells in response to estradiol (**Fig. S18B&C**). Moreover, both proliferation-related genes in unciliated epithelial cells and NET formation-related genes in neutrophils were downregulated after GSK484 administration (**Fig. S18F**, **Fig. S19D**). We extracted the differentially expressed genes from the GSK484 + Estradiol vs. Estradiol group for pathway enrichment analysis neutrophils. We observed that GSK484 administration significantly affected NETs formation related pathways such as regulation of cellular response to stress, inflammatory response, and humoral immune response (**Fig. S19E**).

Next, three lines of evidence suggested that 11 differentially expressed genes in unciliated epithelial cells were identified in the intersection of human, monkey and mouse scRNA-seq data (**Fig. 5C&D**). In addition, ion homeostasis-related pathways were enriched in unciliated epithelial cells from GSK484-treated mice (**Fig. 5E**). Among the 11 selected genes, *SLC12A2* (encoding NKCC1) was the only gene associated with ion channels and is a known $Na^+/K^+/2Cl^-$ cotransporter [28]. Intriguingly, NETs can regulate the imbalance of $Na^+/K^+/2Cl^-$ ion homeostasis (**Fig. 5F**). To screen the direct binding proteins of NETs, a biotinylated NET-DNA pull-down assay was performed, and 65 membrane proteins were identified as potential binding proteins of NETs by liquid chromatography coupled with mass spectrometry (**Fig. S20A&B**). These membrane protein-coding genes together with 11 differentially expressed genes (**Fig. 5D**) were then intersected, and NKCC1 was identified as a cell-surface DNA receptor (**Fig. S20C&D**). This result was also confirmed by immunoblotting after

biotinylated NET-DNA pull-down (**Fig. 5G**). More importantly, we found that NET-DNA can bind to the NKCC1 protein *in vitro*. Both untreated NETs and trypsin-treated NETs exhibited high affinity. However, due to the absence of molecular weight constraints on NETs, the specific KD constant was unobtainable. The RU (Response Unit) curve indicated a significant decrease in binding affinity after Dnase I treatment (**Fig. 5H, Fig. S21**). Previous studies have confirmed that NKCC1 can regulate cell ion homeostasis and then affect cell proliferation [29]. Importantly, epithelial cell-specific *Slc12a2* conditional knockout mice showed an attenuated EH phenotype compared to wild-type littermates following estrogen treatment *in vivo* (**Fig. 5I-K**). These findings indicate that NETs promote endometrial epithelial cell proliferation and EH in a NKCC1-dependent manner.

Aspirin ameliorates EH in cynomolgus monkey through inhibiting NETs via HMGN2 acetylation

We next focused on screening potential drugs that could inhibit estrogen-induced NET formation based on the FDA-approved drug library, and the classic drug aspirin was identified as a potential NET inhibitor (**Fig. 6A&B**). We observed that aspirin not only inhibited NET formation in estrogen-treated neutrophils *in vitro* and estrogen-treated cynomolgus monkeys *in vivo* but also dramatically improved estrogen-induced uterine enlargement and overgrowth of endometrial glands in both monkeys and mice (**Fig. 6C-E**, **Fig. S22&23, Supplementary Video 3**). Correlation analysis based on the scRNA-seq data of monkey uterine tissues revealed that the aspirin-treated group was

more similar to the normal group than the estrogen-treated group (**Fig. 6F&G**). This finding further confirmed the effect of aspirin on EH. To evaluate the mechanism by which aspirin improves EH, we performed differential expression analysis combined with experimental verification. Consistent with the NET inhibitor GSK484, aspirin also inhibited the expression of *Slc12a2*/NKCC1 (**Fig. 6H-J**).

ChIP-seq experiments consequently confirmed that aspirin decreased the binding of ERα to *HMGN2* (**Fig. S24**). To further uncover the target of aspirin, we used label-free target-responsive accessibility profiling strategy (TRAP) to explore the aspirin-binding proteins by probing the lysine accessibility changes on a proteome-level. At the same time, we combined ChIP-seq experimental data to identify the target protein of aspirin (**Fig. S25A&B**). Considering that estrogen induced ERα binding to *HMGN2*, we hypothesized that HMGN2 was the target protein of aspirin. Cellular thermal shift assay (CETSA) exhibited that aspirin significantly enhanced the thermal stability of HMGN2 even at higher temperatures compared to control group (**Fig. S25C**). Acetylation of proteins by aspirin has been demonstrated in previous studies [30]. We also found aspirin could directly acetylate HMGN2 protein at K64 and K82 sites (**Fig. 6K-M**). Furthermore, HMGN2 with mutations in these acetylation sites could block the inhibitory effect of aspirin on NET formation (**Fig. 6N**, **Fig. S26**).

In conclusion, a unique neutrophil subpopulation was newly identified to be involved in estrogen-driven NET formation. Distinct from infectious state, estrogen-induced NETs were mainly consequent from ERα binding to *HMGN2*. Functionally, the ablation or inhibition of NETs significantly ameliorated EH in mouse model.

Mechanistically, NETs bound to NKCC1 in unciliated epithelial cells and promoted cell proliferation. Pharmacologically, a classic drug aspirin was screened to inhibit NET formation via acetylating HMGN2 at K64 and K82 sites and confirmed to alleviate hyperplasia in a nonhuman primate EH model (**Graphical abstract**).

Discussion

Here, we provide a detailed analysis of the immune and nonimmune cell microenvironment in endometrial tissue at single-cell resolution and have identified disease-specific neutrophil subsets that contribute to NET formation. Furthermore, we discovered that neutrophil heterogeneity and NET formation play key roles in the pathogenesis of EH and that aspirin alleviated EH in a murine model.

In light of the fact that EH (sterile inflammation) and EN (bacterial infectious inflammation), as common gynecological diseases, have long plagued women, we constructed a single-cell multiomics study in an attempt to provide new insights into gynecology-related diseases, especially EH. Although endometritis is also a disease that deserves serious attention, the well-established antibiotic treatment has brought great hope to patients with EN. Therefore, we focused on the mechanisms and pharmacological treatment of EH. The interaction between neutrophils and epithelial cells was noted to be enhanced dramatically, particularly in the EH group. Although some studies have revealed an increase in immune cell infiltration in the progression of endometrium-related diseases [7, 22], it is unclear how these immune cells, especially neutrophils, affect EH progression. In recent years, the advent of high resolution has enabled us to uncover the presence of heterogeneity in neutrophils, as presented in

346 various phenotypes, under physiological and pathological contexts [20]. Neutrophils from
347 different subpopulations function diversely in inflammatory diseases and cancers [31-33],
348 which merits further exploration. Here, neutrophil heterogeneity in human endometrial
349 tissue was observed. The proportion of Neus4 cells ($ESR1^+$) increased in the EH group,
350 whereas that of Neus2 cells ($TGM2^+$) increased in the EN group. Interestingly, we
351 found that pathways such as neutrophil chemotaxis, neutrophil migration, and response
352 to virus were significantly enriched in Neus 2. In contrast, pathways related to NET
353 formation, such as integrated stress response signaling, were significantly enriched in
354 Neus 4. This suggests that Neus 2 primarily plays a role in defending against pathogens
355 to promote EN, while Neus 4 promotes EH mainly through NET formation. In addition,
356 EN was not the focus of this study, we did not perform in-depth analyses on the Neus
357 2. To validate the predicted function of $ESR1^+$ human neutrophils, we generated a EH
358 model on human immune system (HIS) mice optimized for human neutrophil
359 engraftment. We found that the EH phenotypes were remarkably ameliorated by
360 treatment with estrogen receptor degrader, indicating that $ESR1^+$ neutrophils are major
361 pathogenic cells of EH. We have to admit that we did not explore other subsets due to
362 the proportion of other neutrophil subsets hardly changed significantly in the
363 development of EH or EN. Although these cells showed no significant differences in
364 their proportions, there may be functional changes. However, considering the focus of
365 this study, we concentrated our in-depth analyses on cells that exhibited more
366 pronounced changes in cell proportion, cell–cell interactions, and pathway enrichment.
367 We cannot exclude the role of other neutrophil subsets in other diseases, which is

worthy of further investigation.

The formation of NETs has been primarily considered to be the result of recognition of microorganism damage-associated molecular patterns and immune complexes [34,35]. Continuous estrogen exposure contributes to the EH process [4]. Studies regarding the effect of estrogen on NET formation are limited, which motivated us to explore whether estrogen induces NET formation and to compare neutrophil heterogeneity in infection- or hormone-driven NET formation. Surprisingly, we found that estradiol significantly induced NET formation in both cynomolgus monkeys and humans. Human pregnancy was previously associated with a mild proinflammatory state characterized by circulatory neutrophil activation [36]. A recent study uncovered the different roles of neutrophil subsets in homeostasis and infection [20]. However, it remains unclear whether all neutrophil subpopulations form NETs under external stimuli. Using scRNA-seq technology, we discovered that neutrophils of different subpopulations accounted for NET formation under infection- or hormone-driven states. Specifically, $ESR1^{+}$ neutrophils were found to be primarily involved in estrogen-induced NET formation. The mechanism was mainly related to the binding of ERα to *HMGN2*, consequently regulating chromatin depolymerization function, both of which is key molecular events for NET formation [26].

For a long time, EH has been mostly attributed to continuous estrogen exposure and epithelial cell proliferation [4]. Somewhat contradictory to the view that abnormal proliferation of endometrial epithelial cells is induced by estrogen, we showed that the level of NETs was higher in EH patients than in healthy donors. This finding raised the

intriguing issue of whether it is possible to target NETs to treat EH. Our research revealed that NET removal considerably reduced the severity of EH in mice and monkeys. In addition, high levels of estrogen are also risk factors for breast cancer [37]. The aforementioned examples further indicate that targeting NETs may be a promising strategy for the treatment of estrogen-related disorders. Although counterintuitive to the concept that the aberrant proliferation of endometrial epithelial cells is driven by estrogen, we discovered that NETs served as a new bridge between estrogen and epithelial cells. Mechanistically, NKCC1, a protein associated with ion homeostasis [38], was identified as a NET-DNA receptor on endometrial epithelial cells for abnormal proliferation. NKCC1 is a $Na^+/K^+/2Cl^-$ cotransporter which as a known regulator of cell volume [39]. In the present study, we found that NETs might bind to NKCC1 and control endometrial epithelial cell proliferation. This may explain to some extent how NETs regulate EH progression. We acknowledge that epithelial subtypes, fibroblasts, and endothelial cells were not deeply characterized. Our study focused on the neutrophil–unciliated epithelial cell axis, and epithelial-specific Slc12a2 deletion supported its functional importance in NET-mediated EH. Future studies are needed to determine whether specific epithelial subtypes differentially respond to NETs.

Currently, progesterone and surgery are the two main treatments for EH [40]. Novel nonhormone replacement therapies are urgently needed for EH patients. Currently, estrogen receptor degraders are primarily used for patients with advanced breast cancer in clinical practice, and they are associated with significant side effects [41]. In this study, we found that NETs play an important role in promoting the progression of EH.

Therefore, inhibiting NET formation represents a novel therapeutic approach for EH. NETs inhibitors, on the other hand, have not been used clinically. Compared with estrogen receptor degraders and NETs inhibitors, screening drugs from the FDA drug library to inhibit NETs formation is a safer strategy. Thus, FDA-approved drugs were screened *in vitro*, and aspirin was identified to inhibit NET formation. Macaques, have menstrual cycles that are most similar to those of humans [42]. Thus, macaques are frequently used in research due to the availability of their basic data and physiological similarities to humans. Considered that estrogen levels in women typically peak before ovulation (on day 14 of the menstrual cycle), and then decrease continuously. Patients with endometrial hyperplasia usually have persistently high levels of estrogen [6]. Therefore, we used a 5-week high-level estrogen induction model to induce EH in cynomolgus monkeys, and the H&E staining results also confirmed the occurrence of EH. From the perspective of the therapeutic effect of aspirin, aspirin is not limited to the treatment of inflammation-related diseases, but also shows good therapeutic potential in other diseases such as cardiovascular disease and women with prepregnancy diabetes, obesity, and hypertension [43,44]. In this study, we found that aspirin significantly ameliorated estrogen-induced uterine enlargement and overgrowth of endometrial glands in monkeys. These results suggest that the use of aspirin would avoid the side effects of hormone therapy and the risks of surgical treatment, suggesting a drug repurposing strategy for EH treatment. It is worth mentioning that aspirin directly acetylates at K64 and K82 of HMGN2, which is involved in regulating chromatin depolymerization. Furthermore, HMGN2 with mutations in these acetylation

sites could block the inhibitory effect of aspirin on NET formation. These data can help us understand how aspirin inhibits NET formation. We selected aspirin as a potential agent to improve EH based on the estrogen-induced NETs formation system. However, we cannot rule out that aspirin may also ameliorate EH through other ways, such as inhibiting ERα expression in endometrial epithelial cells. In addition, the side effects of aspirin mainly include gastrointestinal irritation, increased risk of bleeding, allergic reactions, and liver and kidney damage [45,46]. When using aspirin to treat endometrial hyperplasia, it is important to remind patients to pay attention to gastrointestinal reactions, abnormal uterine bleeding, and to regularly monitor liver and kidney function.

In conclusion, a unique neutrophil subpopulation with ESR1 expression was newly identified to be involved in estrogen-driven NET formation. In addition, NKCC1 was identified as a new NET-DNA receptor on endometrial epithelial cells, accounting for abnormal proliferation during EH. In terms of disease intervention, blockade of NET formation by aspirin would be the first nonhormonal drug strategy for patients with estrogen abnormalities such as EH.

References

1. van der Poll, T., van de Veerdonk, F.L., Scicluna, B.P. & Netea, M.G. The immunopathology of sepsis and potential therapeutic targets. *Nat Rev Immunol* **17**, 407-420 (2017).
2. Shen, H., Kreisel, D. & Goldstein, D.R. Processes of sterile inflammation. *J Immunol* **191**, 2857-2863 (2013).
3. Kelleher, A.M., DeMayo, F.J. & Spencer, T.E. Uterine Glands: Developmental Biology and Functional Roles in Pregnancy. *Endocr Rev* **40**, 1424-1445 (2019).
4. Ring, K.L., Mills, A.M. & Modesitt, S.C. Endometrial Hyperplasia. *Obstet Gynecol* **140**, 1061-1075 (2022).
5. Singh, N. & Sethi, A. Endometritis - Diagnosis,Treatment and its impact on

fertility - A Scoping Review. *JBRA Assist Reprod* **26**, 538-546 (2022).
6. Crosbie, E.J. *et al.* Endometrial cancer. *Lancet* **399**, 1412-1428 (2022).
7. Symons, L.K. *et al.* The Immunopathophysiology of Endometriosis. *Trends Mol Med* **24**, 748-762 (2018).
8. Wilson, M.R. *et al.* Obesity alters the mouse endometrial transcriptome in a cell context-dependent manner. *Reprod Biol Endocrinol* **20**, 163 (2022).
9. Wang, W. *et al.* Single-cell transcriptomic atlas of the human endometrium during the menstrual cycle. *Nat Med* **26**, 1644-1653 (2020).
10. Qu, J. *et al.* A reference single-cell regulomic and transcriptomic map of cynomolgus monkeys. *Nat Commun* **13**, 4069 (2022).
11. Brinkmann, V. *et al.* Neutrophil extracellular traps kill bacteria. *Science* **303**, 1532-1535 (2004).
12. Papayannopoulos, V. Neutrophil extracellular traps in immunity and disease. *Nat Rev Immunol* **18**, 134-147 (2018).
13. Yang, L. *et al.* DNA of neutrophil extracellular traps promotes cancer metastasis via CCDC25. *Nature* **583**, 133-138 (2020).
14. Munoz, L.E. *et al.* Neutrophil Extracellular Traps Initiate Gallstone Formation. *Immunity* **51**, 443-450 e444 (2019).
15. Yi Hu. *et al.* Neutrophil Extracellular Traps (NETs) in Sterile Inflammatory Diseases. *J Inflamm Res* **18**, 7989-8004 (2025).
16. Annika Warnatsch. *et al.* Inflammation. Neutrophil extracellular traps license macrophages for cytokine production in atherosclerosis. *Sciences* **17**, 316-20 (2015).
17. Anubhuti Gupta. *et al.* Neutrophil Extracellular Traps Promote NLRP3 Inflammasome Activation and Glomerular Endothelial Dysfunction in Diabetic Kidney Disease. *Nutrients* **20**, 2965 (2022).
18. Przemyslaw Sapieha. *et al.* Neutrophil extracellular traps target senescent vasculature for tissue remodeling in retinopathy. *Science* **21**, 5356 (2020).
19. Keum Hwa Lee. *et al.* Neutrophil extracellular traps (NETs) in autoimmune diseases: A comprehensive review. *Autoimmun Rev* **16**, 1160-1173 (2017).
20. Xie, X. *et al.* Single-cell transcriptome profiling reveals neutrophil heterogeneity in homeostasis and infection. *Nat Immunol* **21**, 1119-1133 (2020).
21. Chenghui Yang. *et al.* Aged neutrophils form mitochondria-dependent vital NETs to promote breast cancer lung metastasis. *J Immunother Cancer* **9**, e002875 (2021).
22. Lai, Z.Z. *et al.* Changes in subsets of immunocytes in endometrial hyperplasia. *Am J Reprod Immunol* **84**, e13295 (2020).
23. Gao, Y., Li, S. & Li, Q. Uterine epithelial cell proliferation and endometrial hyperplasia: evidence from a mouse model. *Mol Hum Reprod* **20**, 776-786 (2014).
24. Schattner, M. Platelet TLR4 at the crossroads of thrombosis and the innate immune response. *J Leukoc Biol* **105**, 873-880 (2019).
25. Deroo, B.J. & Korach, K.S. Estrogen receptors and human disease. *J Clin Invest* **116**, 561-570 (2006).

26. Pogna, E.A., Clayton, A.L. & Mahadevan, L.C. Signalling to chromatin through post-translational modifications of HMGN. *Biochim Biophys Acta* **1799**, 93-100 (2010).
27. Fullston, T., Mitchell, M., Wakefield, S. & Lane, M. Mitochondrial inhibition during preimplantation embryogenesis shifts the transcriptional profile of fetal mouse brain. *Reprod Fertil Dev* **23**, 691-701 (2011).
28. Young, S.Z. *et al.* NKCC1 knockdown decreases neuron production through GABA(A)-regulated neural progenitor proliferation and delays dendrite development. *J Neurosci* **32**, 13630-13638 (2012).
29. Demian, W.L. *et al.* The Ion Transporter NKCC1 Links Cell Volume to Cell Mass Regulation by Suppressing mTORC1. *Cell Rep* **27**, 1886-1896 e1886 (2019).
30. Dai, J. *et al.* Acetylation Blocks cGAS Activity and Inhibits Self-DNA-Induced Autoimmunity. *Cell* **176**, 1447-1460 e1414 (2019).
31. Xue, R. *et al.* Liver tumour immune microenvironment subtypes and neutrophil heterogeneity. *Nature* **612**, 141-147 (2022).
32. Qi, X. *et al.* Identification and characterization of neutrophil heterogeneity in sepsis. *Crit Care* **25**, 50 (2021).
33. Veglia, F. *et al.* Analysis of classical neutrophils and polymorphonuclear myeloid-derived suppressor cells in cancer patients and tumor-bearing mice. *J Exp Med* **218** (2021).
34. de Bont, C.M., Boelens, W.C. & Pruijn, G.J.M. NETosis, complement, and coagulation: a triangular relationship. *Cell Mol Immunol* **16**, 19-27 (2019).
35. Thiam, H.R., Wong, S.L., Wagner, D.D. & Waterman, C.M. Cellular Mechanisms of NETosis. *Annu Rev Cell Dev Biol* **36**, 191-218 (2020).
36. Giaglis, S. *et al.* Multimodal Regulation of NET Formation in Pregnancy: Progesterone Antagonizes the Pro-NETotic Effect of Estrogen and G-CSF. *Front Immunol* **7**, 565 (2016).
37. Clemons, M. & Goss, P. Estrogen and the risk of breast cancer. *N Engl J Med* **344**, 276-285 (2001).
38. Chew, T.A. et al. Structure and mechanism of the cation-chloride cotransporter NKCC1. Nature **572**, 488-492 (2019)..
39. Kahle, K.T. *et al.* K-Cl cotransporters, cell volume homeostasis, and neurological disease. *Trends Mol Med* **21**, 513-523 (2015).
40. Chandra, V., Kim, J.J., Benbrook, D.M., Dwivedi, A. & Rai, R. Therapeutic options for management of endometrial hyperplasia. J Gynecol Oncol 27, e8 (2016).
41. Neha Bhatia. *et al.* Selective Estrogen receptor degraders (SERDs) for the treatment of breast cancer: An overview. Eur J Med Chem 256:115422 (2023).
42. K A O'Connor. *et al.* Menstrual cycle variability and the perimenopause. *Am J Hum Biol.* **13**, 465-78 (2001).

43. Mohammed E Al-Sofiani. *et al.* Aspirin for Primary Prevention of Cardiovascular Disease in Diabetes: a Review of the Evidence. *Curr Diab Rep*

23, 107 (2019).
44. Joel G Ray. *et al.* Aspirin Use for Preeclampsia Prevention Among Women With Prepregnancy Diabetes, Obesity, and Hypertension. *JAMA* **25**, 388-390 (2022).
45. J P Kelly. *et al.* Risk of aspirin-associated major upper-gastrointestinal bleeding with enteric-coated or buffered product. Lancet **23**, 1413-6 (1996).
46. H J Zimmerman. *et al.* Effects of aspirin and acetaminophen on the liver. Arch Intern Med **23**, 141 (1981).

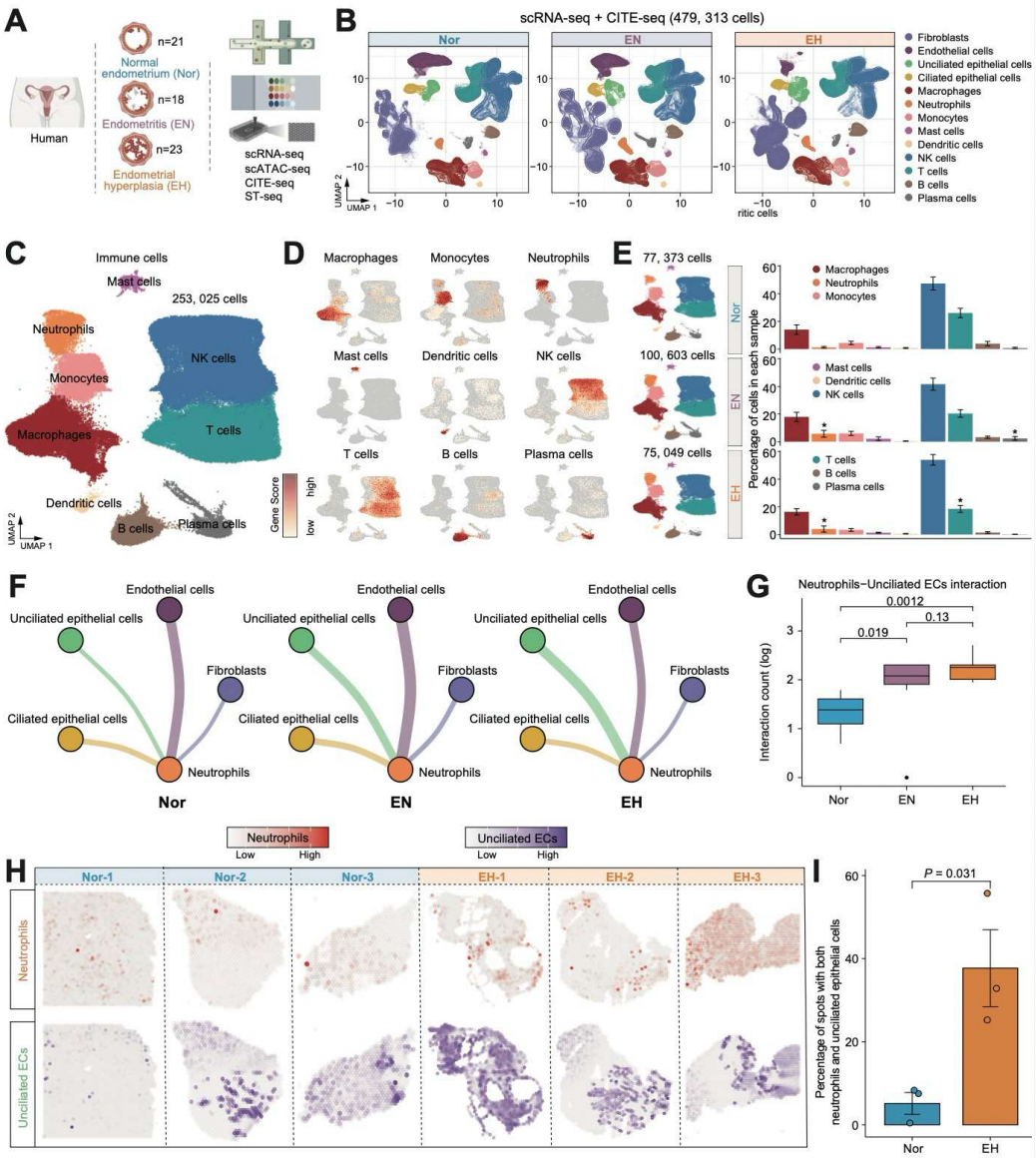


Figure 1. Single-cell multiomics map of patients with EH and EN.

(A) Schematic of human endometrial tissue collection. **(B)** Uniform Manifold Approximation and Projection (UMAP) plots showing the distribution of cell types by groups. **(C)** UMAP plot showing the subtypes of immune cells, colored by subtypes. **(D)** Feature plots showing the gene score of selected cluster-specific gene signatures. Cells with the highest gene score are colored red. **(E)** UMAP plots displaying the distribution of cells in different groups as colored by immune cell types (left) and bar plots showing the cell type abundance for different groups (right). The *p*-value was calculated using the Wilcoxon rank sum test. * $p < 0.05$. **(F)** Network diagrams showing directed interactions from neutrophils to non-immune cells, including endothelial cells, unciliated epithelial cells, ciliated epithelial cells, and fibroblasts, in Nor, EN, and EH samples based on scRNA-seq. Line thickness represents the strength of cell-cell

interactions. **(G)** Boxplot indicating cell interaction counts between neutrophils and unciliated epithelial cells according to (F). The *p*-value was calculated using the Wilcoxon rank sum test. **(H)** Spatial distribution of spots colored by neutrophil scores (top) and unciliated epithelial cell scores (bottom) in human endometrial tissue. **(I)** Bar plot showing the percentage of spots with both neutrophils and unciliated epithelial cells according to (H). The *p*-value was calculated using the Wilcoxon rank sum test.

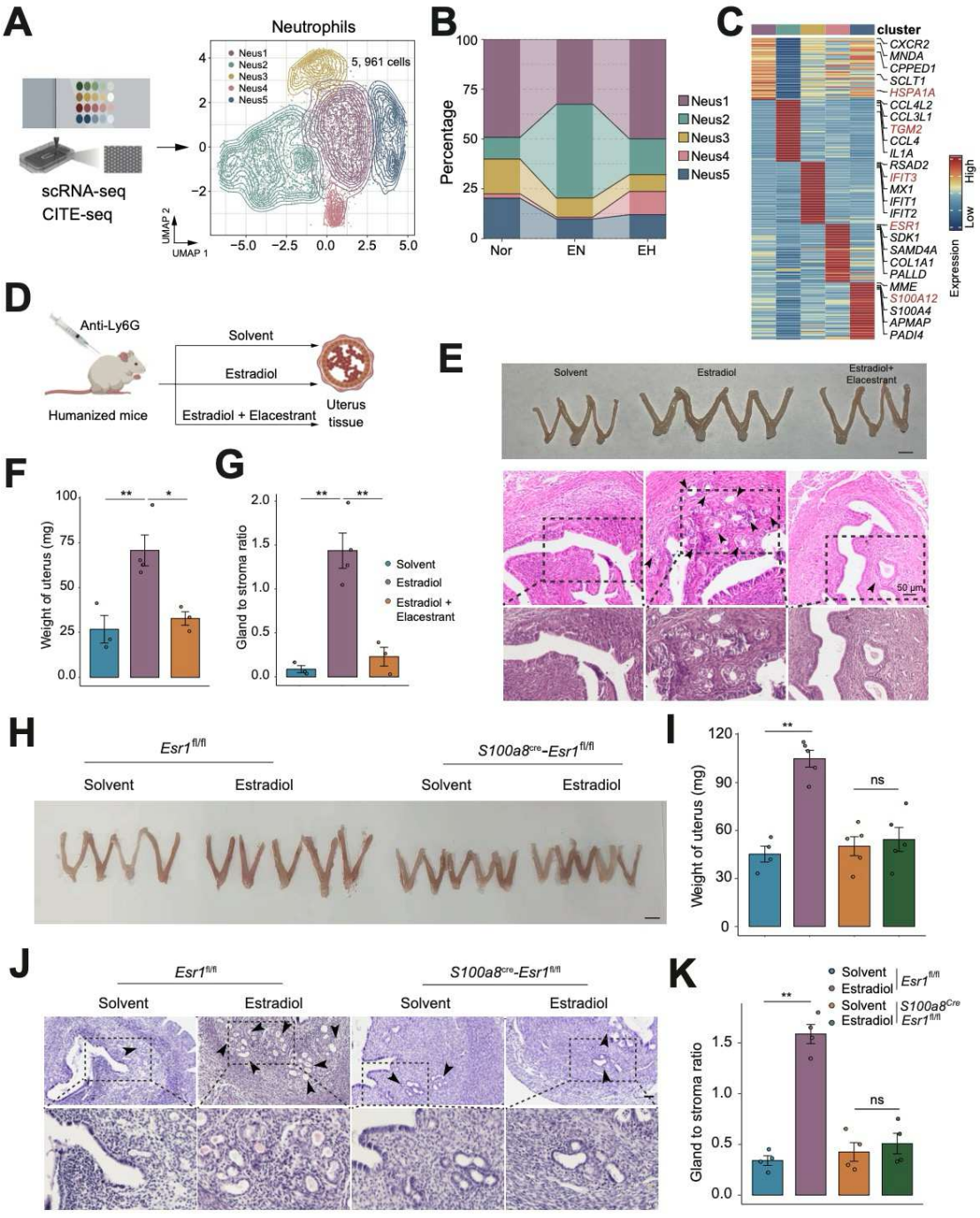


Figure 2. *ESR1*$^{+}$ neutrophils are main pathogenic cells in the development of EH.

(A) Schematic diagram of analysis (left); UMAP plot displaying five neutrophil clusters (right) from human endometrial tissue. **(B)** Bar plot representing the percentage of five neutrophil clusters from each group. **(C)** Heatmap showing the expression of marker genes (top 20) in the indicated neutrophil subtypes. **(D)** Schematic overview of

experimental design: NCG humanized (human immune system, HIS) mice were treated with estradiol (50 μg/kg, s.c.) for 21 days. Anti-mouse Ly6G antibody (12.5 mg/kg) were administered on two days interval, and Elacestrant was administered intragastrically daily at a dosage of 30 mg/kg. **(E)** Representative macrophotographs of uterus in each group (n=3 or 4), Scale bar, 0.5 cm; Representative images of H&E staining (scale bar, 50 μm). **(F)** Uterus weight of each group (n=3 or 4), $^{**}P<0.01$, $^{*}P<0.05$. **(G)** Statistics of the area ratio of gland to stroma according to H&E images (n=3-4), $^{**}P<0.01$, $^{*}P<0.05$. **(H)** *Esr1*$^{fl/fl}$ or *S100a8*^{Cre}-*Esr1*$^{fl/fl}$ mice were given a daily subcutaneous injection of 50 μg/kg estradiol for 21 days. Representative macrophotographs of uterus in each group (n=4 or 5), Scale bar, 0.5 cm. **(I)** Uterus weight of each group (n=4 or 5), $^{**}P<0.01$. **(J)** Representative images of H&E staining (n=4 or 5, scale bar, 50 μm). **(K)** Statistics of the area ratio of gland to stroma according to H&E staining images (n=4 or 5), $^{**}P<0.01$.

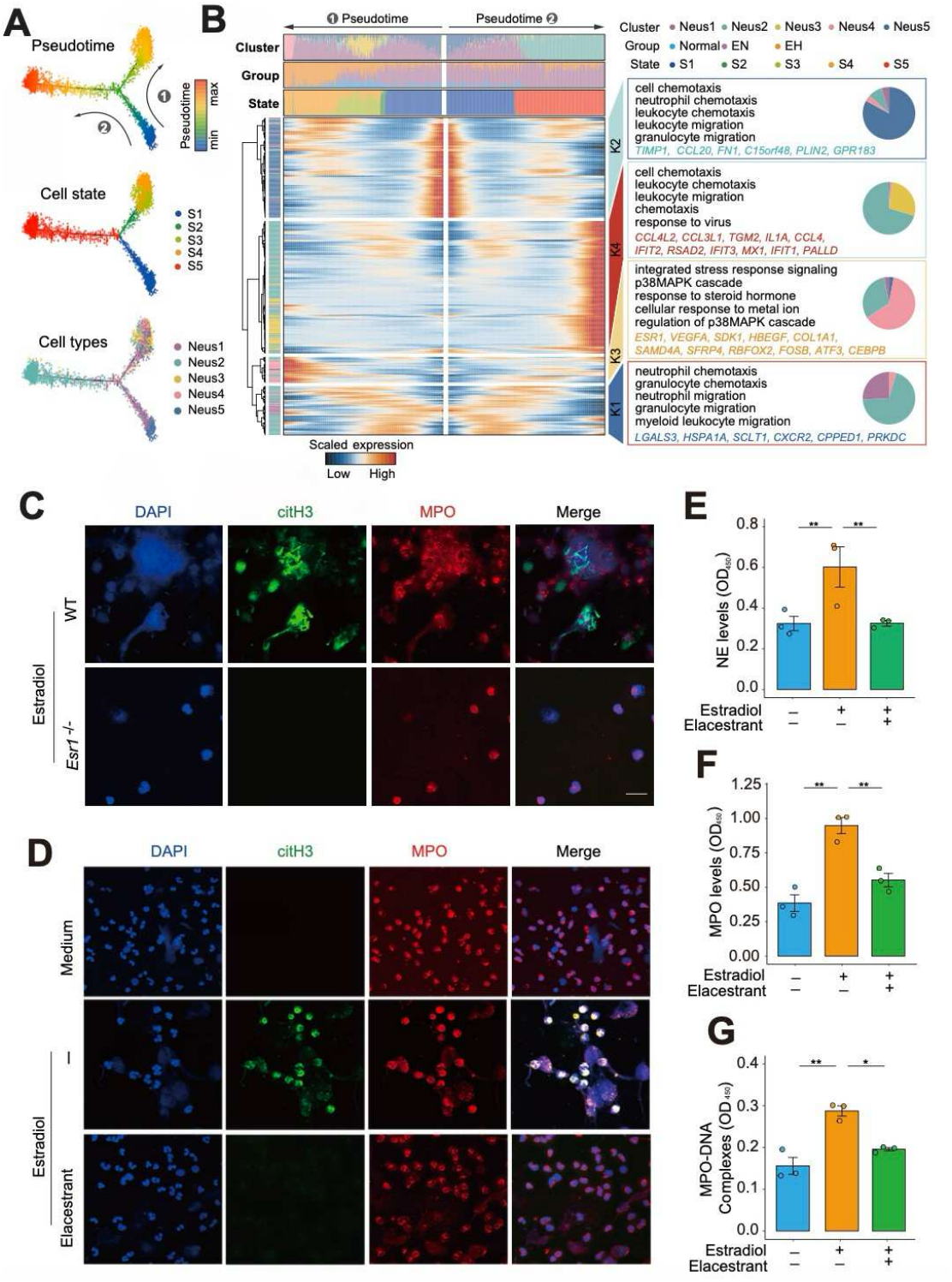
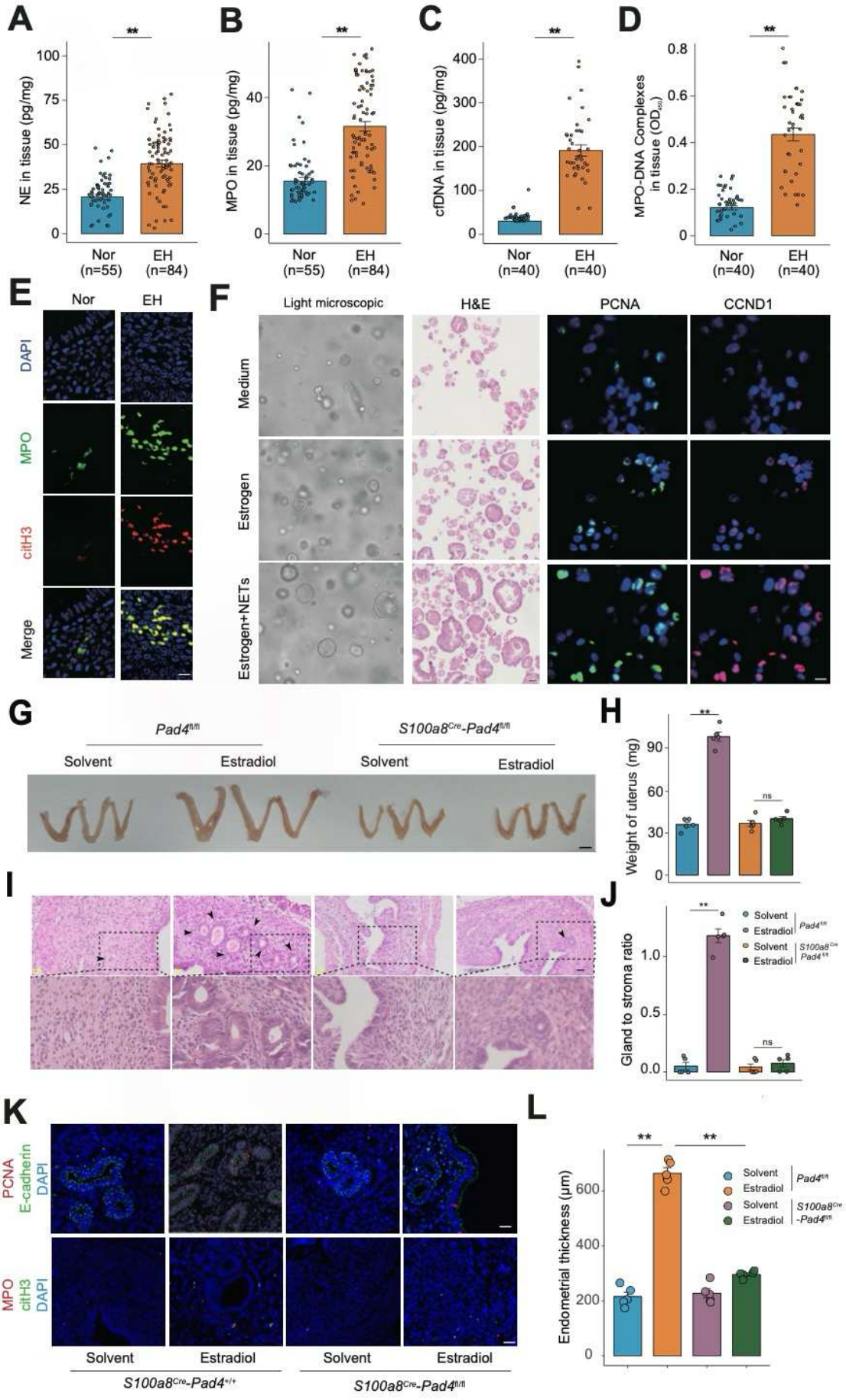


Figure 3. Estrogen induces the binding of ERα to HMGN2 and promotes NET formation.

(A) Semisupervised pseudotime trajectory of neutrophil subtypes inferred by Monocle2. Trajectory is colored by pseudotime, cell states, and cell subtypes. **(B)** Heatmap showing the scaled expression of differentially expressed genes across pseudotime from (h). Genes and functional pathways (listed to the right of the heatmap) are assigned to specific cell states based on their expression levels. Bar plots above the heatmap are scaled diagrams of different cell states and cell clusters during pseudotime differentiation trajectory. Pie plots on the right showing the distribution

of cell subtypes harboring differential genes across different modules. **(C)** The neutrophils from peripheral blood of WT mice or *Esr1* KO mice were incubated with 50 nM or medium at 37℃ for 2 h. Neutrophils were stained with citH3 (green), MPO (red) and DAPI (blue). Scale bar: 20 μm. **(D)** Purified neutrophils from the peripheral blood of healthy donors incubated with elacestrant at 37℃ for 12 h. Neutrophils were stained with citH3 (green), MPO (red) and DAPI (blue). Scale bar: 20 μm. **(E-G)** Neutrophils were incubated with 50 nM estradiol and/or 4 μM elacestrant at 37℃ for 12 h. OD_{450} value reflects the level of MPO, NE or MPO-DNA Complexes; $^{**}P<0.01$.


A
B
C
D
NE in tissue (pg/mg)
MPO in tissue (pg/mg)
cfDNA in tissue (pg/mg)
MPO-DNA Complexes in tissue (OD405)
Nor (n=55)
EH (n=84)
Nor (n=40)
EH (n=40)
E
Nor
EH
DAPI
MPO
citH3
Merge
F
Light microscopic
H&E
PCNA
CCND1
Medium
Estrogen
Estrogen+NETs
G
Pad4fl/fl
S100a8Cre-Pad4fl/fl
Solvent
Estradiol
H
Weight of uterus (mg)
ns
I
J
Gland to stroma ratio
K
PCNA
E-cadherin
DAPI
MPO
citH3
S100a8Cre-Pad4+/+
S100a8Cre-Pad4fl/fl
L
Endometrial thickness (μm)

606

Figure 4. NETs derived from neutrophil aggravate the progression of EH

(A-D) Levels of NE, MPO, cfDNA and MPO-cfDNA complex in endometrial tissues from EH patients and normal donors, $^{**}P<0.01$. **(E)** Immunofluorescence staining of endometrial tissue from EH patients and normal donors with MPO (green), citH3 (red) and DAPI (blue). Scale bar: 20 μm. **(F)** Endometrial organoid from EH patienst was treated with 10 ng/mL NETs or 50 nM estradiol for 5 days. Microscopic images were provided daily. Representative images of H&E staining (Scale bar: 50 μm). Immunofluorescence staining of organoid with PCNA (green), CCND1 (Red) and DAPI (blue). Scale bar: 50 μm. **(G)** *Pad4*$^{fl/fl}$ or *S100a8*^{Cre}-*Pad4*$^{fl/fl}$ mice were given a daily subcutaneous injection of 50 μg/kg estrogen for 21 days. Representative macrophotographs of uterus in each group (scale bar, 0.5 cm). **(H)** Uterus weight of each group (n=5), $^{**}P<0.01$. **(I)** Representative images of H&E staining (n=5, scale bar, 50 μm). **(J)** Statistics of the area ratio of gland to stroma according to H&E images (n=5), $^{**}P<0.01$. **(K)** Mice endometrial tissues were stained with PCNA or MPO (Red), E-cadherin or citH3 (green) and DAPI (blue), (n=3), Scale bar: 20 μm. **(L)** Statistics of endometrial thickness according to H&E staining images (n=5); $^{**}p < 0.01$.

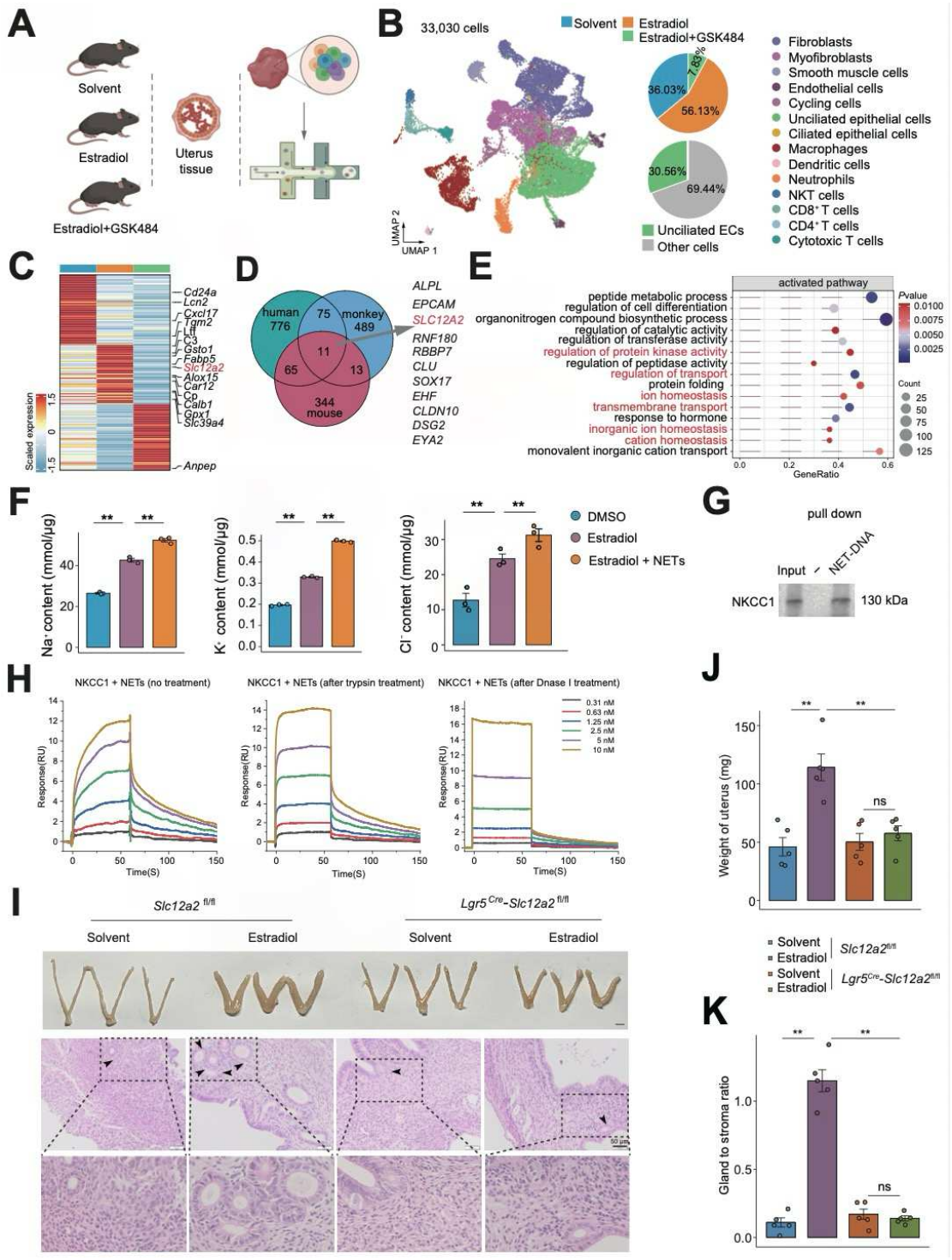
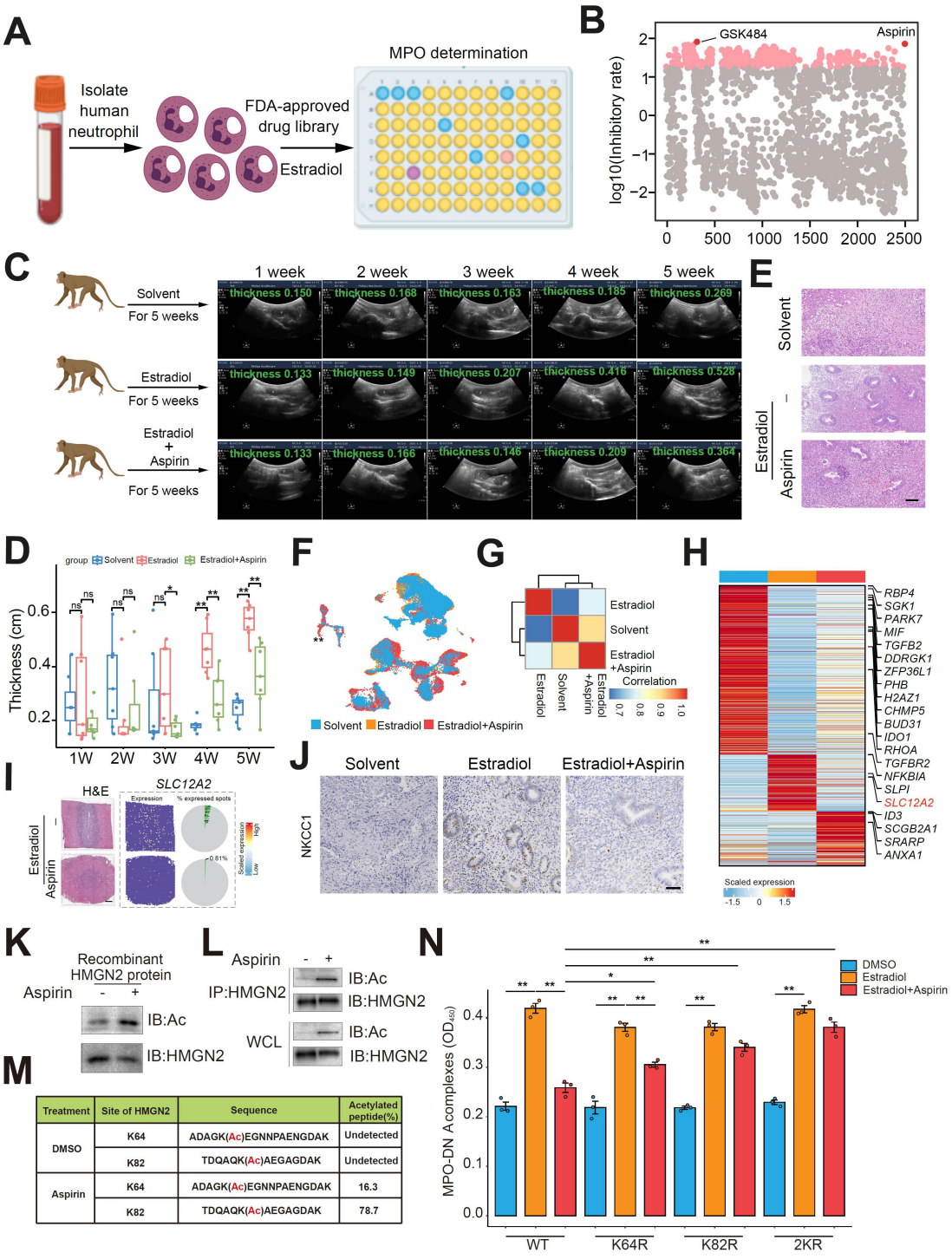


Figure 5. NETs promote epithelial cell proliferation and EH in a NKCC1-dependent manner.

(A) Female C57BL/6 mice were treated with estradiol (50 μg/kg, s.c.) with or without GSK484 (4 mg/kg, i.p.) for 21 days. Schematic overview of mouse scRNA-seq experimental design. **(B)** UMAP plot of mouse cell types. Bottom right, the proportion of unciliated epithelial cells and other cells; top right, the proportion of unciliated epithelial cells among the three groups. **(C)** Heatmap showing the expression pattern of marker genes in the groups. **(D)** Overlap of gene sets in human, monkey and mouse. Human: upregulated genes of non-ciliated epithelial cells in EH group compared to normal group; Monkey: upregulated genes of non-ciliated epithelial cells in Estradiol group

compared to Solvent group; Mouse: downregulated genes of non-ciliated epithelial cells in Estradiol+GSK484 group compared to Estradiol group. **(E)** Lollipop chart demonstrating significant enrichment of ion homeostasis-related pathways in unciliated epithelial cells from estrogen-treated mice. **(F)** Endometrial epithelial cells were treated with 10 ng/mL NETs or 50 nM estradiol for 24 h. Then the content of Na^+, K^+, Cl^- ion in cells were measured, $^{**}P<0.01$. **(G)** Immunoblotting of the membrane proteins of human endometrial epithelial cells pulled down by biotinylated NET-DNA and measured by anti-NKCC1 antibody. **(H)** The binding of NETs to NKCC1 protein under different treatment conditions was demonstrated by SPR. In order to conduct the experiment, we have defined the molecular weight of NETs as 100 bp to estimate the molar concentration of NETs. **(I)** *Slc12a2*$^{fl/fl}$ or *Lgr5*^{Cre}- *Slc12a2*$^{fl/fl}$ mice were given a daily subcutaneous injection of 50 μg/kg estrogen for 21 days. Representative macrophotographs of uterus in each group (scale bar, 0.5 cm); Representative images of H&E staining (n=5, scale bar, 50 μm). **(J)** Uterus weight of each group (n=5), $^{**}P<0.01$. **(K)** Statistics of the area ratio of gland to stroma according to H&E images (n=5), $^{**}P<0.01$.



Treatment	Site of HMGN2	Sequence	Acetylated peptide(%)
DMSO	K64	ADAGK(Ac)EGNNPAENGDAK	Undetected
	K82	TDQAQK(Ac)AEGAGDAK	Undetected
Aspirin	K64	ADAGK(Ac)EGNNPAENGDAK	16.3
	K82	TDQAQK(Ac)AEGAGDAK	78.7

Figure 6. Aspirin attenuates EH in cynomolgus monkey through inhibiting NETs via HMGN2 acetylation.

(A) Experimental workflow for screening NETs inhibitor from FDA-approved drug library. The neutrophils from peripheral blood of human were incubated with 50 nM or medium at 37℃ for 2 h. The MPO level in the cell supernatant was measured. **(B)** Inhibitory rates of NETs of log10 conversion for screened compounds. **(C)** Female cynomolgus monkeys were subcutaneous injection with estradiol (32 μg/kg) per day for 5 weeks. Aspirin (5 mg/kg) was i.p. injected followed by estrogen injection. Abdominal ultrasound of cynomolgus monkey reveals endometrial thickness on the fifth week (unit: cm) (n=7). **(D)** Statistics of the endometrial thickness according to the data of

abdominal ultrasound (n=7). **(E)** H&E staining for endometrial tissue of Cynomolgus monkeys, Scale bar: 80 μm. **(F)** UMAP plot of monkey uterus cell map, colored by sample groups. **(G)** Overall transcriptome correlations among the three groups. Average gene expression calculated from scRNA-seq data for each group were used for correlation analysis. **(H)** Heatmap showing the expression pattern of marker genes in each group. **(I)** H&E images of monkey uterine tissues (left), and expression pattern of *SLC12A2* overlaying on the ST spots (right). **(J)** Immunohistochemistry analysis of NKCC1 in monkey uterine tissues, Scale bar: 80 μm. **(K)** Recombinant HMGN2 protein was incubated with aspirin (5 mM) for 1 h at 30°C. Shown is immunoblot analysis of HMGN2 acetylation with a pan-acetyl-lysine antibody. **(L)** HEK-293T cells were treated with DMSO or aspirin (5 mM) for 24 h, and HMGN2 was immunoprecipitated. HMGN2 acetylation was analyzed by immunoblotting with pan-acetyl-lysine antibody. **(M)** Recombinant HMGN2 protein was incubated with aspirin (5 mM) for 1 h at 30°C. Identification of K64 and K82 on HMGN2 by 5600+ NanoLC/Triple TOF. **(N)** HL60 cells transfected with the indicated constructs were treated with estradiol or aspirin for 24 h. OD_{450} value reflects the level of MPO-DNA Complexes in lysates, $^{**}P<0.01$, $^{*}P<0.05$.

Acknowledgements

This work was supported by National Natural Science Foundation of China (Nos. 82374113, 82404639, 32122035), Natural Science Foundation of Jiangsu Province (BK20241249) and Zhejiang Clinovation Pride (Grant No. CXTD202501010).

Author contributions

Yang Sun, Qiang Xu, Dijun Chen, Yan Li and Wen Lv conceived and designed the project. Jiao Qu, Tao Zhang, Wei Liu, Yan Ding, Yuyu Zhu, Zijun Ouyang, and Haiyan Sun performed NETs quantification, immunohistochemistry, immunoblotting, immunofluorescence staining, ELISA, cell culture and the mouse/monkey experiments. Wen Fang, Xianjia Qi and Dijun Chen performed the data analysis of scRNA-seq, scATAC-seq, CITE-seq and ST-seq. Wen Lv, Songjun Liu, Tian Xu and Haibo Cheng provided samples from patients for clinical data analysis. Yang Sun and Jiao Qu wrote this manuscript. All authors discussed the results and commented on the manuscript.

Competing interests

The authors declare no competing interests.

Materials and Methods

Patients and tissue samples

The study and protocols were carried out in accordance with the ethical guidelines of the 1975 Declaration of Helsinki Principles and were approved by the Ethics Institutional Review Board of Tongde Hospital of Zhejiang Province (Study number: 2020-002, 2021-013) and Research and Ethical Committee of Affiliated Hospital of Nanjing University of Chinese Medicine and complied with all relevant ethical regulations (2020-NL-094-02).

Animal experiments

Mice

The neutrophil cell-specific *Pad4* knockout mice (*S100a8-Cre*; $Pad4^{flox/flox}$), epithelial cell-specific *Slc12a2* knockout mice ($Lgr5\text{-}Cre^{ERT}$; $Slc12a2^{flox/flox}$), *Hmgn2* knockout mice, *Timm8b* knockout mice, neutrophil cell-specific *Esr1* knockout mice (*S100a8-Cre*; $Esr1^{flox/flox}$) and eight-week-old female C57BL/6 mice were purchased from GemPharmatech Co. Ltd. and maintained in specific pathogen-free conditions at GemPharmatech Co. Ltd. and the Experimental Animal Center at Nanjing University or Experimental Animal Center at Zhejiang Academy of Traditional Chinese Medicine. with access to food and water ad libitum. The animal procedures were approved by the National Institutes of Medicine Guidelines for the Care and Use of Laboratory Animals and the Nanjing University Animal Care and Use Committee (IACUC-2012011) and Laboratory Animal Ethics Review Zhejiang Academy of Traditional Chinese Medicine (2022-044). Age- and sex-matched mice (6-10 weeks of age) were used. Mice were

randomly assigned after acclimation for 7 days. Immunodeficient NOD/ShiLtJGpt-Prkdcem26Cd52Il2rgem26Cd22 (NCG, GemPharmatech Co. Ltd., T001475) mice were used for creation of human immune system (HIS) mice as previously described [1]. Briefly, we used CD34 Microbead Kit (Miltenyi Biotec, Cat: 130-046-702) to purify human $CD34^+$ cells from fetal liver under clinical ethical approval from Drum Tower Hospital with informed consent (protocol# 2021-488-01). NCG pups within 7 days of birth were sub-lethally irradiated and engrafted with $CD34^+$ cells by intrahepatic injection. B6.129S2-Ighmtm1Cgn/J (mμMt) mice were obtained from The Jackson Laboratory (002288). HIS mice and mμMt mice were housed under specific pathogen-free (SPF) conditions with humane care in Model Animal Research Center of Nanjing University. All experiments were approved by an Institutional Animal Care and Use Committee (IACUC) at the Model Animal Research Center of Nanjing University (AP# LY-01). To ensure a uniform starting point, before the formal experiment we synchronized the mice by strictly screening estrous stage using vaginal cytology, and only mice in proestrus were enrolled for estrogen induction, because at this stage the endometrium is in a physiological proliferative state with the most sensitive and consistent response to estrogen. For EH induction in mice, 50 μg/kg estradiol was subcutaneously (s.c.) injected into mice for 20 successive days. To generate the other groups, 4 mg/kg GSK484 or 5 mg/kg aspirin was intraperitoneally (i.p.) injected followed by estradiol injection. Mice were sacrificed one day after the last treatment. Uterine tissues were harvested for hematoxylin and eosin (H&E), immunocytochemistry, immunofluorescence and ELISA analyses.

Monkeys

Healthy female cynomolgus monkeys ranging from 3 to 5 years in age were raised in the monkey breeding base of Changchun Biotechnology Development Co., Ltd., Guangxi, China. The sample collection of cynomolgus monkeys and research conduction in this study were approved by the Research Ethics Committee of Changchun Biotechnology Development Co., Ltd. (Approval Number: 200010). The monkey management protocols were carried out in accordance with the standard procedures of Changchun Biotechnology Development, referring to the Guide for Care and Use of Laboratory Animals (2010) and the principles of Animal Welfare Management (Public Law 99-198). The monkeys were coded and randomly divided into three groups. For EH induction, 32 μg/kg estradiol was s.c. injected into cynomolgus monkeys for 5 successive weeks. To generate the other groups, 3.2 mg/kg aspirin was i.p. injected followed by estradiol injection. Serum was collected from cynomolgus monkeys every week for experiments.

Cell culture

Human endometrial epithelial cell line was purchased from Qingqi (Shang hai) Biotechnology Development Co.Ltd. HL-60 cell cell line was purchased from Wuhan Pricella Biotechnology Co., Ltd. All cells were cultured in DMEM (2051245, Biological Industries, Israel) containing 10% fetal bovine serum (2033119, Biological Industries, Israel) and 1% penicillin–streptomycin (C0222, Beyotime, China) in an incubator at 37 ℃ with 5% CO_2. HL-60 cells (Procell, Wuhan, China) was cultured in RPMI 1640 with 10% FBS. HL-60 were differentiated with 1.3% DMSO, and

transfection was initiated on the 7th day of differentiation. As for HL-60 cells transfection, cells were transfected with 2 μg DNA by electroporation (btx Gemini X, pCMV3- HMGN2-GFP-Puro-3×Flag or HMGN2 mutant plasmids were purchased from Corues Biotechnology). The materials involved in the experimental section are summarized in **Supplementary Table 2**.

Neutrophil isolation

Neutrophils were isolated from the peripheral blood of healthy donors using Ficoll-Hypaque density gradient centrifugation according to the instructions of the Human Neutrophil Isolation Kit (LZS11131, Haoyang Biology, China). Briefly, anticoagulant and hydroxyethyl starch were mixed for erythrocyte sedimentation and then gently superimposed on the neutrophil separation solution followed by centrifugation at 800 *g* for 20 min. The neutrophil layer was pipetted out, subsequently purified, centrifuged and resuspended.

NET purification

NETs were extracted according to previously described methods [2]. After overnight incubation with estradiol, the culture medium was removed and a restriction enzyme mix containing BseRI, PacI, NdeI, and AflII (5 U/ml in Cut Smart NEB buffer) was added and incubated at 37°C for 30–60 min to achieve partial NET enzymatic digestion. NET DNA concentration was determined using Quant-iT PicoGreen dsDNA Reagent after Proteinase K treatment (100 μg/ml for 2 hours at 56°C).

Live-cell imaging of NETs

Primary neutrophils were isolated from human peripheral blood or from mouse orbital venous blood and seeded into 96-well glass-bottom plates. After stimulation with the indicated agents, cells were incubated with Draq5 (2 μM) and Sytox Green (1μM) for 15 min. Imaging was then performed using the Operetta High Content Imaging System with a 20× objective. NETosis was identified by the emergence of green fluorescence.

Immunohistochemistry

The sections were deparaffinized by successive xylene and ethanol baths. Antigen retrieval and inactivation of endogenous peroxidases were performed with sodium citrate buffer and hydrogen peroxide methanol solution. Permeabilization and blocking were performed using Triton-100 and goat serum, and the sections were incubated with primary antibody at 4°C overnight. Primary antibodies against NKCC1 (1:200, Abcam, ab140986) were used. The sections were incubated with streptavidin-HRP (KIHC-5, Proteintech Group, USA) and then treated with diaminobenzidine (DAB, Proteintech Group, USA) as a visualization agent. Hematoxylin was used as the counterstain to observe the nucleus. Finally, the slides were imaged by a light microscope (IX61, Olympus, Japan).

Immunoblotting

Samples were loaded and separated on 10% sodium dodecyl sulfate (SDS)-polyacrylamide gels and then transferred to polyvinylidene fluoride (PVDF) membranes (IPVH00010, Merck Millipore, Germany). Membranes were incubated with 5% BSA blocking buffer, and primary antibodies were added and incubated at 4°C overnight. Primary antibodies against NKCC1 (1:1,000, Santa Cruz, sc-514774) and β-

795 actin (1:2000, Abmart, M20011) were used. Secondary antibodies were incubated with
796 membranes at room temperature for 2 h. LumiGLO® Reagent and 20× Peroxide (7003,
797 Cell Signaling Technology, USA) were used to detect and expose protein bands. To
798 detect HMGN2 acetylation, HEK-293T and HeLa cells were lysed in lysis buffer (20
799 mM Tris pH7.5, 150mM NaCl, 1% Triton X-100, 3 mM EDTA, 3 mM EGTA, 2 mM
800 dithiothreitol) supplemented with complete protease inhibitor cocktail, followed by
801 centrifugation at 16,000 *g* for 10 min at 4°C. The supernatants were
802 immunoprecipitated with HMGN2 antibody for 12 h at 4°C. The immunoprecipitants
803 were washed six times with TBST buffer and boiled in 1×SDS-loading buffer for
804 immunoblot analysis.

805 **Immunofluorescence staining**

806 The paraffin-embedded sections were deparaffinized and rehydrated in successive
807 xylene and ethanol baths. We subjected the sections to heat-induced epitope retrieval
808 methods, followed by inactivation of endogenous peroxidase. Triton-X 100 and goat
809 serum were applied, and then the sections were incubated with the indicated antibodies
810 overnight at 4°C. The next day, the sections were treated with Alexa Fluor-labeled
811 secondary antibodies (A11034 and A21424, Thermo Fisher Scientific, USA;
812 HYDS0045, Shanghai Guduo Technology Co. Ltd., China) and then treated with DAPI
813 staining solution (C1002, Beyotime, China) for nuclear visualization. Chromogenic
814 immunodetection was employed using an inverted confocal microscope (Zeiss LSM
815 880 with Airyscan, Carl Zeiss, Germany) or 3D Histech (*Hungary*).

816 Neutrophils at the bottom of the dishes were treated with poly-L-lysine for 15 min,

followed by Triton-X 100 and goat serum administration. Neutrophils were incubated with a the indicated antibodies overnight at 4°C. The next day, Alexa Fluor-labeled secondary antibodies were applied to the dishes and incubated for 2 h, followed by DAPI staining for 15 min. Chromogenic immunodetection was employed using an inverted confocal microscope.

Isolation of cell membrane proteins

Cell membrane proteins were isolated with a Cell Surface Protein Isolation Kit (Abcam, ab206998). After washing the cells, Sulfo-NHS-SS-Biotin was used for biotinylation. Thereafter, lysis buffer with protease inhibitors was added for 30 min with vortexing every 15 min. Streptavidin beads were incubated with the supernatant at room temperature for 1 h with end-over-end mixing on a rotator. After 3 bead washes, elution buffer (10% DTT) was used for cell membrane protein elution.

Biotinylation of NET-DNA

Biotinylation of NET-DNA was performed with a Biotin 3' End DNA Labeling Kit (Beyotime, D3106). In brief, NET-DNA, TdT buffer, TdT, and Biotin-11-dUTP were mixed together at room temperature for 30 min. After termination of the probe labeling reaction, chloroform isoamyl alcohol (24:1) was added to extract TdT. During this process, vortexing is required to fully mix the organic phase with the aqueous phase. After 14,000 *g* centrifugation, the biotin-labeled NET-DNA was obtained in the supernatant.

Biotinylated NET-DNA pull-down

DNA pull-down was performed as previously described. In brief, cell membrane

protein was incubated with 200 ng biotinylated NET-DNA in 200 μl immunoprecipitation (IP) lysis buffer (P0013, Beyotime) at room temperature for 1 h. Next, the protein-DNA complex was incubated with 50 μl streptavidin-agarose beads at room temperature for another 1 h. The beads were then washed 3 times with IP lysis buffer and separated through gradient gel electrophoresis followed by silver staining or Western blotting. The band was identified by liquid chromatography coupled with mass spectrometry.

cfDNA quantification

cfDNA levels in serum were quantified using a Quant-it PicoGreen dsDNA Assay kit (P7581, Thermo Fisher Scientific, USA) in accordance with the manufacturer's instructions. Briefly, dilutions of dsDNA standards and samples were incubated for 5 min with 1 mL of Quant-it PicoGreen reagent. Fluorescence signals were measured in a microplate fluorescence reader (Safire, Tecan, Switzerland) with an excitation wavelength of 480 nm and an emission wavelength of 520 nm.

ELISA

The protein level was detected by an ELISA kit (R&D System Duoset). Briefly, the capture antibody was coated in a 96-well enzyme-linked immunoassay (EIA) plate (Costar 3590, Corning Incorporated, USA). After 3 washes with PBST, the samples were incubated for 2 h and discarded. The detection antibody was added and incubated for 2 h. The absorbance at 450 nm was measured to quantify the levels of NE and MPO using a microplate fluorescence reader (Safire, Tecan, Switzerland).

MPO-DNA ELISA

Anti-MPO capture antibody (DY3174, R&D System, USA) was coated in a 96-well EIA plate (Costar 3590, Corning Incorporated, USA). Samples were incubated with a peroxidase-labeled anti-DNA monoclonal antibody from a Cell Death Detection ELISA kit (11544675001, Roche, USA) following the manufacturer's instructions. The absorbance at 450 nm was measured to quantify the association between MPO and DNA by a microplate fluorescence reader (Safire, Tecan, Switzerland).

MPO activity assay

MPO activity in the serum of cynomolgus monkeys was detected by the Myeloperoxidase Activity Assay Kit (ab105136, Abcam, USA). According to the manufacturer's instructions, samples and MPO substrate were incubated for 2 h at 25°C. Subsequently, the reaction was stopped, and TMB was added for the color reaction. The absorption was measured at 412 nm with a microplate fluorescence reader (Safire, Tecan, Switzerland). MPO activity was calculated as units/mL based on a standard curve.

H&E staining

Briefly, after removal of the embedding agent and rehydration, tissue sections were stained with hematoxylin solution (G1005, Servicebio, China) for 8 min. Then, sections were dehydrated with ascending concentrations of alcohol, and eosin staining was performed for 10 min (G1005, Servicebio, China). Neutral balsam was used to seal the sections.

Organoid culture

All endometrial organoids were constructed and cultivated by Chongqing Kingbiotech

Co., Ltd. Patient tissue samples acquired by surgical operation were minced into as small as possible pieces by sterile scissors. The tissue pieces were mixed thoroughly with Matrigel (Corning, NY, USA) at an approximate ratio of 1:4 on ice. The tissue-Matrigel solutions were seeded quickly in the multiwell plate to form hemispherical droplets and transferred to 37°C for 15-20 min, allowing the droplets to solidify. Then, the appropriate amount of culture medium (Kingculture^{TM} Organoid Growth Medium, catalog No. KCW-12) was added to each well and changed every 2-4 days.

Microscale thermophoresis (MST)

HEK293T cells were transfected with GFP-NKCC1 plasmids and were lysed after 48 hours. NETs treated under different conditions (unprocessed NETs, NETs treated to 0.05% trypsin at 37°C for 30 minutes, and NETs treated with 125 ug/ml DNase I for 2 hours.) serve as ligands and are diluted by half. Subsequently, they are mixed with an equal volume of cell lysate to achieve a final fluorescence intensity of 400. The experiment was performed utilizing the Monolith NT.115 instrument, with the subsequent data analysis conducted through the MO.Affinity Analysis software.

Surface Plasmon Resonance (SPR)

The human recombinant NKCC1 protein, acquired from MCE, served as the ligand and was coupled to the sensor chip. A series of analytes with differing concentrations of NETs were prepared in electrophoresis buffer. The comprehensive experimental procedures have been previously outlined.

Tissue processing and spatial transcriptomics

Endometrial tissues were obtained from Tongde Hospital of Zhejiang Province. we

905 performed scRNA-seq, scATAC-seq, and ST-seq of endometrial tissue. For scRNA-seq
906 and scATAC-seq, endometrial tissues are derived from biopsy tissue samples. After
907 collection, all of the samples were rinsed with DMEM on a Petri dish to remove blood
908 and mucus before dissociation and other follow-up experiments. Then the tissues were
909 firstly cut into 1-2 mm^3 pieces in DMEM with 12% fetal bovine serum (FBS, Gibico),
910 then enzymatically digested with gentleMACS (Miltenyi) according to manufacturer's
911 instruction. Cells were passed through a 70 μm cell trainer (Miltenyi) and centrifuged
912 at 300 *g* for 5 min at 4°C. The pelleted cells were re-suspended in red blood cell
913 lysisbuffer (Beyotime) and incubated 1 min to lyse red blood cells. After wash twice
914 with PBS (Gibico), the cell pellets were re-suspended in sorting buffer (PBS with
915 supplemented with 1% FBS). Single cells were captured by the BD Rhapsody by
916 NovelBio Bio-Pharm Technology Co., Ltd. (Shanghai, China). scRNA-seq library was
917 conducted by Shanghai Xuran Biotechnology and scATAC-seq library was conducted
918 by LC-Biotechnology (Hangzhou, China) and prepared following the manufacturer's
919 protocol (10× Genomics). For ST-seq, the tissues were obtained from patients
920 undergoing total hysterectomy and the tissues were cut longitudinally. Endometrial
921 tissue was carefully dissected from the myometrium, and the overlying vertical
922 endometrial region was preserved. The tissues were washed in cold PBS. The tissues
923 were placed in a histology plastic cassette and snap frozen for 1 min in a bath of liquid
924 nitrogen-cooled isopentane. The frozen tissue was then embedded in Optimal Cutting
925 Temperature compound (OCT, Sakura Tissue-TEK) on dry ice. Then, we transferred
926 the slice sections to fit the 6.5 mm^2 oligo-barcoded capture areas on the Visium 10×

Genomics slide. Visium Spatial Tissue Optimization (10× Genomics) was performed according to the manufacturer's instructions. Sequence libraries were then processed according to the manufacturer's instructions (10× Genomics, Visium Spatial Gene Expression Slide & Reagent Kit).

Cellular indexing of transcriptomes and epitopes by sequencing (CITE-seq)

The fresh blood samples were immediately subjected to PBMCs isolation using standard density gradient centrifugation. PBMCs were isolated using ficoll solution according to the manufacturer's instructions. The tissue samples were processed as described below. Briefly, samples were first washed with phosphate-buffered saline (PBS), minced into small pieces (about 1 mm^3) on ice and enzymatically digested with 2 mg mL^{-1} collagenase IV, 50 U mL^{-1} DNase I, and 10% Fetal Bovine Serum for 40 min at 37℃, with agitation. After digestion, samples were sieved through a 70 μm cell strainer, and centrifuged at 400 *g* for 5 min. After washing with PBS containing 0.04% BSA, the cell pellets were re-suspended in PBS containing 0.04% BSA and re-filtered through a 35 μm cell strainer. Dissociated single cells were then stained with AO/PI for viability assessment using Countstar Fluorescence Cell Analyzer. Then single cells from the tissue were resuspended in PBS and stained for CD45 for 30 min on ice for flow cytometry and FACS, cells FACS and cytometry was performed on a BD FACS Melody™ and sorted $CD45^+$ cells were collected in RPMI-1640 supplemented with 10 % FBS. Abseq surface antibody libraries (Supplementary Table 1) were pipetted 24 h before experiments. For most antibodies, 1 μl was used for surface library preparation. Antibodies recognizing epitopes with well-known high surface expression were further

diluted in PBS and 1μl was added to the surface library (for example HLA ABC, CD45, CD11a). Sorted cells (around 1.2×10^5–1.4×10^5; described in Cell sorting for Abseq) were centrifuged 5 min at 350 *g* and resuspended in the surface library mix. BD Rhapsody system was used to capture the transcriptomic information of the (endometrium and blood sample-derived) single cells. Single-cell capture was achieved by random distribution of a single-cell suspension across >200,000 microwells through a limited dilution approach. Beads with oligonucleotide barcodes were added to saturation so that a bead was paired with a cell in a microwell. Cell-lysis buffer was added so that poly-adenylated RNA molecules hybridized to the beads. Beads were collected into a single tube for reverse transcription. Upon cDNA synthesis, each cDNA molecule was tagged on the 5′ end (that is, the 3′ end of a mRNA transcript) with a unique molecular identifier (UMI) and cell label indicating its cell of origin. Whole transcriptome libraries were prepared using the BD Rhapsody single-cell whole-transcriptome amplification workflow. In brief, second strand cDNA was synthesized, followed by ligation of the WTA adaptor for universal amplification. Eighteen cycles of PCR were used to amplify the adaptor- ligated cDNA products. Sequencing libraries were prepared using random priming PCR of the whole-transcriptome amplification products to enrich the 3′ end of the transcripts linked with the cell label and UMI. Sequencing libraries were quantified using a High Sensitivity DNA chip (Agilent) on a Bioanalyzer 2200 and the Qubit High Sensitivity DNA assay (Thermo Fisher Scientific). The library for each sample was sequenced by illumina sequencer (Illumina, San Diego, CA) on a 150 bp paired-end run. The CITE-seq

971 experiment was conducted by NovelBio Bio-Pharm Technology Co., Ltd. (Shanghai,
972 China).

973 **ChIP assay**

974 Neutrophils isolated from the peripheral blood of healthy donors were treated with
975 medium, estradiol and aspirin for 2 h. Then, the cells were cross-linked with 1%
976 formaldehyde for 10 min at room temperature. Crosslinking was neutralized with 0.125
977 M glycine for 5 min. Formaldehyde was removed, and the cells were washed twice with
978 PBS. Briefly, cells were lysed in lysis buffer LB1, LB2 and LB3. Chromatin was
979 incubated with antibody at 4°C overnight following sonication. Subsequently, the
980 protein A/G was added to each ChIP reaction, and the chromatin was eluted and
981 reversed crosslinked, followed by DNA purification. The extracted DNA was used for
982 ChIP-seq.

983 ***In vitro* acetylation and mass spectrometry assays**

984 Recombinant Human Non-histone chromosomal protein HMG-17 (HMGN2) were
985 purchased from CUSABIO. The acetylation assay was performed by incubating
986 recombinant HMGN2 protein in reaction buffer (20 mM Tris-HCl pH8.0, 20% Glycerol,
987 100 mM KCl, 0.2 mM EDTA, 1 mM DTT) according to the previous research. After
988 incubation for 1 h at 30°C, the reaction was stopped by SDS-loading buffer for
989 immunoblot analysis. To identify HMGN2 acetylation and quantification of aspirin
990 induced HMGN2 acetylation change, MS analysis of digested peptides was carried out.
991 In brief, desalted peptides were analyzed using a TripleTOF 5600+ NanoLC mass
992 spectrometer (AB Sciex) coupled to an ekspert nanoLC 425 (Eksigent). TripleTOF

5600+ raw data were performed against ProteinPilot software. The percentage of acetylation was calculated by peptides counts.

Flow cytometry

After digestion of endometrial tissue and the single-cell suspension was prepared. Surface staining was performed with surface antigen antibodies in the flow cytometry buffer (PBS containing 1% FBS) and stained on ice with appropriate antibodies for 30 min. Pellets were washed and suspended in fresh flow cytometry buffer prior to analysis.

Target discovery via a target-responsive accessibility profiling approach

Target discovery via a target-responsive accessibility profiling approach (TRAP) was used to explore the binding proteins. Two dishes of neutrophils were treated with 50 nM estradiol or 5 μM aspirin plus 50 nM estradiol. After 1 h incubation, cells were permeabilized by M-PER buffer and the resultant lysates were covalently labeled by the addition of formaldehyde and borane pyridine complex that together specifically label proteinaceous lysine residues at room temperature for accessibility profiling. More detailed information can be found in the previous literature [3].

Cellular thermal shift assay

The neutrophils were treated with estradiol or eatradiol plus aspirin for 6 h. The cells were collected, washed with cold PBS, and centrifuged at 180 *g* for 5 min. The cells were then evenly divided into centrifugation tubes and heated for 3 min at the following temperature: 46, 49, 52, 55, 58, and 61°C, the samples were cooled for 3 min at temperature and then kept on ice. Then, the samples were placed in a refrigerator at -80°C overnight. The samples were thawed at room temperature for 30 min and then

refrigerated at -80°C for 4 h. Finally, the samples were centrifuged at 12, 000 *g* for 25 min, the supernatant added to the loading buffer, and analyzed by Western blotting.

Analysis of intracellular ion concentrations.

For intracellular ion measurements, endometrial epithelial cells were washed 3 times with osmotically balanced solution of 150 mM LiCl (300 mOsm). The cells were Freeze-thaw repeatedly to lyse cells and then lysed overnight at 4°C in 1% HNO_3. The intracellular Na^+, Cl^- and K^+ concentrations were measured using an analytik jena novAA350/ZEEnit650p Atomic Absorption Spectrometer.

Plasmid DNA transfection.

Endometrial epithelial cells were seeded for 12hours, and then transfected with pLV3-CMV-SLC12A2-mCherry-Puro(Related plasmids were purchased from Miaoling Biology). HL-60 cells were transfected by electroporation (btx Gemini X, pCMV3-HMGN2-GFP-Puro-3×Flag or HMGN2 mutant plasmids were purchased from Corues Biotechnology).

Statistical analysis

Statistical analysis was performed using GraphPad Prism 9.0. Thank you for pointing out our mistake. Statistical analyses were performed by using GraphPad Prism 8 software. Data are presented as mean ± SEM. One-way analysis of variance (ANOVA) with Tukey's multiple comparisons test was used to evaluate statistical significance for group comparisons. Differences at $*p < 0.05$ and $**p < 0.01$ were accepted as statistically significant.

Computational analysis

scRNA-seq of clinical samples using BD Rhapsody

The scRNA-seq data of clinical samples generated in this study were performed on the BD Rhapsody system. Single-cell capture was achieved by random distribution of a single-cell suspension across >200,000 microwells through a limited dilution approach. Beads with oligonucleotide barcodes were added to saturation so that a bead was paired with a cell in a microwell. The cells were lysed in the microwell to hybridize mRNA molecules to barcoded capture oligos on the beads. Beads were collected into a single tube for reverse transcription and ExoI digestion. Upon cDNA synthesis, each cDNA molecule was tagged on the 5′ end with a unique molecular identifier and cell barcode indicating its cell of origin. Whole transcriptome libraries were prepared using the BD Rhapsody single-cell whole-transcriptome amplification (WTA) workflow including random priming and extension (RPE), RPE amplification PCR and WTA index PCR. The libraries were quantified using a High Sensitivity DNA chip (Agilent) on a Bioanalyzer 2200 and the Qubit High Sensitivity DNA assay (Thermo Fisher Scientific). Sequencing was performed by illumina sequencer (Illumina, San Diego, CA) on a 150 bp paired-end run.

scRNA-seq of mouse and monkey samples using 10× Chromium

The scRNA-seq data of mouse and monkey samples generated in this study were performed on the 10× Chromium platform using Next GEM single cell 3'GEM Kit V3.1 according to the manufacturer's protocols including sample preparation, library preparation and instrument and sequencing settings. All libraries were sequenced on

the NextSeq 500 platform (Illumina) with paired-end sequencing and dual indexing.

scATAC-seq using 10× Chromium

The scATAC-seq data generated in this study were performed on the Next GEM single cell ATAC Gel Beads V1.1according to the manufacturer's protocols including sample preparation, library preparation and instrument and sequencing settings. All libraries were sequenced on the NextSeq 500 platform (Illumina) with paired-end sequencing and dual indexing.

scRNA-seq data processing, cluster annotation and data integration

Raw scRNA-seq data from human samples were processed using fastp (v.0.19.7) with default parameters to filter adaptor sequences and remove low-quality reads, obtaining clean data [4]. UMI-tools (v.1.0.0) was applied for single-cell transcriptome analysis to identify the cell barcode whitelist [5]. The UMI-based clean data were mapped to the human genome (Ensemble version 91) using STAR (v.2.7.11) mapping with customized parameters from the UMI-tools standard pipeline to obtain the UMI counts for each sample [6]. Raw scRNA-seq data of mouse and monkey samples were processed using the Cell Ranger (v.3.1.0) software (10× Genomics) for read alignment, barcode assignment and unique molecular identifier (UMI) counting, based on corresponding reference genomes (mouse mm10-3.0.0, monkey macFas5). Cells were filtered with a UMI count greater than 200 and a mitochondrial percentage less than 20%. Filtered data were then log normalized and scaled, with cell-cell variation due to UMI counts and percent mitochondrial reads regressed out using Seurat (v.4.0.4) [7]. To avoid batch effects among samples and experiments, Seurat's robust principal component analysis

(RPCA) integration tool was used to integrate single-cell data. Dimensionality reduction was performed with "RunUMAP" function and visualized by Uniform Manifold Approximation and Projection (UMAP). Cell clustering was performed by "FindClusters" function at a resolution of 0.2 and the top 30 principal components (PCs) were used to define cell identity. Marker genes for each cluster were performed using the Wilcoxon rank-sum test ("FindAllMarkers" function with default parameters) and each cell clusters were annotated based on known maker genes the top gene list.

Identification of neutrophil subsets

The neutrophils were extracted from the integrated cell map and re-clustered using the "RunUMAP" function based on the first 30 PCs. Neutrophil subsets were determined by the "FindClusters" function at a resolution of 0.2. In total, five different subclusters were identified.

Gene-set enrichment analysis

All the gene-set enrichment analyses (GSEA) in this study were performed by the clusterProfiler package (v.3.14.3) in R [8].

Pseudotime analysis

The R package Monocle2 (version 2.14.0) was used to reconstruct the neutrophil developmental trajectory [9]. The UMI count matrix was used as input and variable genes obtained from the neutrophil cell cluster were used to sort cells in pseudotime analysis. The neutrophil cluster 5 (Neus5) was defined as the root state since the developmental potential of this cell cluster showed the highest value based on CytoTRACE analysis [10].

Single-cell gene regulatory network inference

Gene regulatory network (GRN) modules were inferred using the SCENIC workflow (v0.10.0; a Python implementation of SCENIC) [11]. First, raw expression data were normalized by dividing feature counts of each cell by the total counts for that cell and multiplying by a factor of 10,000, followed by log1p transformation. Next, normalized counts were used to generate co-expression modules using the GRNboost2 algorithm implemented in the arboreto package (v.0.1.3). Finally, co-expression modules were inferred using pySCENIC (with default parameters) and were filtered using cis-regulatory motif analysis (RcisTarget, using hg38 motif collections) to retain only modules enriched for putative direct-binding targets of the corresponding transcription factor (TF), and remaining modules were pruned to remove targets lacking motif support, resulting in a matrix of AUCell values that represent the activity of each regulon in each cell. The final gene regulatory networks consisted of 196 regulons for the datasets each group. GRNs were visualized using igraph (v.1.2.6) package in R.

Spatial transcriptomics data processing

Space Ranger (v.1.1.0) software (10× Genomics) was used to process, align and summarize UMI counts against the GRCh38 human reference genome and macFas5 monkey reference genome respectively for each spot on the Visium spatial transcriptomics array. Raw spot count matrices were filtered out to keep only spots overlaying tissue sections. In order to account for variability in total spot RNA content, count matrices were normalized using regularized negative binomial regression (SC Transform) [12] Dimensionality reduction was performed using PCA and for each slide.

Clustering was performed using Louvain clustering algorithm (resolution=1.0) and clusters were visualized using UMAP algorithm. Clusters distributions were visualized in spatial context over H&E images.

Cell type decomposition analysis of spatial transcriptome data

Conditional autoregressive-based deconvolution (CARD) was used to map the cell types found in the reference scRNA-seq dataset to spatial transcriptomic data[13]. Marker genes for each cell type were obtained using the Seurat function FindAllMarkers, whereby only markers with positive log2-transformed fold changes were considered. We then followed the standard CARD analysis pipeline on the reference and Visium spatial transcriptomics data in doublet mode set to full.

Co-location analysis of spatial transcriptome data

To investigate potential physical proximity and microenvironmental interactions among key cell populations in tissue sections, we performed pairwise co-localization analysis using spatial transcriptomic data generated by the 10x Genomics Visium platform. Specifically, we examined spatial relationships between $ESR1^+$ neutrophils and $NKCC1^+$ epithelial cells. For each cell type in a pair, we selected the top fraction of spots ranked by their CARD-inferred cell-type proportions, while excluding spots with zero contribution. These selected spots were considered spatially enriched for the corresponding cell type. Spatial coordinates of these selected spots were retrieved using Seurat's GetTissueCoordinates function and rescaled to micrometer units based on the spot diameter and image scale factors provided by the Visium platform. Pairwise nearest-neighbor distances between the selected spots of two cell types were calculated

bidirectionally using the FNN package (get.knnx, k = 5, kd-tree algorithm). For each spot, we computed the average distance to its k nearest neighbors from the other population. Spots were annotated into one of the following categories:

- Cell type A: proximity only to cell type A,
- Cell type B: proximity only to cell type B,
- Co-localization: spatially proximal (< threshold distance, e.g., 100 μm) to both cell types.

This annotation was added to the Seurat object metadata and visualized using SpatialDimPlot. The analysis was applied across multiple tissue sections to identify consistent spatial patterns of co-localization. Counts of co-localized spots were summarized for comparative analysis across samples or conditions.

scATAC-seq sequencing data processing

scATAC-seq data were processed using Cell Ranger ATAC (v.1.2.0) software (10× Genomics), which generated a count matrix for open chromatin regions in single cells after barcode processing, alignment, duplicate marking, peak calling and cell calling. Human reference genome version GRCh38 and monkey custom reference genome macFas5 were used in alignment process, respectively. Downstream analyses were performed with the ArchR workflow (version 1.0.1) [14]. In brief, we filtered out cells with less than 1,000 unique fragments and transcriptional start site (TSS) enrichment score below 4 so that the remaining cells had adequately sequenced reads and high signal-to-background ratio. Then, we filtered doublets with the ratio of predicted

doublets to filter based on the number of pass-filter cells less than 1. Finally, scATAC-seq clustering was performed using Seurat's "FindClusters" function. We used SVD on the TF-IDF matrix to generate a lower-dimensional representation of the data by retaining the first 50 dimensions. We then used these reduced dimensions as input into a Seurat object and then final clusters were identified by Seurat's SNN graph clustering "FindClusters" with a resolution of 0.3.

Defining cluster identity of scATAC-seq data

We annotated each cell clusters using three different approaches: (1) chromatin accessibility of *cis*-elements (i.e., ATAC-seq peaks); (2) gene activity scores, computed from the accessibility of putative enhancers linked to the target gene promoter; and (3) TF activity, computed from the accessibility of TF binding sites genome-wide in each single cell.

Gene-activity scores and co-accessibility

We calculate co-accessibility using the "addCoAccessibility" function with the default parameter. Loop tracks of 10000 bp upstream and downstream of specific genes were drawn.

Measuring TF activity

The global TF activity was calculated using ChromVAR. Briefly, the CIS-BP motif database was added to existing ArchR objects with the "addMotifAnnotations" function. The GC bias-corrected deviation scores were then computed using the chromVAR "deviationScores" function after adding a set of background peaks with the "addBgdPeaks" function. Finally, the deviation value for each cell was calculated with

the “addDeviatonMatrix” function.

ChIP-seq sequencing data processing

Raw sequencing data were cleaned to filter adapters and low quality reads using FASTQC (v0.11.5) and the unique mapped reads were harvested by mapping the cleaned reads to genome with no more than two mismatches by Bowtie 2. MACS2 (v2.1.1) was used to call peak, giving a robust and high resolution ChIP-Seq peak predictions. Peaks were annotated related genes using Homer (v4.10). deepTools (v2.4.1) was used to plot gene coverage of the reads near TSS and TES. ChIPseeker (v1.5.1) was used to depict the reads distribution on chromosomes. Homer (v4.10) was used to search motif and analyze transcription factors.

CITE-seq sequencing data processing

Fastq files were processed via the standard Rhapsody analysis pipeline (BD Biosciences) on Seven Bridges (https://www.sevenbridges. com) according to the manufacturer's recommendations. The resulting unique molecular identifier (UMI) count matrices were imported into R (v.4.0.0) and processed with the R package Seurat (v.4.0.4). To account for differences in sequencing depth across cells, both layers were normalized independently using Seurat defaults. RNA UMI counts were log-normalized, while antibody UMI counts were centered using log ratio normalization to account for unspecific binding background signal. Subsequently, both normalized matrices were concatenated and integration across patients was performed using Harmony [15]. The antibodies used for CITE-seq in this study are summarized in **Supplementary Table 3**.

Data and materials availability:

The data that support the findings of this study have been deposited into Gene Expression Omnibus (GEO) with accession number:

Human (scATAC-seq): GSE223639,

https://www.ncbi.nlm.nih.gov/geo/query/acc.cgi?acc=GSE223639

Monkey: GSE223641,

https://www.ncbi.nlm.nih.gov/geo/query/acc.cgi?acc=GSE223641

Mouse: GSE223640,

https://www.ncbi.nlm.nih.gov/geo/query/acc.cgi?acc=GSE223640

ChIP: GSE223642,

https://www.ncbi.nlm.nih.gov/geo/query/acc.cgi?acc=GSE223642

The following secure token has been created to allow review while it remains in private status: kviviuooxpgtvkf.

Human (scRNA-seq, BD): GSE286093

https://www.ncbi.nlm.nih.gov/geo/query/acc.cgi?acc=GSE286093

The following secure token has been created to allow review of record GSE286093 while it remains in private status: Mxwreigwptkflcx

CITE-seq: GSE272956

https://www.ncbi.nlm.nih.gov/geo/query/acc.cgi?acc=GSE272956

The following secure token has been created to allow review while it remains in private status: ctgjomowzjwjdej.

References (methods only)

1. Ren, D., Liu, W., Ding, S. & Li, Y. Protocol for generating human immune system mice and hydrodynamic injection to analyze human hematopoiesis in vivo. *STAR Protoc* **3**, 101217 (2022).
2. Theodora-Dorita Tsourouktsoglou. *et al*. Histones, DNA, and Citrullination Promote Neutrophil Extracellular Trap Inflammation by Regulating the Localization and Activation of TLR4. *Cell Rep* **5**, 107602 (2020).

3. Tian, Y. *et al.* Chemoproteomic mapping of the glycolytic targetome in cancer cells. *Nat Chem Biol* **19**, 1480-1491 (2023).
4. Chen, Shifu. *et al.* fastp: an ultra-fast all-in-one FASTQ preprocessor. *Bioinformatics* **17**, i884-i890 (2018).
5. Smith, Tom. *et al.* UMI-tools: modeling sequencing errors in Unique Molecular Identifiers to improve quantification accuracy. *Genome research* **27**, 491-499 (2017).
6. Dobin, Alexander. *et al.* STAR: ultrafast universal RNA-seq aligner. *Bioinformatics* **29**, 15-21 (2013).
7. Satija, R., Farrell, J.A., Gennert, D., Schier, A.F. & Regev, A. Spatial reconstruction of single-cell gene expression data. *Nat Biotechnol* **33**, 495-502 (2015).
8. Yu, G., Wang, L.G., Han, Y. & He, Q.Y. clusterProfiler: an R package for comparing biological themes among gene clusters. *OMICS* **16**, 284-287 (2012).
9. Qiu, X. *et al.* Reversed graph embedding resolves complex single-cell trajectories. *Nat Methods* **14**, 979-982 (2017).
10. Gulati, Gunsagar S et al. "Single-cell transcriptional diversity is a hallmark of developmental potential." Science 6476, 405-411. (2020).
11. Aibar, S. *et al.* SCENIC: single-cell regulatory network inference and clustering. *Nat Methods* **14**, 1083-1086 (2017).
12. Hafemeister, C. & Satija, R. Normalization and variance stabilization of single-cell RNA-seq data using regularized negative binomial regression. *Genome Biol* **20**, 296 (2019).
13. Ying Ma, Xiang Zhou. Spatially informed cell-type deconvolution for spatial transcriptomics. *Nat Biotechnol.* **40**, 1349-1359 (2022).
14. Granja, J.M. *et al.* ArchR is a scalable software package for integrative single-cell chromatin accessibility analysis. *Nat Genet* **53**, 403-411 (2021).
15. Ilya Korsunsky. *et al.* Fast, sensitive and accurate integration of single-cell data with Harmony. *Nat Methods.* **16**, 1289-1296 (2019).

Supplementary Information for
Estrogen-triggered neutrophil extracellular traps fuel sterile inflammation via NKCC1

Jiao Qu[1#,*], Wen Fang[1#], Tao Zhang[1,2#], Wei Liu[3#], Yan Ding[1], Songjun Liu[4], Xinran Cao[1], Ning Wan[5], Hui Ye[5], Xianjia Qi[6], Tian Xu[7], Qiang Xu[1], Yan Li[3*], Dijun Chen[1*], Yang Sun[1,2*], Wen Lv[4*]

[1]State Key Laboratory of Pharmaceutical Biotechnology and Nanjing Drum Tower Hospital, School of Life Sciences, Chemistry and Biomedicine Innovation Center, Nanjing University, 163 Xianlin Avenue, Nanjing 210023, China; [2]Jiangsu Key Laboratory of New Drug Research and Clinical Pharmacy, Xuzhou Medical University, Xuzhou 221004, China; [3]State Key Laboratory of Pharmaceutical Biotechnology and MOE Key Laboratory of Model Animals for Disease Study, National Resource Center for Mutant Mice, Chemistry and Biomedicine Innovation Center, Model Animal Research Center, Medical School of Nanjing University, Nanjing, China; [4]Department of Gynecology, Tongde Hospital of Zhejiang Province Affiliated to Zhejiang Chinese Medical University (College of Integrated Traditional Chinese and Western Medicine Clinical Medicine), 234 Gucui Road, Hangzhou, 310012, China;[5]State Key Laboratory of Natural Medicines, China Pharmaceutical University, Nanjing 210009, China; [6]Shanghai XuRan Biotechnology Co., Ltd., 1088 Zhongchun Road, Shanghai 201109, China; [7]Affiliated Hospital of Nanjing University of Chinese Medicine, 155 Hanzhong Road, Nanjing 210029, China.

[#]These authors contributed equally to this work.

The documents include:
Figs. S1-S26
Supplementary Table 1-3
Supplementary video 1-3

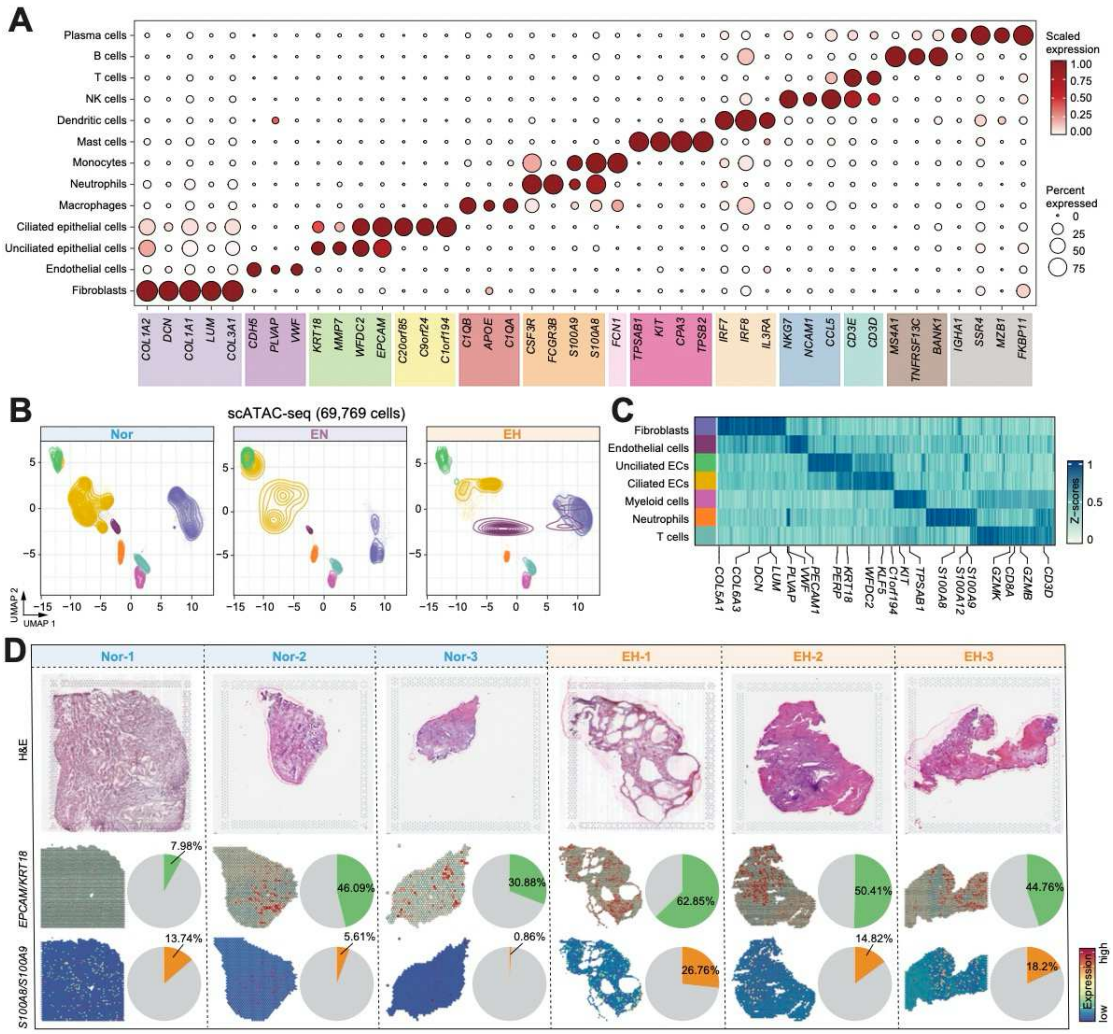


Fig. S1. The marker gene for each cluster based the date of scRNA-seq, scATAC-seq, CITE-seq. Related to Figure 1.

(A) Dot plot showing representative marker genes across cell types. Dot size is proportional to the fraction of cells expressing specific genes. Color intensity corresponds to the relative expression of specific genes. **(B)** UMAP plots showing the integrated cell map from scATAC-seq data, colored by major cell types by groups. **(C)** Heatmap showing gene-activity scores of marker genes in the indicated cell types. **(D)** Hematoxylin-Eosin (H&E) images (top) of spatial transcriptomics (ST) slides from normal or EH samples, with the average expression level of selected epithelial cell markers (*EPCAM* and *KRT18*) (middle) and neutrophil markers (*S100A8* and *S100A9*) (bottom) overlaying the ST slides. Pie charts below show the percentage of spots that express those genes. The data analysis of scRNA-seq, scATAC-seq, and ST-seq was based on Figure 1.

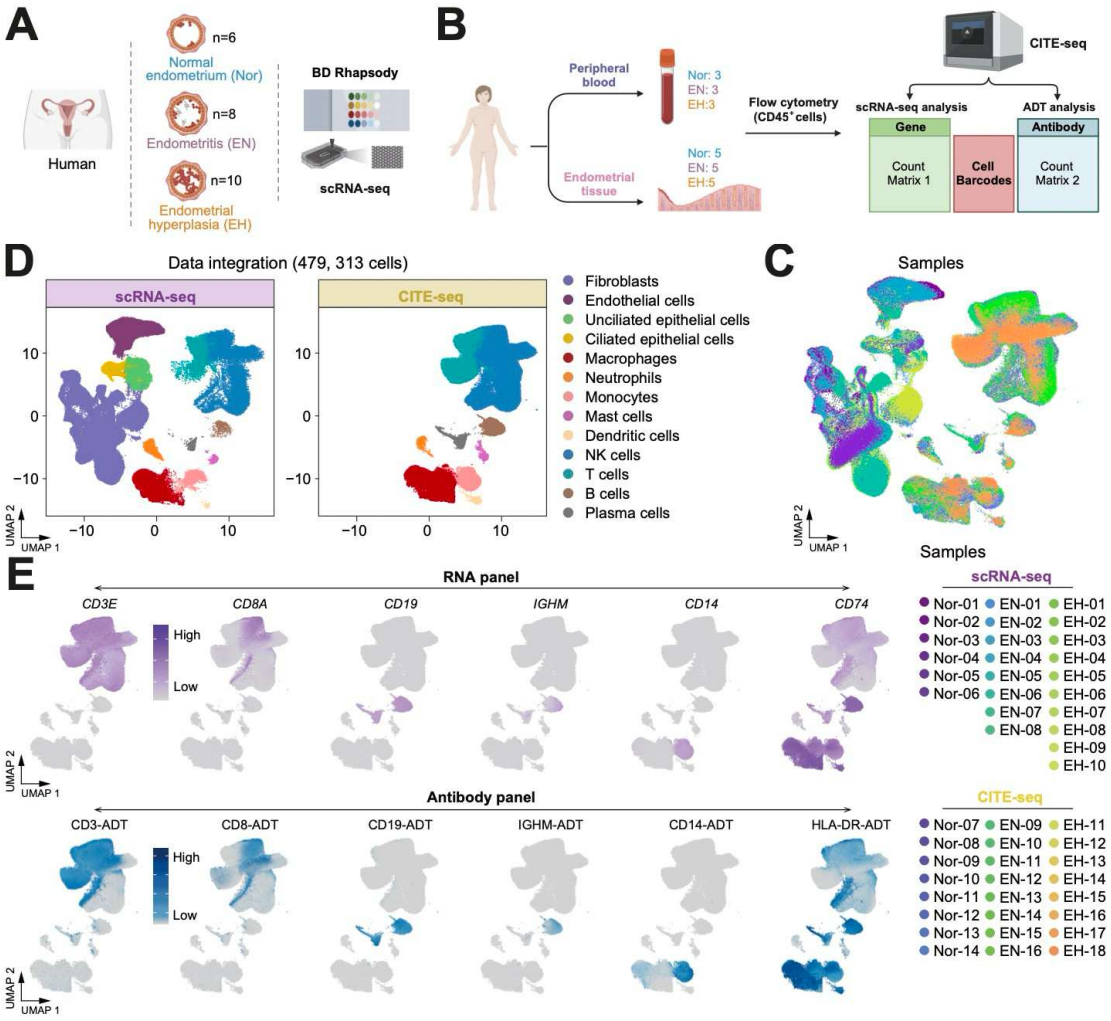


Fig. S2. CITE-seq assisted cell type identification. Related to Figure 1.

(A) Workflow for sample collection and scRNA-seq base on BD Rhapsody from human endometrial tissue. **(B)** Workflow for sample collection and CITE-seq from human endometrial tissue and peripheral blood. **(C)** UMAP plot showing the distribution of samples. **(D)** UMAP plot showing the distribution of cell types by datasets. **(E)** Normalized expression of selected mRNAs and surface proteins highlighted on the UMAP space from **(D)**. Top: expression of mRNAs encoding surface markers widely used to identify main cell types. Bottom: expression of the corresponding surface proteins.

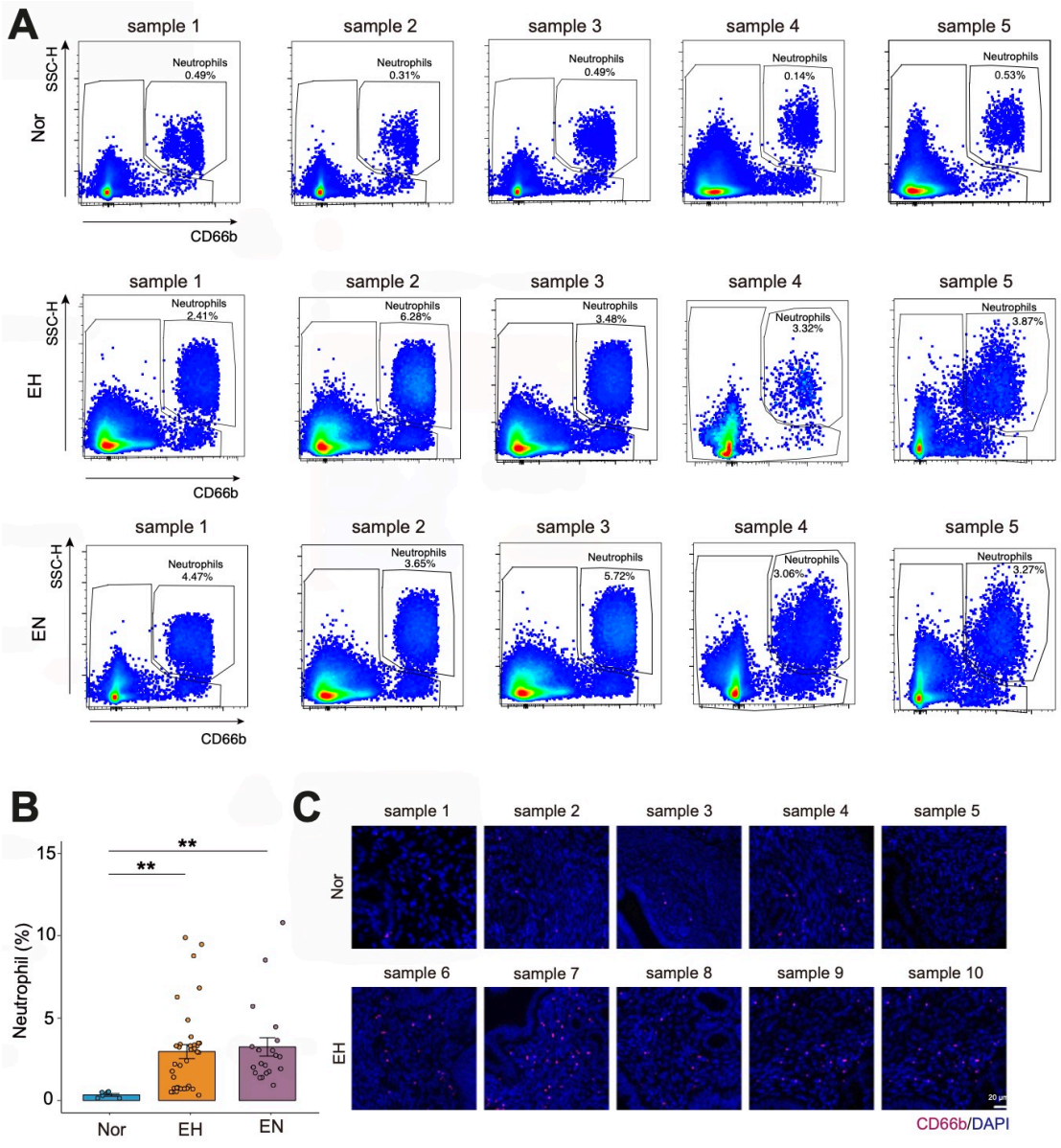


Fig. S3. The proportion of neutrophils increases in EH. Related to Figure 1.

(A&B) Frequencies of neutrophils in the white blood cell (WBC) of human endometrial tissues, $^{**}p<0.01$. **(C)** Human endometrial tissues were stained with CD66 (Red) and DAPI (blue). Scale bar: 20 μm.

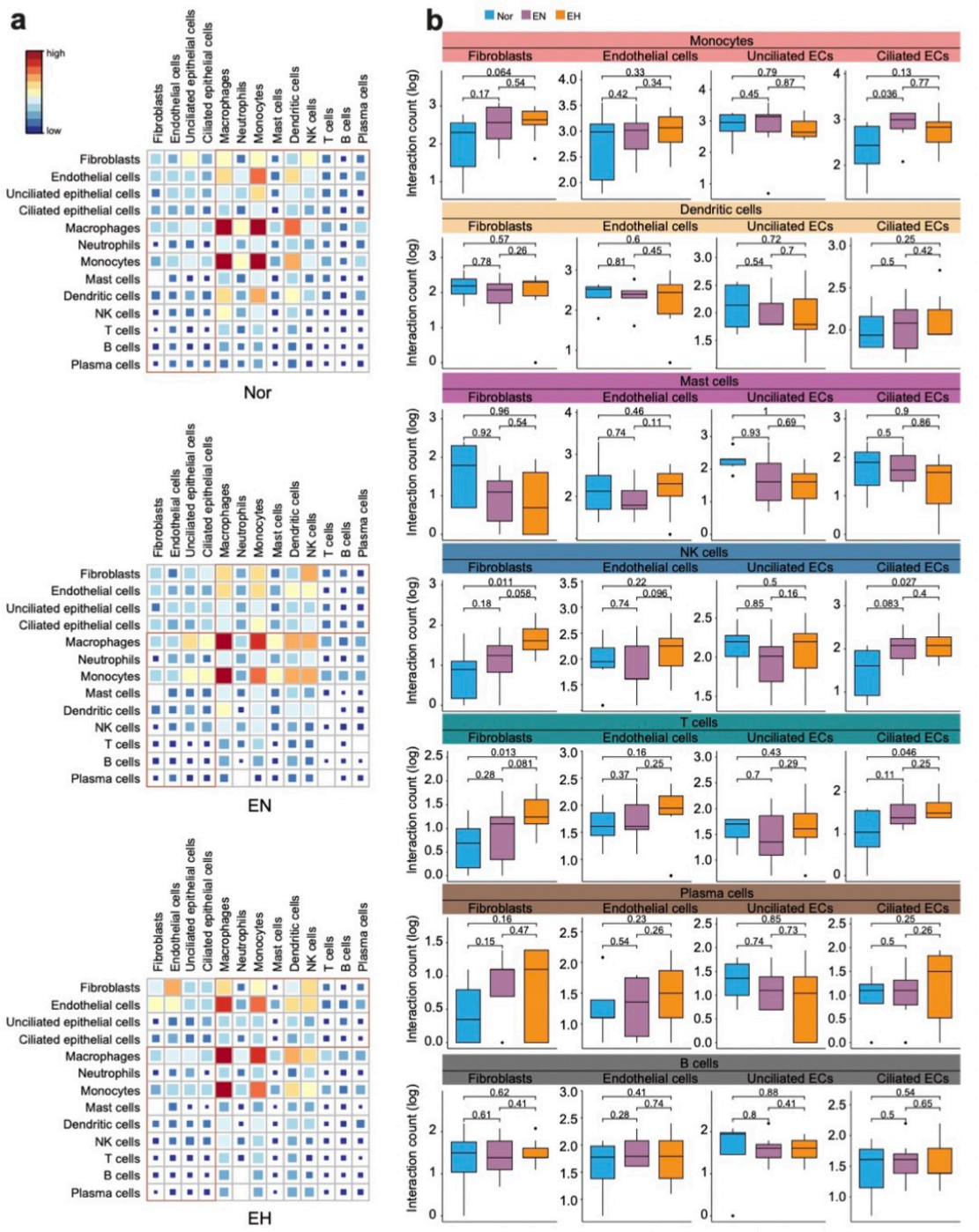


Fig. S4. Dynamics of cell-cell interaction networks in each group. Related to Figure 1.

(a) A Heatmap illustrating the cell interaction patterns in Nor, EN, and EH samples. **(b)** Boxplot indicating cell interaction counts between immune cells and non-immune cells respectively. The *p*-value is calculated using the Wilcoxon rank sum test.

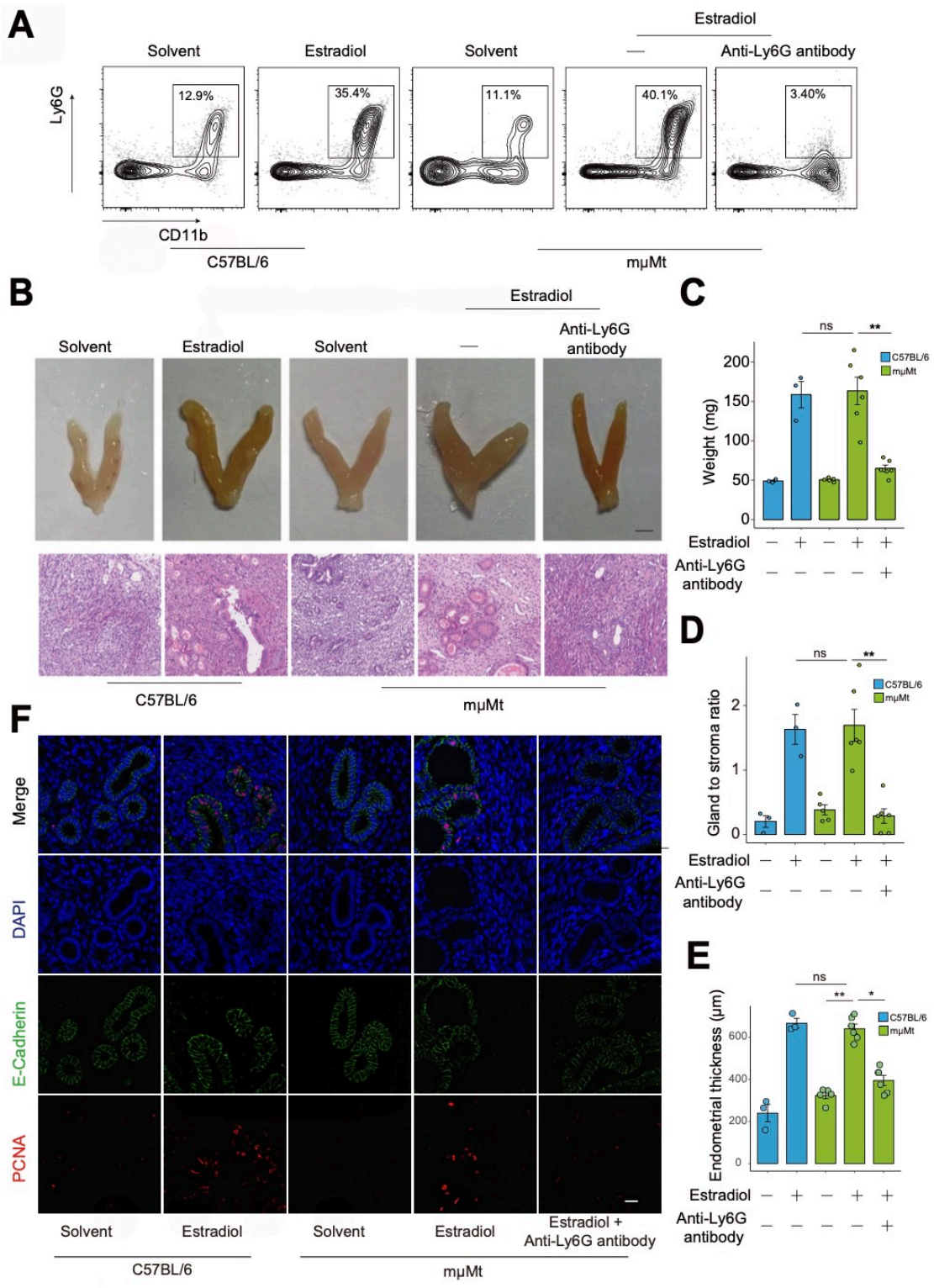


Fig. S5. Neutrophils but not B cells are indispensable for the development of EH induced by estradiol in mice. Related to Figure 1.

(A) Female C57BL/6 mice and B6.129S2-Ighmtm1Cgn/J (muMt) mice were treated with estradiol (50 μg/kg, s.c.) for 21 days. Anti-Ly6G antibody (12.5 mg/kg) were intraperitoneally administered every 3 days. Representative plots of neutrophils in uterus tissues. **(B)** Representative macrophotographs of uterus in each group (scale bar, 0.5 cm), (n=3-6). Representative images of H&E staining (scale bar, 160 μm). **(C)** Uterus weight of each group (n=3-6); $^{**}p<0.01$. **(D)** Statistics of the area ratio of gland to stroma according to H&E staining images (n=3-6); $^{**}p<0.01$.

(E) Statistics of endometrial thickness according to H&E staining images (n = 3–6); $^{**}p < 0.01$. **(F)** Mice endometrial tissues were stained with PCNA (Red), E-cadherin (green) and DAPI (blue), (n = 3–6)Scale bar: 20 μm.

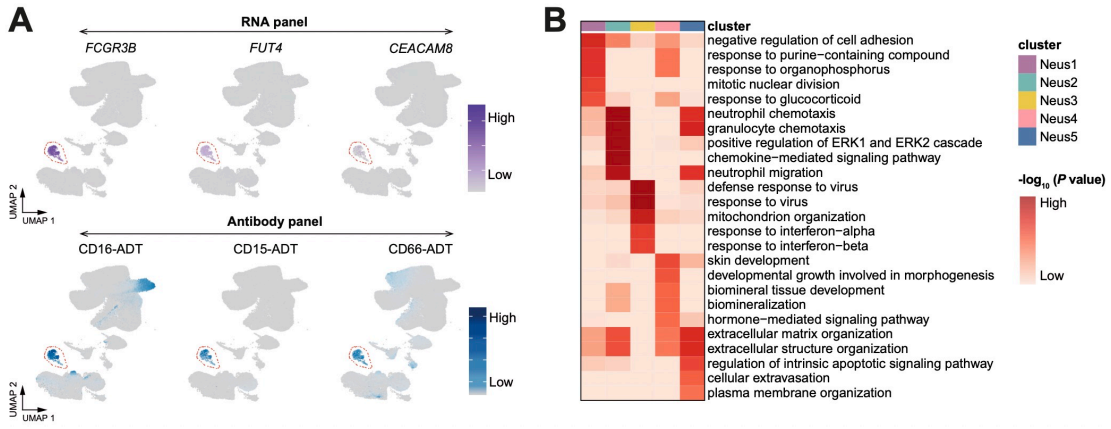


Fig. S6. Transcriptional and protein signatures of human neutrophils. Related to Figure 2.

(A) Feature plots showing the gene and protein expression of canonical markers of neutrophils (CD66b, CD16, CD15). **(B)** Heatmap showing enrichment of representative GO terms in neutrophil subtypes.

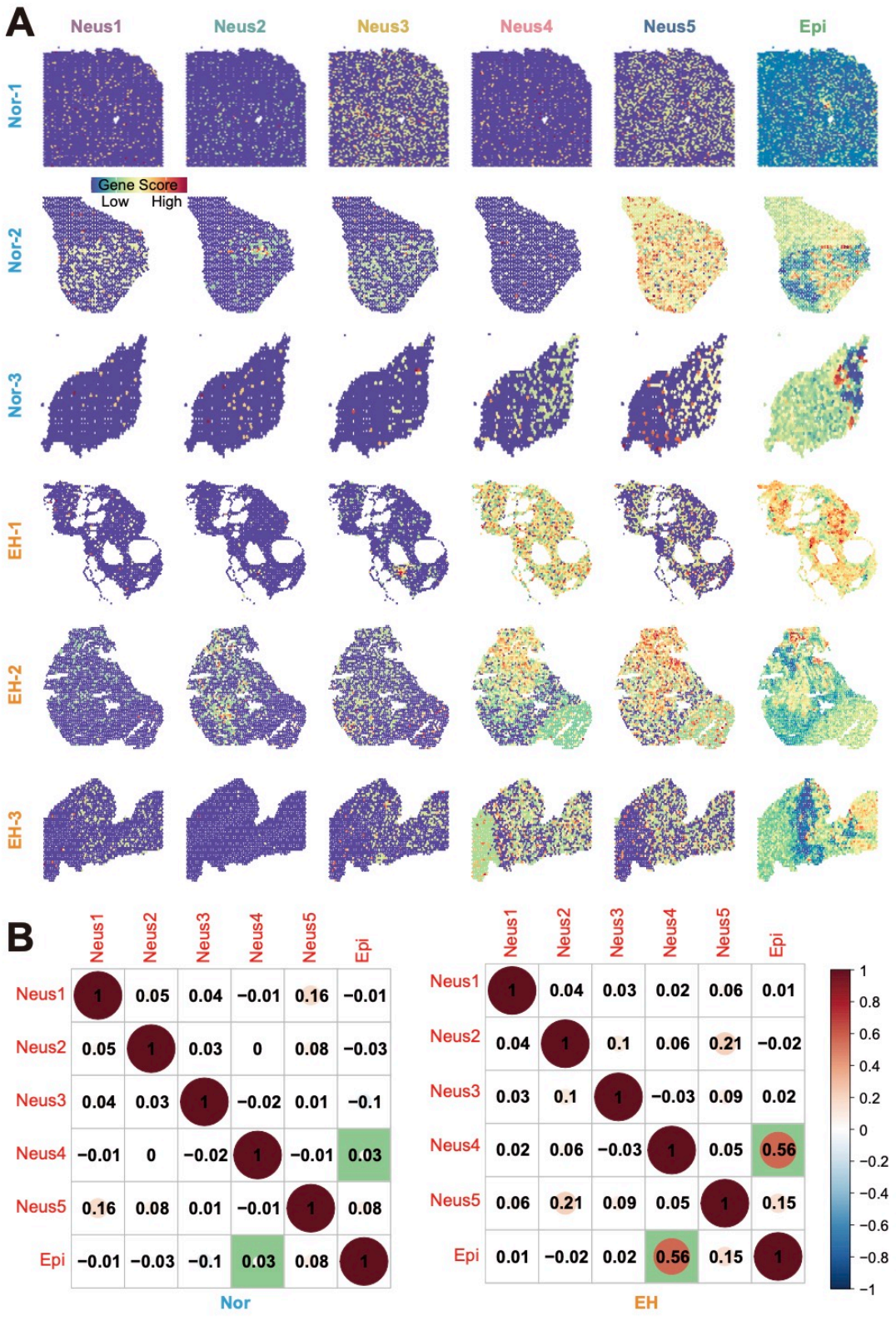


Fig. S7. Spatial transcriptomics analysis of neutrophil subsets. Related to Figure 2.

(A) Gene set scores of the top 10 genes of neutrophil subsets and epithelial cells on spatial transcriptomics (ST) spots from human endometrial tissue. **(B)** Corrplot showing the correlation between neutrophil subsets and epithelial cells according to (A).

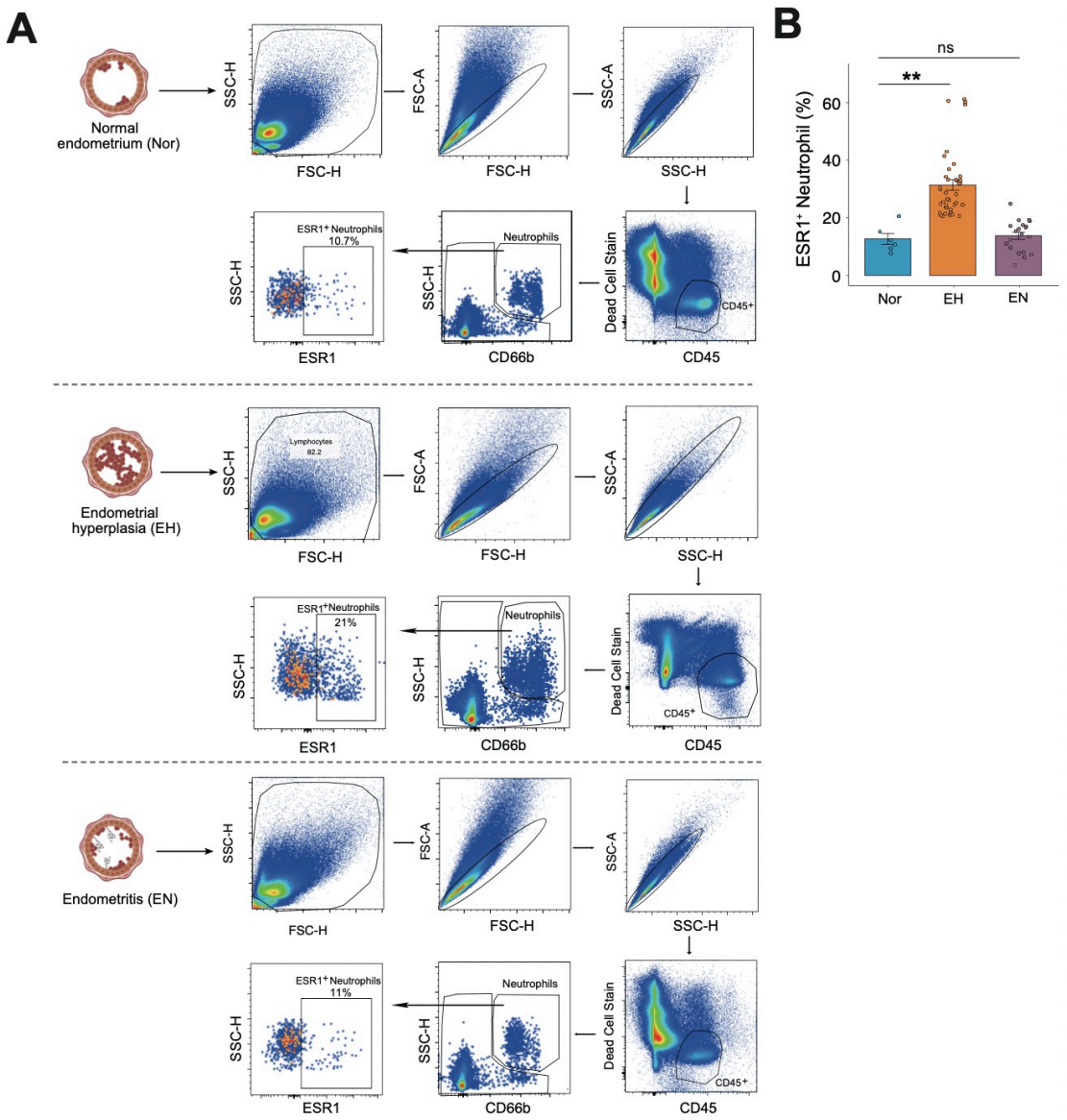


Fig. S8. The proportion of *ESR1*$^+$ Neutrophil increases in endometrial hyperplasia. Related to Figure 2.

(A&B) Representative plots and frequencies of *ESR1*$^+$ neutrophils in the total neutrophils from clinical endometrial tissue, $^{**}p<0.01$.

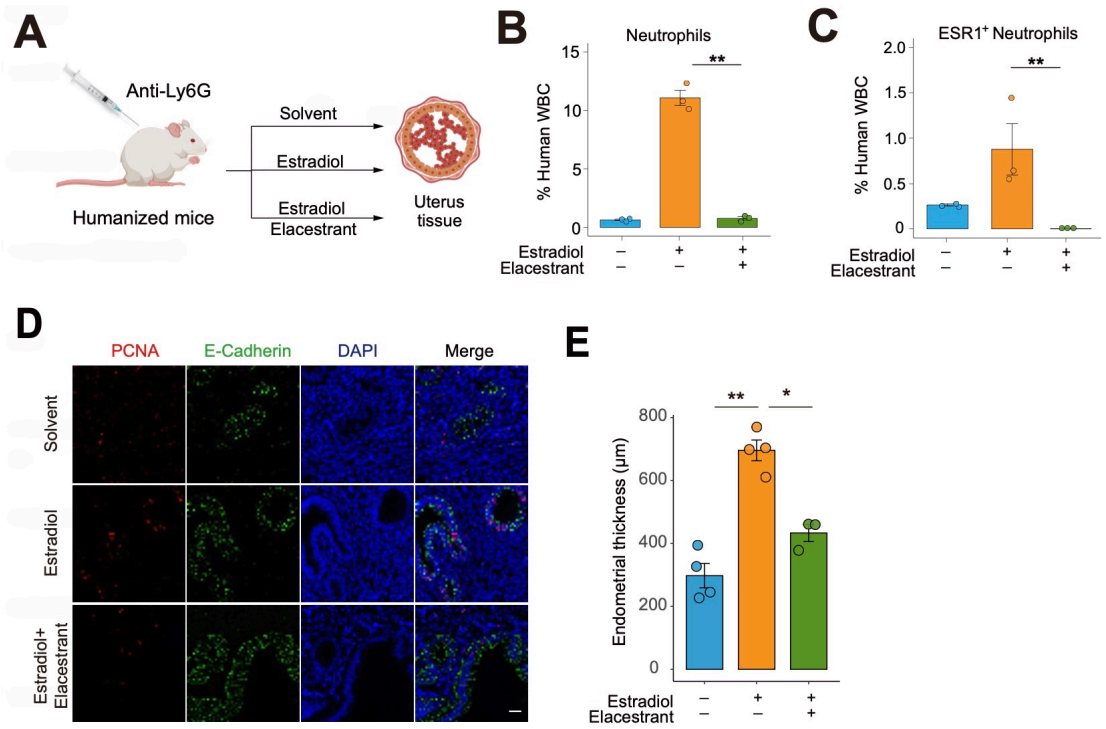


Fig. S9. Validation of *ESR1*$^{+}$ neutrophil clearance efficiency. Related to Figure 2.

(A-C) NCG humanized (human immune system, HIS) mice were treated with estradiol (50 μg/kg, s.c.) for 21 days. Anti-mouse Ly6G antibody (12.5 mg/kg) were administered on two days interval, and Elacestrant was administered intragastrically daily at a dosage of 30 mg/kg. The frequencies of neutrophils or *ESR1*$^{+}$ neutrophils in the uterine tissue, $^{**}p<0.01$. **(D)** Mice endometrial tissues were stained with PCNA (Red), E-cadherin (green) and DAPI (blue), (n = 3–6), Scale bar: 20 μm. **(E)** Statistics of endometrial thickness according to H&E staining images (n = 3–6); $^{**}p < 0.01$.

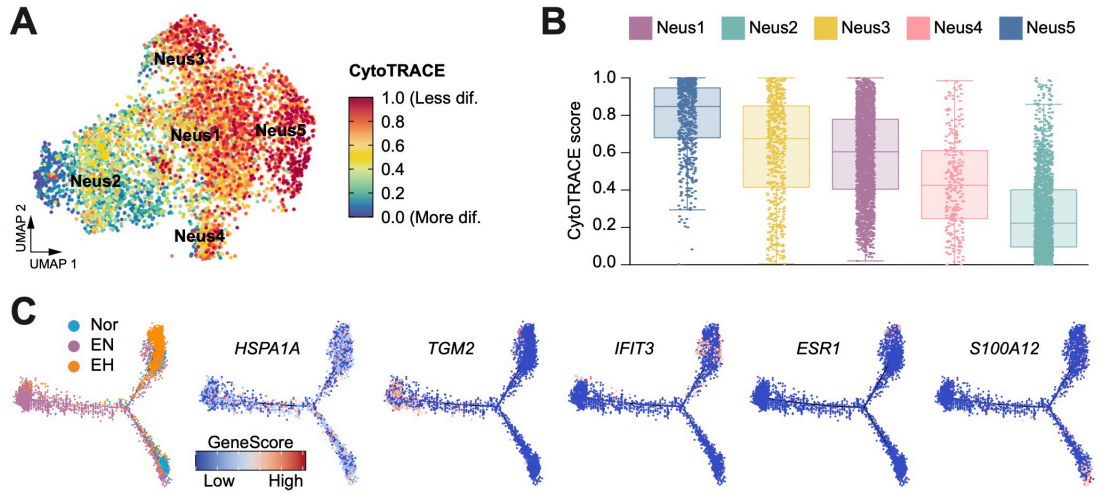


Fig. S10. Transcriptional and protein signatures of human neutrophils. Related to Figure 3.

(A) UMAP of neutrophils by differentiation state inferred by CytoTRACE. **(B)** Boxplot showing the CytoTRACE scores of neutrophil subtypes. **(C)** Pseudotime trajectory of neutrophil subtypes as colored by groups and expression dynamics of marker genes.

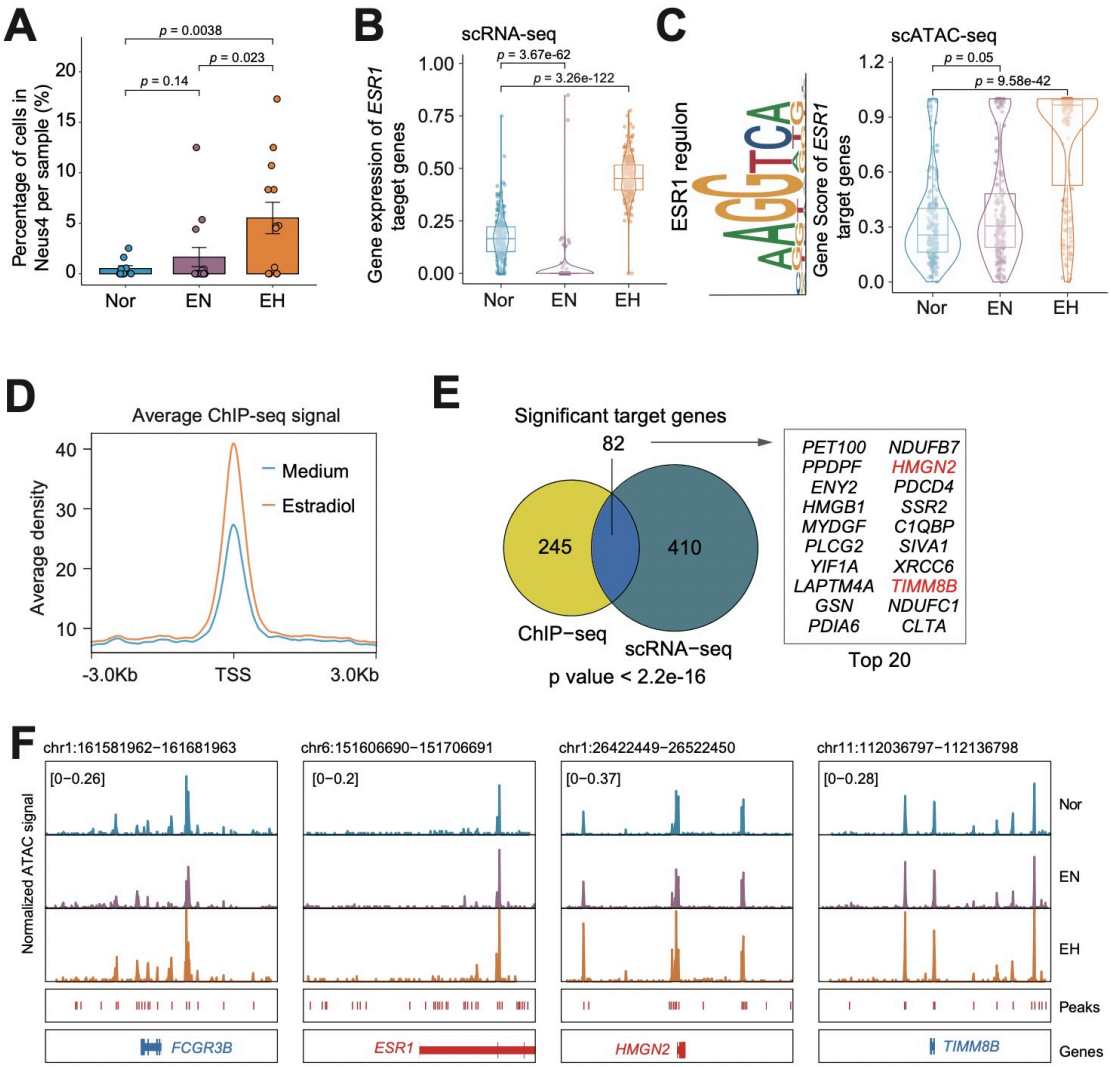


Fig. S11. Estrogen induced ERα binding to *HMGN2* and *TIMM8B*. Related to Figure 3.

(A) Box plot illustrating the percentage of Neus4 in different samples according to human scRNA-seq. The p-value is calculated using the Wilcoxon rank sum test. **(B)** Boxplot showing the scaled mean expression of *ESR1* target genes (n=251) in cells from different sample groups according to human scRNA-seq. **(C)** Seq logo showing TF binding motif of *ESR1* (left). Boxplot showing the scaled chromatin accessibility of *ESR1* target genes (n=251) in cells from different sample groups (right) according to human scATAC-seq. **(D)** Neutrophils isolated from the peripheral blood of healthy donors were treated with with 50 nM or medium at 37°C for 6 h. The ChIP-seq experiment was performed. Density plot showing the binding signal of TFs in estradiol group is enhanced in ChIP-seq predicted target genes compared with medium group. **(E)** Venn diagrams showing the overlapping genes between target genes predicted by scRNA-seq compared with genes predicted by increased peaks in estradiol group. **(F)** Genome browser tracks showing normalized ATAC-seq signals in Normal, EN, and EH groups at representative loci (*FCGR3B, ESR1, HMGN2, and TIMM8B*) with annotated peaks and gene models.

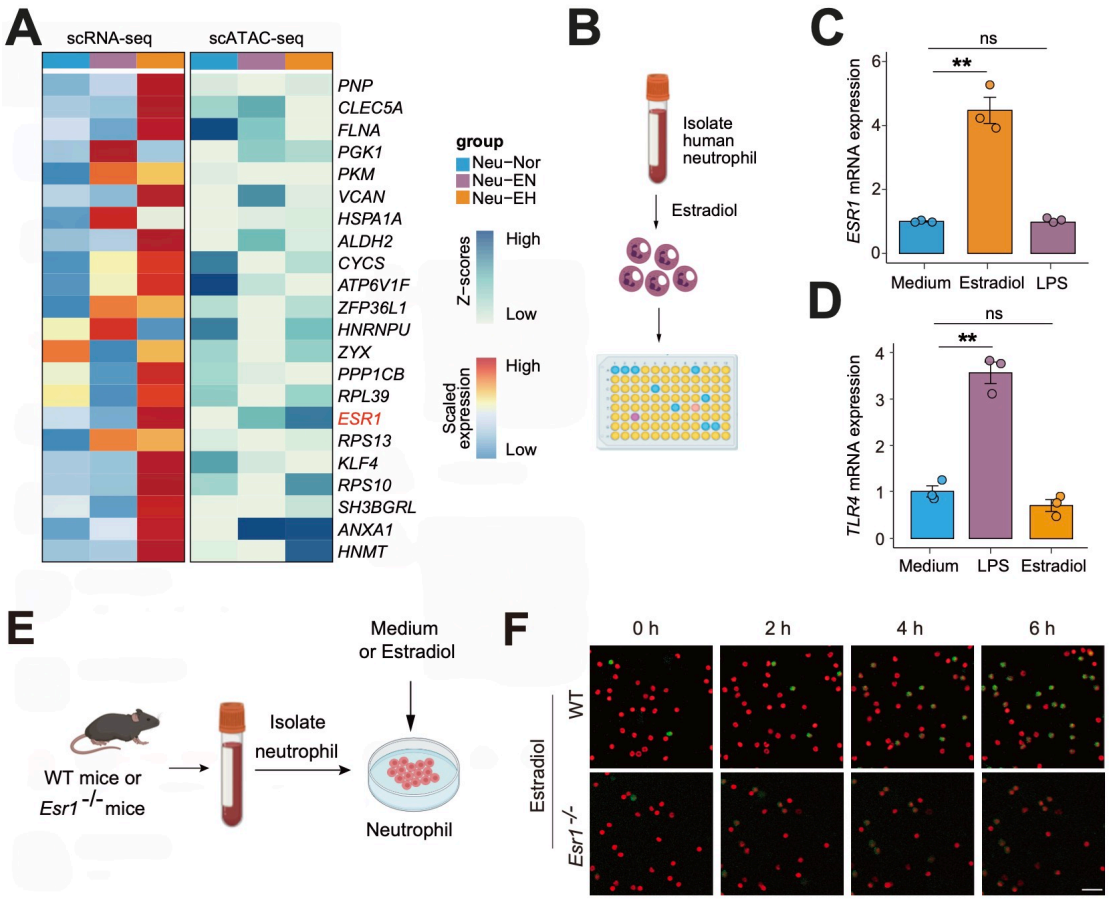


Fig. S12. Estrogen significantly induces *ESR1* expression in neutrophils. Related to Figure 3.

(A) The Heatmap showing gene expression and chromatin accessibility of *ESR1* and its top target genes between the three groups. **(B)** Experimental workflow for getting neutrophils. **(C&D)** Purified neutrophils from the peripheral blood of healthy donors incubated with 50 nM estradiol or 10 ng/mL LPS at 37℃ for 2 h. The mRNA expression levels of representative *TLR4* and *ESR1* in neutrophils (n=3). ***P*<0.01; ns, no significance. **(E)** Experimental workflow for getting neutrophils from peripheral blood and estradiol treatment. (**F**) Primary mouse neutrophils were stained with Draq5 (blue) and Sytox Green (green), stimulated with 50 nM estradiol, and monitored for 6 h. NETosis was identified by the emergence of green fluorescence. Scale bar: 20 μm.

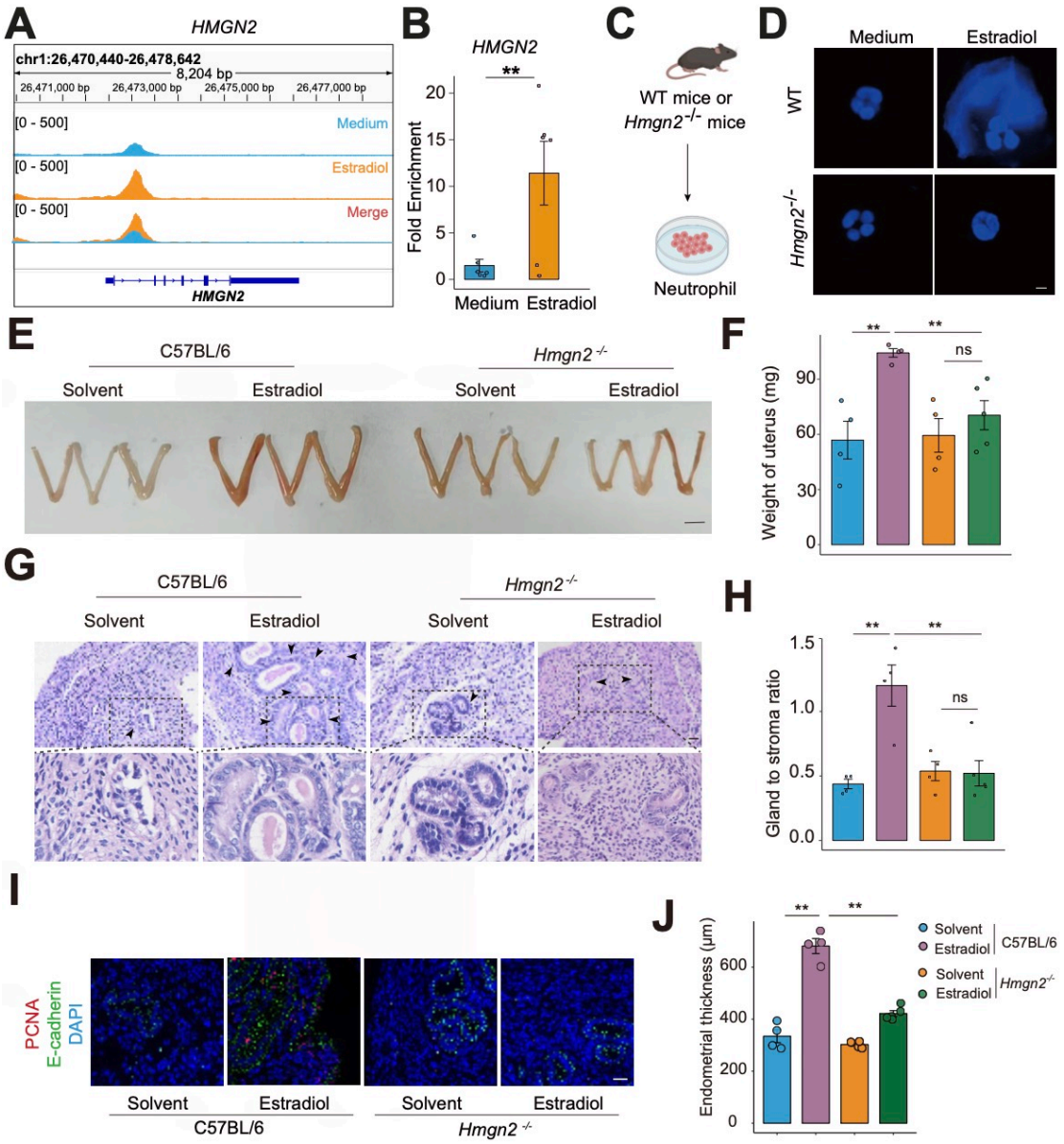


Fig. S13. *Hmgn2* KO mice were not sensitive to estrogen-induced EH. Related to Figure 3.

(A) Neutrophils isolated from the peripheral blood of healthy donors were treated with with 50 nM or medium at 37℃ for 6 h. The ChIP-seq experiment was performed. IGV screenshots showing ERα binding at the HMGN2 gene locus in two groups. **(B)** Neutrophils isolated from the peripheral blood of healthy donors were treated with with 50 nM or medium at 37℃ for 2h. ChIP-qPCR revealed the binding of ESR1 to *HMGN2*, ***P*<0.01. **(C)** Experimental workflow for getting neutrophils from peripheral blood of WT mice or Hmgn2 KO mice and estradiol treatment. **(D)** Neutrophils were incubated with 50 nM or medium at 37℃ for 2 h. Neutrophils were stained with DAPI (blue). Scale bar: 5 μm. **(E)** *Hmgn2* KO mice were given a daily subcutaneous injection of 50 μg/kg estrogen for 21 days. Representative macrophotographs of uterus in each group (scale bar, 0.5 cm). **(F)** Uterus weight of each group (n=4 or 5), ***P*<0.01. **(G)** Representative images of H&E staining (n=4 or 5, scale bar, 50 μm). **(H)** Statistics of the area ratio of gland to stroma according to H&E staining images (n=4 or 5), ***P*<0.01. **(I)** Mice endometrial tissues were stained with PCNA (Red), E-cadherin (green) and DAPI (blue), (n=4 or 5), Scale bar: 20 μm. **(J)** Statistics of endometrial thickness according to H&E staining images (n=4 or 5); ***p* < 0.01.

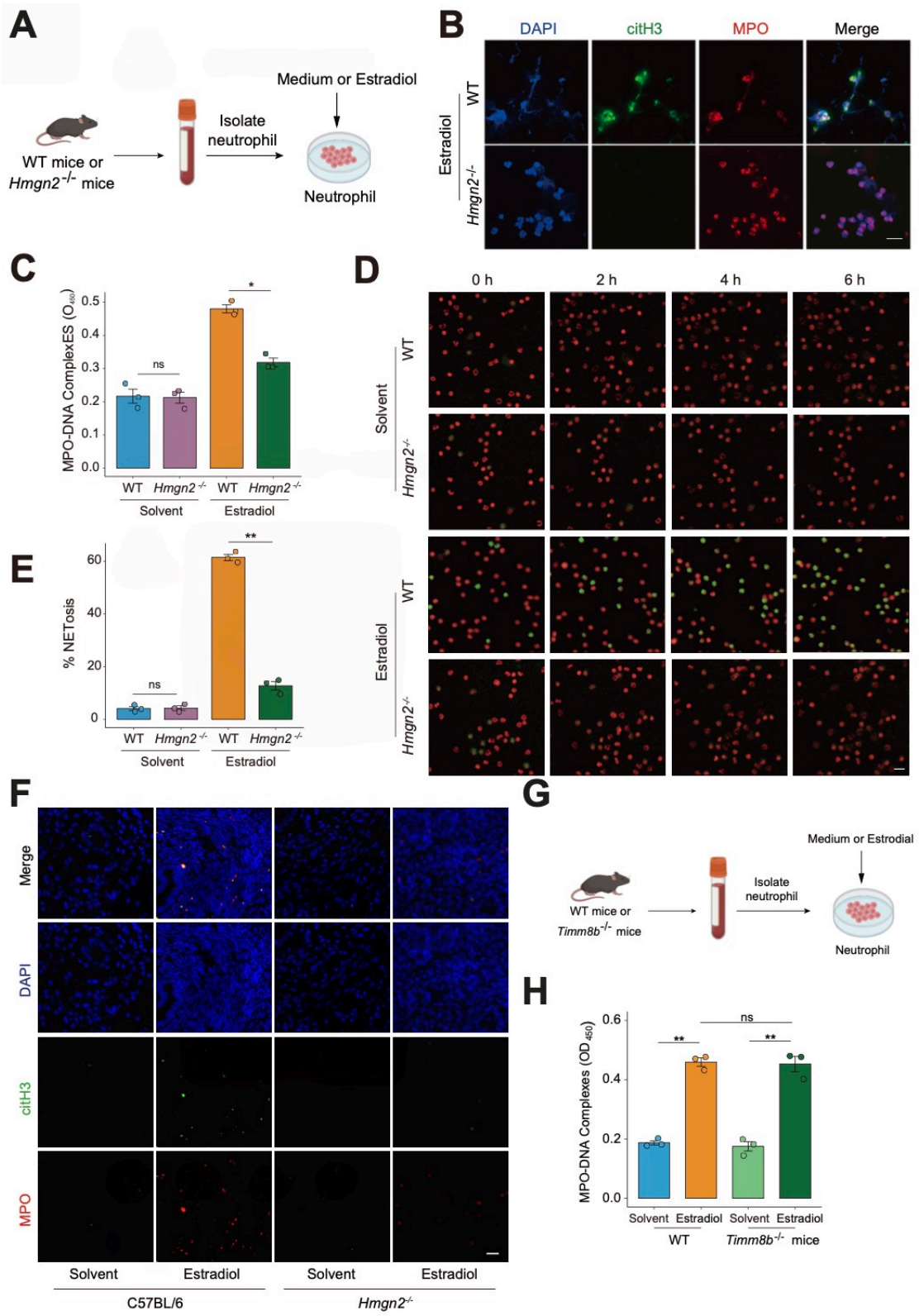


Fig. S14. Neutrophils derived from *Hmgn2* but not *Timm8b* knockout mice almost lost the ability to form a network structure triggered by estrogen. Related to Figure 3.

(A) Experimental workflow for getting neutrophils from mouse uterus and peripheral blood under estradiol treatment;

(B) Neutrophils were incubated with 50 nM estradiol or medium at 37℃ for 2 h. Neutrophils were stained with citH3 (green), MPO (red) and DAPI (blue); Scale bar: 20 μm. **(C)** Neutrophils were incubated with 50 nM estradiol or medium at 37℃ for 2 h. OD_{450} value reflects the level of MPO-DNA Complexes, **P*<0.05. **(D)** Primary mouse neutrophils were stained with Draq5 (blue) and Sytox Green (green), stimulated with 50 nM estradiol, and monitored for 6 h. NETosis was identified by the emergence of green fluorescence. Scale bar: 20 μm. (**E**) NETosis rate in the total neutrophils. ns, no significance, ***P*<0.01. **(F)** Mice endometrial tissues were stained with MPO (Red), E-citH3 (green) and DAPI (blue), (n=3), Scale bar: 20 μm. **(G)** Experimental workflow for getting neutrophils from mouse uterus and peripheral blood under estradiol treatment; **(H)** Neutrophils were incubated with 50 nM estradiol or medium at 37℃ for 2 h. OD_{450} value reflects the level of MPO-DNA Complexes, ns, no significance, ***P*<0.01.

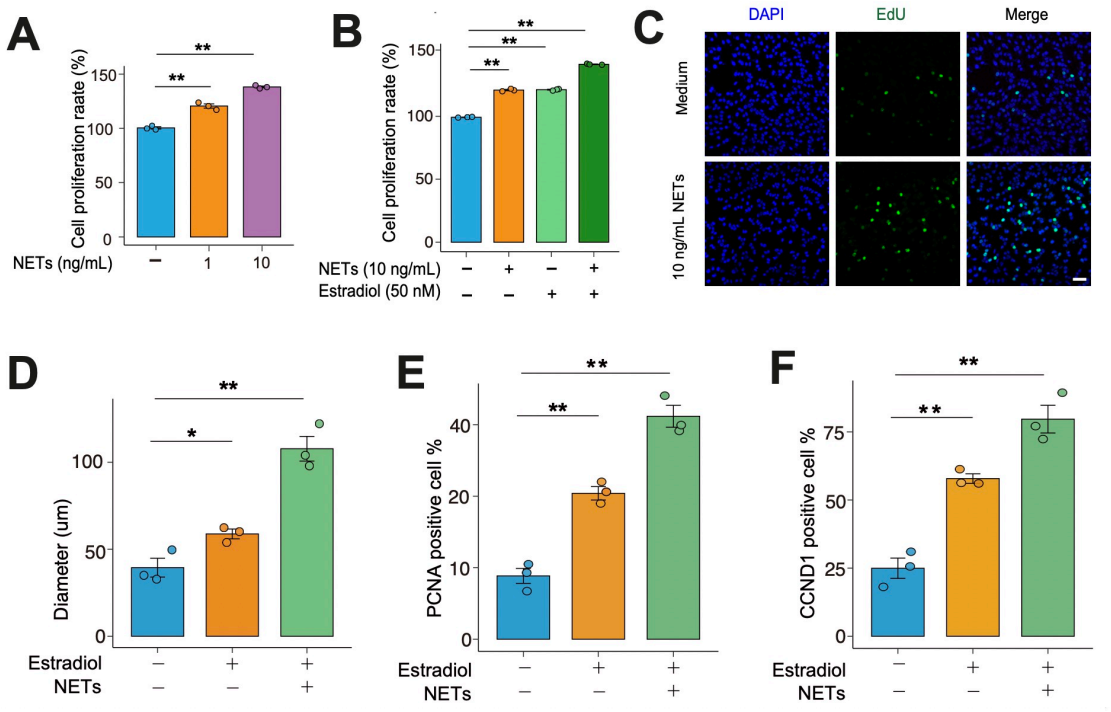


Fig. S15. NETs directly promote epithelial cell and endometrial organoid proliferation. Related to Figure 4.

(A-C) Human endometrial epithelial cells were treated with indicated concentration of NETs or estradiol for 24 h. Then the cell proliferation levels were measured by MTT (a-b) or EdU staining (c). ***P*<0.01. **(D)** Statistics of three largest organoids from Day 5 in Figure 4F, **P*<0.05, ***P*<0.01. **(E&F)** Statistics of PCNA or CCND1 positive cell based on Figure 4F, ***P*<0.01.

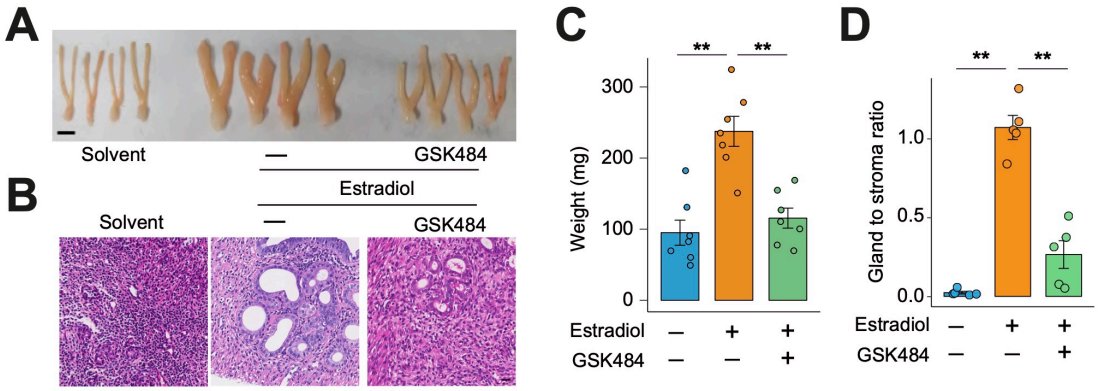


Fig. S16. GSK484 improves estrogen-induced EH in mice. Related to Figure 4.

(A) Female C57BL/6 mice were treated with estradiol (50 μg/kg, s.c.) with or without GSK484 (4 mg/kg, i.p.) for 21 days. Representative macrophotographs of uterus in each group (n=4, scale bar, 0.5 cm). **(B)** Representative images of H&E staining (n=5, scale bar, 80 μm). **(C)** Uterus weight of each group (n=7), ***P*<0.01. **(D)** Statistics of the area ratio of gland to stroma according to H&E staining images (n=5), ***P*<0.01.

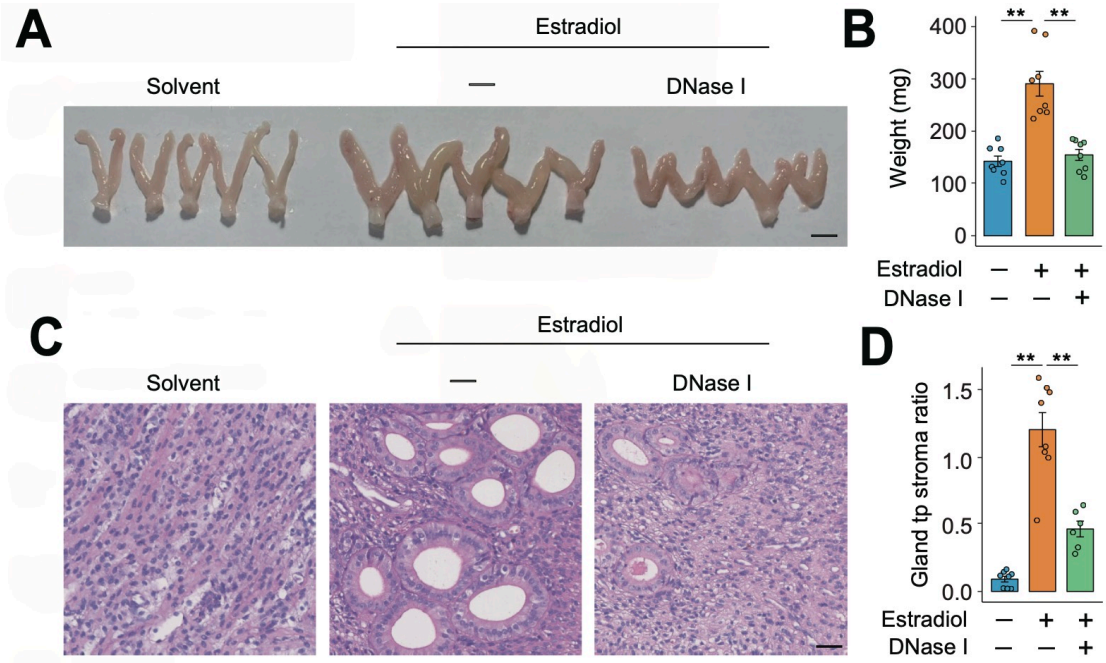


Fig. S17. DNase I ameliorated estrogen-induced EH in mice. Related to Figure 4.

(A) C57BL/6 female mice were treated with 50 μg DNase I intraperitoneally three times per week during 50 μg/kg estrogen treatment. Representative macrophotographs of uterus in each group (n=5, scale bar, 0.5 cm). **(B)** Uterus weight of each group (n=8), ***P*<0.01. **(C)** Representative images of H&E staining (n=5, scale bar, 80 μm). **(D)** Statistics of the area ratio of gland to stroma according to H&E staining images (n=6-8), ***P*<0.01.

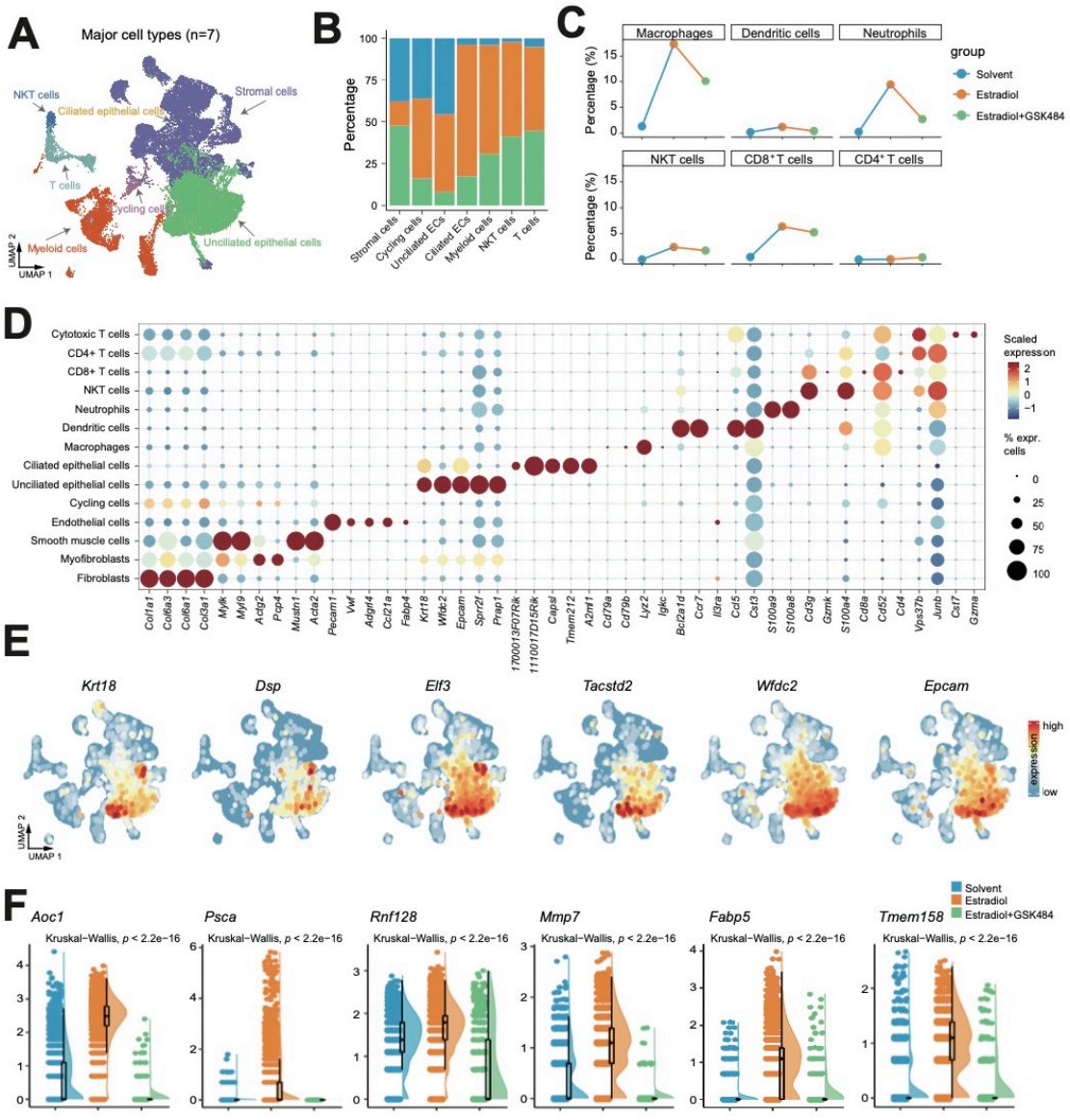


Fig. S18. Mouse cell map. Related to Figure 5.

(A) UMAP plot showing the integrated mouse cell map as colored by major cell types based on scRNA-seq of Figure 5A. **(B)** Percentage of cells from different sample groups for each cell types, colored by groups. **(C)** Dumbbell plots illustrating the proportions of distinct immune cell types across Normal, EH, and GSK groups. **(D)** Dot plot depicting top cell-type-specific gene markers. **(E)** Expression of selected genes on the UMAP plots. **(F)** Raincloud plots showing expression of selected proliferation-associated genes among different groups.

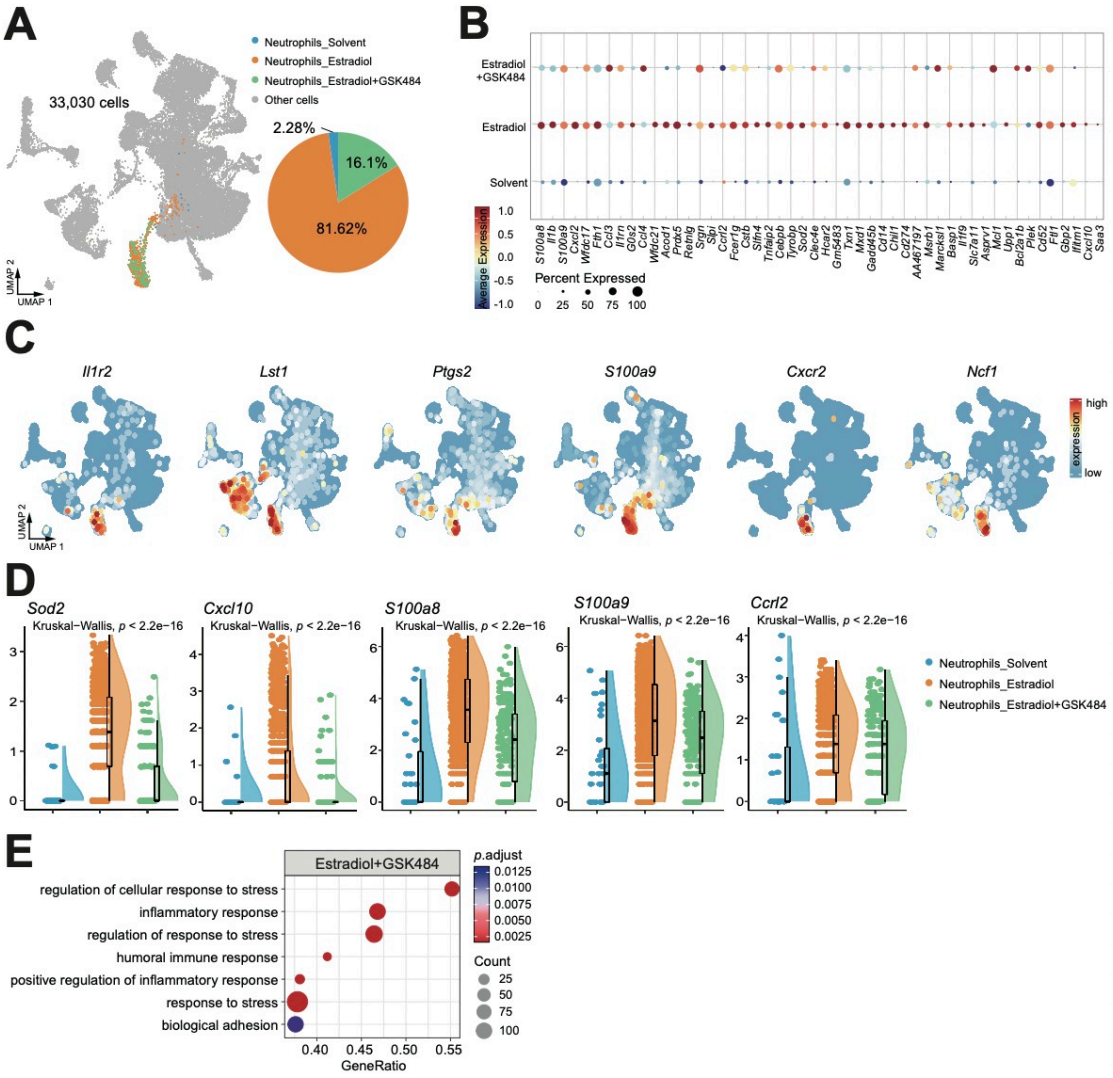


Fig. S19. Transcriptional signatures of mouse neutrophils. Related to Figure 5.

(A) UMAP plot highlighting the distribution of neutrophils from different sample groups based on scRNA-seq of Figure 5A. **(B)** Dot plot depicting top group-specific markers in neutrophils. **(C)** Expression of selected genes on the UMAP plots. **(D)** Raincloud plots showing expression patterns of selected neutrophil-related genes across different groups. **(E)** Dot plot showing enriched GO biological processes of DEGs in GSK484 + E2 vs E2.

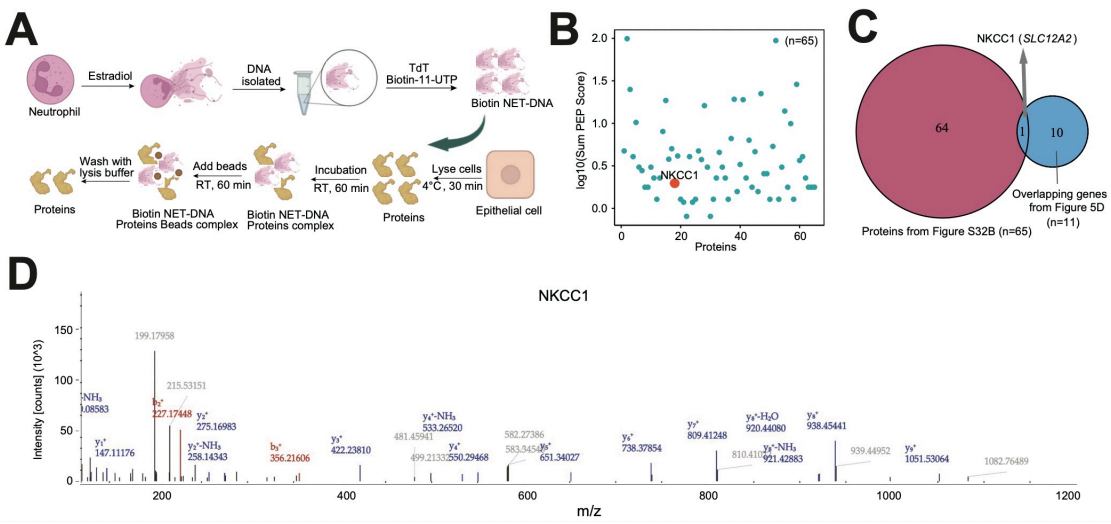


Fig. S20. NKCC1 binds to NET-DNA. Related to Figure 5.

(A) Schematic of NET-DNA pull-down assays. **(B)** Mass spectrometry analysis identified 65 membrane proteins pulled down by the biotinylated NET-DNA. **(C)** Venn diagrams showing the overlaps between 65 membrane proteins coding genes and 11 differential expressed genes. **(D)** Mass spectrometry analysis identified NKCC1 was pulled down by the biotinylated NET-DNA.

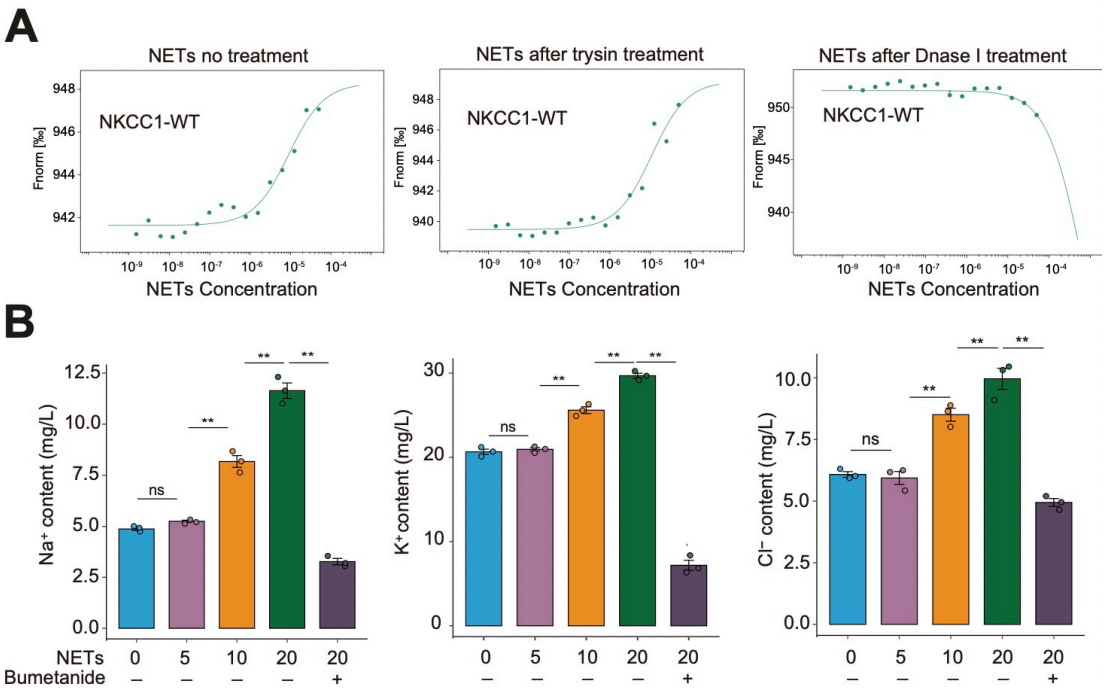


Fig. S21. NET-DNA could directly bind to NKCC1. Related to Figure 5.

(**A**) HEK293T cells were transfected with GFP-NKCC1 plasmids and were lysed after 48 hours. The binding of NETs to NKCC1 protein under different treatment conditions was demonstrated by MST. (**B**) Human endometrial epithelial cells were treated with NETs or bumetanide. Lysates were subjected to measure the content of Na^+, K^+, Cl^- ion, $^{**}P<0.01$.

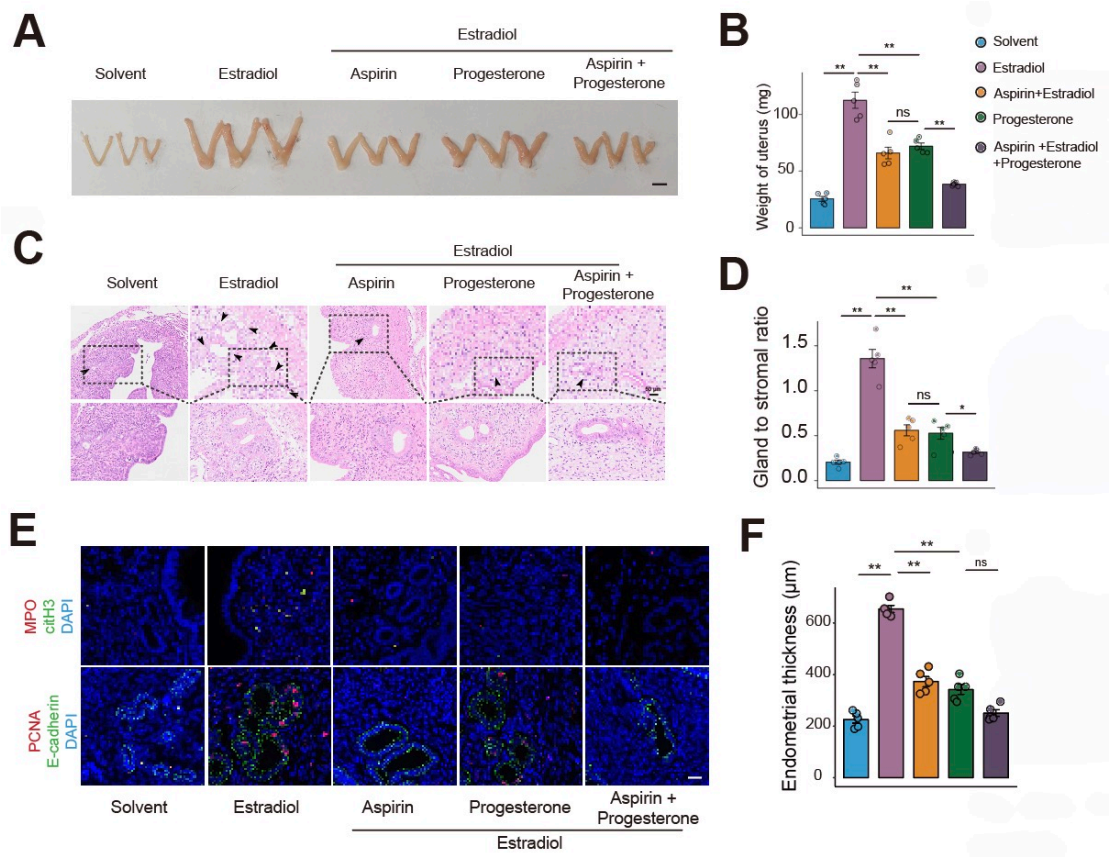


Fig. S22. Aspirin inhibit estrogen-induced NETs formation *in vivo*. Related to Figure 6.

(A) C57BL/6 female mice were administered 50 μg/kg estradiol to induce endometrial hyperplasia. To evaluate therapeutic interventions, mice received either aspirin (5 mg/kg, intraperitoneal injection) or progesterone (2 mg, subcutaneous injection), followed by estradiol administration. Representative macrophotographs of uterus in each group (n=5). Scale bar, 0.5 cm. **(B)** Uterus weight of each group (n=5), $^{**}P<0.01$. **(C)** Representative images of H&E staining (scale bar, 50 μm). **(D)** Statistics of the area ratio of gland to stroma according to H&E images (n=5), $^{**}P<0.01$, $^{*}P<0.05$. **(E)** Mice endometrial tissues were stained with PCNA or MPO (Red), citH3 or E-cadherin (green) and DAPI (blue), (n=3), Scale bar: 20 μm. **(F)** Statistics of endometrial thickness according to H&E staining images (n=4 or 5); $^{**}p < 0.01$.

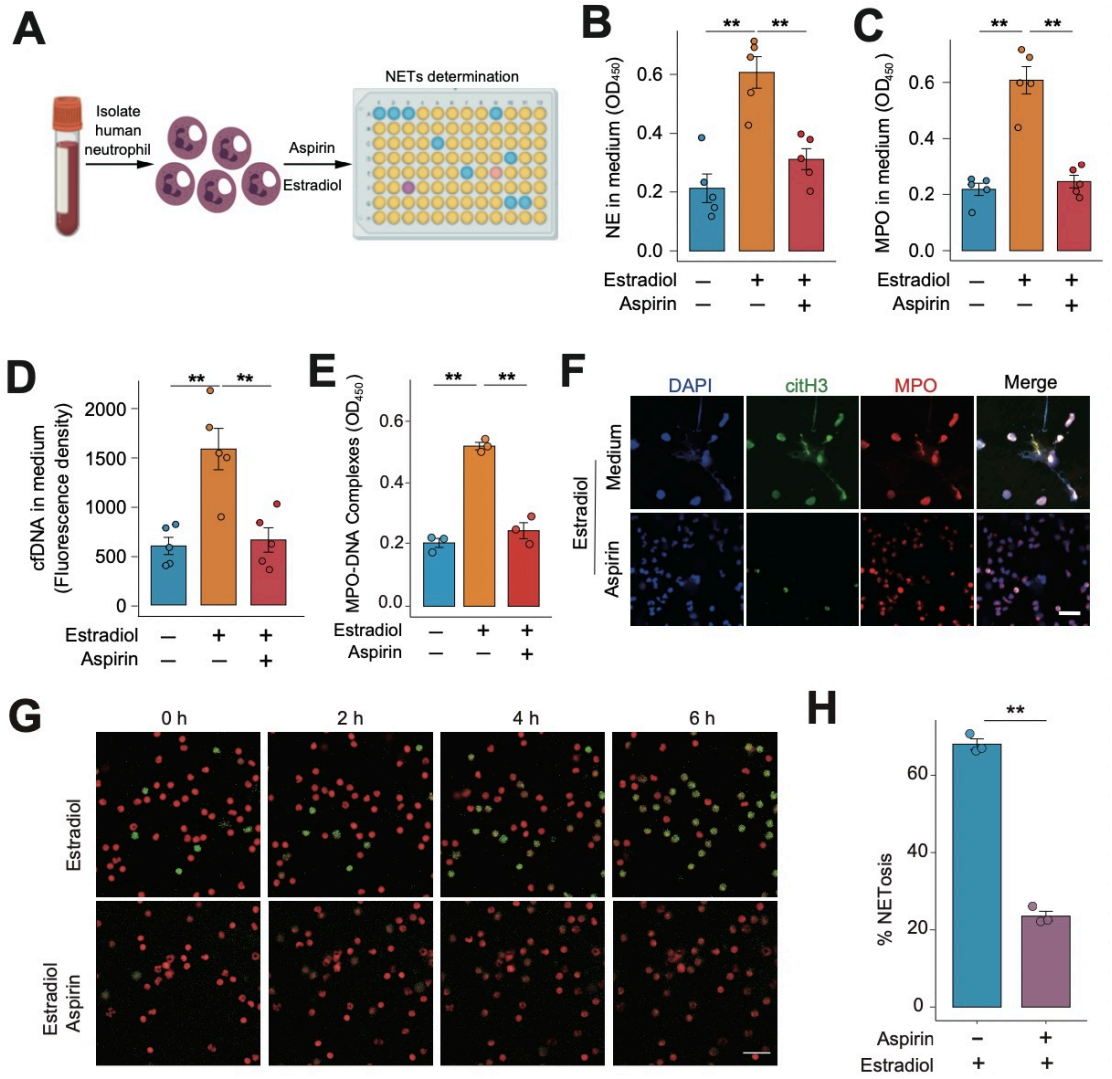


Fig. S23. Aspirin inhibit estrogen-induced NETs formation *in vitro*. Related to Figure 6.

(A) Experimental workflow for screening NETs inhibitor from FDA-approved drug library. **(B-E)** Purified human neutrophils were incubated with 50 nM estradiol or 5 μM aspirin at 37°C for 2 h. OD_{450} value or fluorescence density value reflects the levels of NE, MPO, MPO-DNA Complexes or cfDNA (n=3-5), $^{**}P<0.01$. **(F)** Purified human neutrophils were incubated with 50 nM estradiol or 5 μM aspirin at 37°C for 2 h. Immunofluorescence staining of the neutrophils with citH3 (Green), MPO (Red) and DAPI (Blue). Scale bar: 20 μm. (**G**) The neutrophils were stained with Draq5 (blue) and Sytox Green (green), stimulated with 50 nM estradiol or 5 μM aspirin, and monitored for 6 h. NETosis was identified by the emergence of green fluorescence. Scale bar: 20 μm. (**H**) NETosis rate in the total neutrophils. ns, no significance, $^{**}P<0.01$.

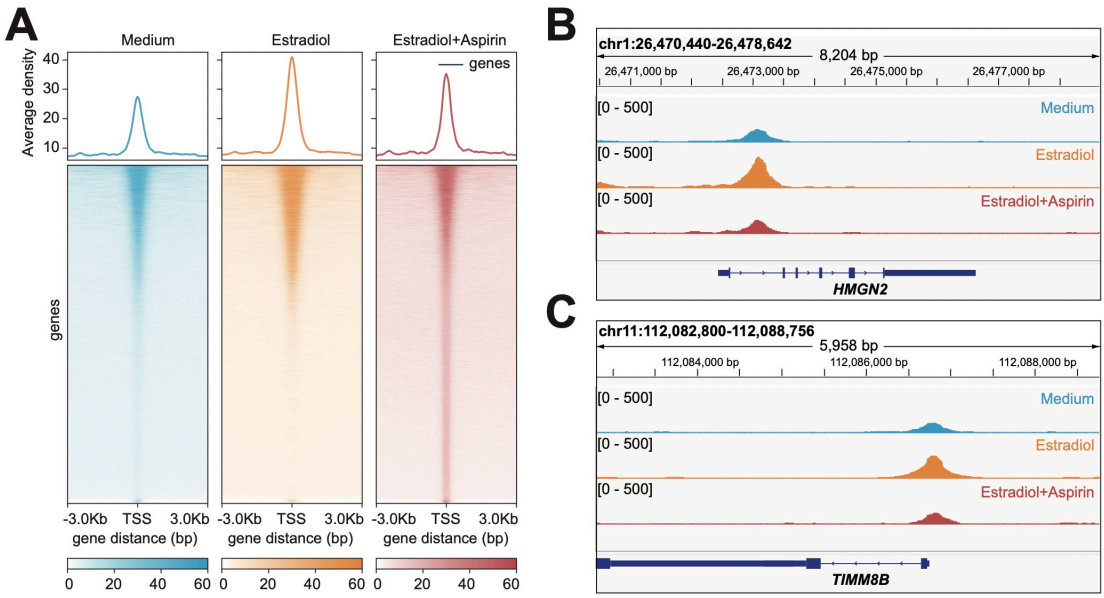


Fig. S24. Aspirin decreases *ESR1* binding signal in estradiol-induced neutrophils. Related to Figure 6.

(A) Genome-wide binding patterns of ERα near transcription start sites (TSS ±3.0 kb). Top: Average signal density across all genes in (i) Medium, (ii) Estradiol (E_2), and (iii) E_2 + Aspirin conditions. Bottom: Heatmap of normalized ChIP-seq signals (z-score) at individual TSS regions. **(B-C)** IGV screen shots showing ERα binding sites in relation to the TSS of **(B)** *HMGN2* and **(C)** *TIMM8B* between three groups.

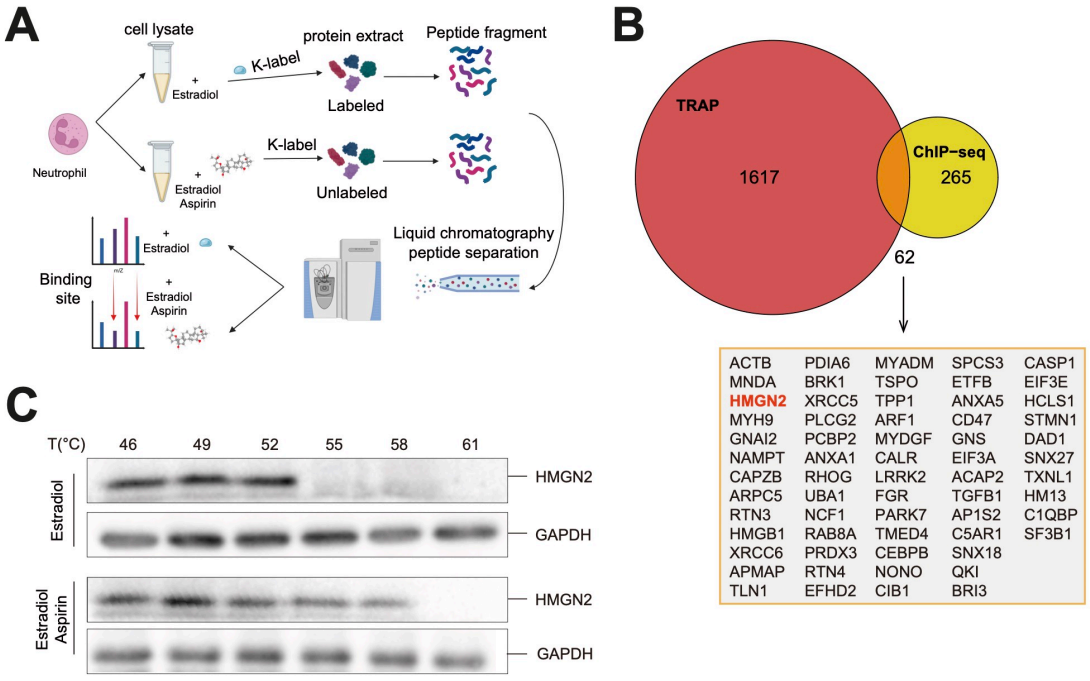


Fig. S25. Aspirin binds to HMGN2 protein. Related to Figure 6.

(A) Schematic representation of the TRAP experiment. The neutrophils from peripheral blood of human were incubated with 50 nM estradiol or medium at 37°C for 2 h. The MPO level in the cell supernatant was measured. The TRAP experiment was conducted. **(B)** The Venn diagram shows the merge of Trap and ChIP-seq results. **(C)** The neutrophils from peripheral blood of human were incubated with estradiol or estradiol+Aspirin for 24 h, and the

cellular thermal shift assays (CETSA) analyzed the thermal stabilization of HMGN2 protein at different temperatures.

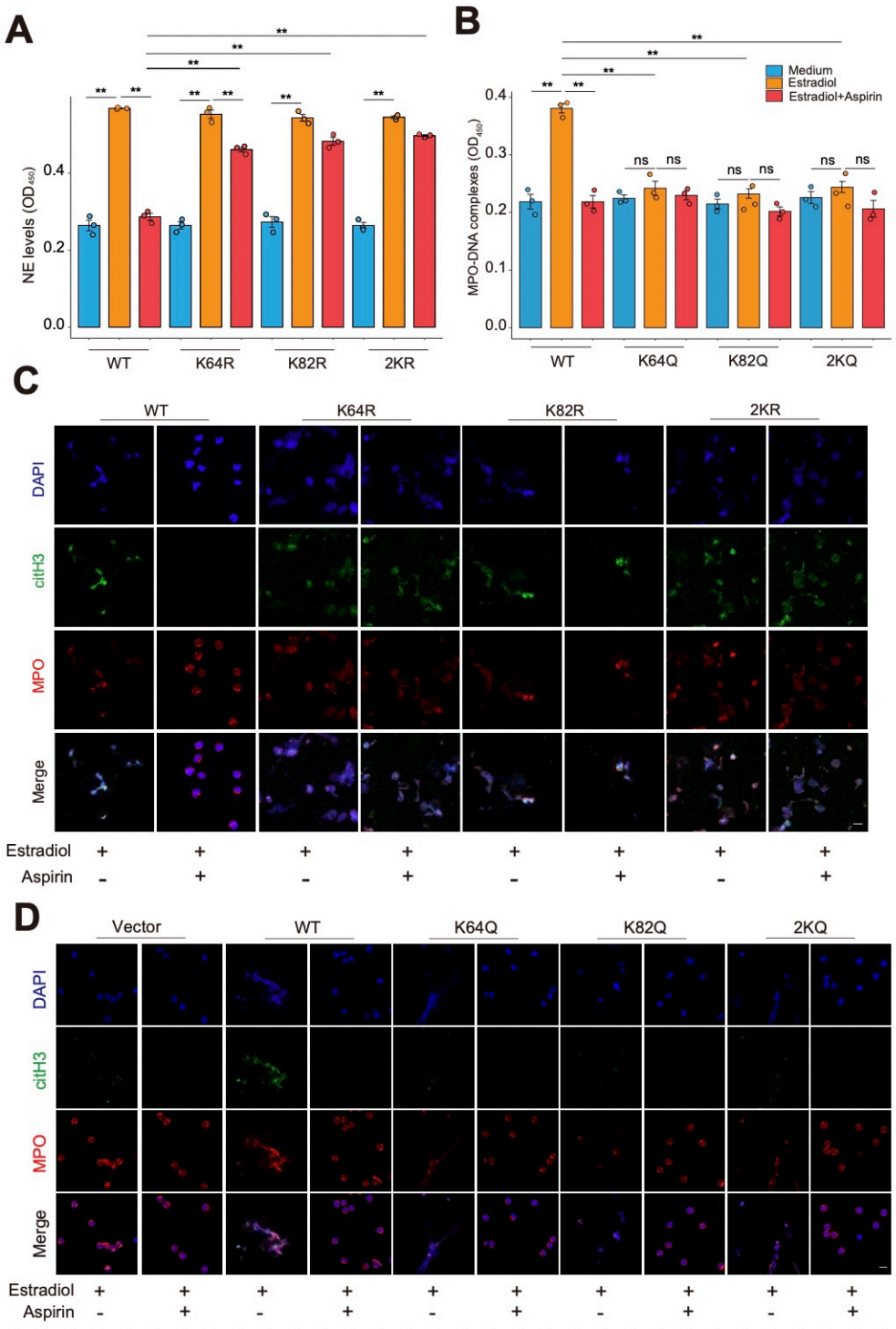


Fig. S26. Aspirin inhibits NET formation by acetylating HMGN2 at K64 and K82. Related to Figure 6.

A) HL60 cells transfected with the indicated constructs were treated with estradiol (50 nM) or aspirin (5 μM) for 2 h. OD_{450} value reflects the level of NE in lysates, **P*<0.05, ***P*<0.01. **(B)** HL60 cells transfected with the indicated constructs were treated with estradiol or aspirin for 2 h. OD_{450} value reflects the level of MPO-DNA complexes in lysates, **P*<0.05, ***P*<0.01. **(C)** HL60 cells transfected with the indicated constructs were treated with estradiol (50 nM) or aspirin (5 μM) for 2 h. HL60 cells were stained with citH3 (green), MPO (red) and DAPI (blue). Scale bar: 10 μm. **(D)** HL60 cells transfected with the indicated constructs were treated with estradiol or aspirin for 2 h. HL60

cells were stained with citH3 (green), MPO (red) and DAPI (blue). Scale bar: 10 μm.

Supplementary Video 1. Dynamic changes of NETs formation from WT and *Esr1* KO mice in response to estrogen.

The neutrophils were isolated from wild-type or *Esr1* knockout mice. The neutrophils were stimulated with estradiol and imaged for 6 h and stained with Draq5 (red, 2 μM) and Sytox Green (green, 1μM).

Supplementary Video 2. Dynamic changes of NETs formation from WT and *Hmgn2* KO mice in response to estrogen.

The neutrophils were isolated from wild-type or *Hmgn2* knockout mice. The neutrophils were stimulated with estradiol and imaged for 6 h and stained with Draq5 (red, 2μM) and Sytox Green (green, 1μM).

Supplementary Video 3. The effect of Aspirin on dynamic changes of NETs formation in response to estrogen.

The neutrophils were isolated from human. The neutrophils were stimulated with estradiol or 5 uM Aspirin and imaged for 6 h and stained with Draq5 (red, 2μM) and Sytox Green (green, 1μM).

Supplementary Table 1. Information of human samples

Name	Age	sample	Experiment	Operation time
Donor-1	48	Normal endometrial (proliferative phases)	scRNA-seq	2024.09.18
Donor-2	43	Normal endometrial (proliferative phases)	scRNA-seq	2024.09.18
Donor-3	33	Normal endometrial (proliferative phases)	scRNA-seq	2024.09.18
Donor-4	50	Normal endometrial (proliferative phases)	scRNA-seq	2024.09.04
Donor-5	32	Normal endometrial (secretory phases)	scRNA-seq	2024.09.30
Donor-6	49	Normal endometrial (proliferative phases)	scRNA-seq	2024.08.06
Patient-1	35	Endometrial hyperplasia (simple hyperplasia)	scRNA-seq	2024.09.16
Patient-2	49	Endometrial hyperplasia (simple hyperplasia)	scRNA-seq	2024.09.19
Patient-3	35	Endometrial hyperplasia (simple hyperplasia)	scRNA-seq	2024.09.20
Patient-4	48	Endometrial hyperplasia (simple hyperplasia)	scRNA-seq	2024.09.12
Patient-5	31	Endometrial hyperplasia (simple hyperplasia)	scRNA-seq	2024.09.11

Patient-6	47	Endometrial hyperplasia (simple hyperplasia)	scRNA-seq	2024.09.26
Patient-7	35	Endometrial hyperplasia (simple hyperplasia)	scRNA-seq	2024.10.09
Patient-8	30	Endometrial hyperplasia (simple hyperplasia)	scRNA-seq	2024.09.18
Patient-9	35	Endometrial hyperplasia (simple hyperplasia)	scRNA-seq	2024.09.11
Patient-10	45	Endometrial hyperplasia (simple hyperplasia)	scRNA-seq	2024.10.07
Patient-11	49	Endometritis ($CD138^+$)	scRNA-seq	2024.08.28
Patient-12	34	Endometritis ($CD138^+$)	scRNA-seq	2024.08.12
Patient-13	36	Endometritis ($CD138^+$)	scRNA-seq	2024.08.12
Patient-14	35	Endometritis ($CD138^+$)	scRNA-seq	2024.07.26
Patient-15	25	Endometritis ($CD138^+$)	scRNA-seq	2024.10.07
Patient-16	44	Endometritis ($CD138^+$)	scRNA-seq	2024.08.07
Patient-17	44	Endometritis ($CD138^+$)	scRNA-seq	2024.08.07
Patient-18	37	Endometritis ($CD138^+$)	scRNA-seq	2024.08.07
Donor-7	49	Normal endometrial (Non-menstrual phase)	scATAC-seq	2020.11.09
Donor-8	53	Normal endometrial (Non-menstrual phase)	scATAC-seq	2021.04.09
Donor-9	45	Normal endometrial (Non-menstrual phase)	scATAC-seq	2020.05.14
Donor-10	45	Normal endometrial (Non-menstrual phase)	scATAC-seq	2021.04.29
Patient-19	53	Endometrial hyperplasia (simple hyperplasia)	scATAC-seq	2019.12.31
Patient-20	46	Endometrial hyperplasia (simple hyperplasia)	scATAC-seq	2020.01.22
Patient-21	54	Endometritis	scATAC-seq	2021.05.13
Patient-22	31	Endometritis	scATAC-seq	2020.12.30
Patient-23	38	Endometrial hyperplasia (simple hyperplasia)	ST-seq	2020.11.23
Patient-24	46	Endometrial hyperplasia (simple hyperplasia)	ST-seq	2020.01.22

Patient-25	44	Endometrial hyperplasia (simple hyperplasia)	ST-seq	2020.10.30
Donor-23	49	Normal endometrial (proliferative phases)	ST-seq	2020.11.09
Donor-24	45	Normal endometrial (proliferative phases)	ST-seq	2021.04.29
Donor-25	53	Normal endometrial (proliferative phases)	ST-seq	2021.04.09
Patient-26	48	Endometritis ($CD138^+$)	CITE-seq	2024.04.01
Patient-27	36	Endometritis ($CD138^+$)	CITE-seq	2024.04.03
Patient-28	52	Endometritis ($CD138^+$)	CITE-seq	2024.03.27
Patient-29	24	Endometritis ($CD138^+$)	CITE-seq	2024.04.09
Patient-30	52	Endometritis ($CD138^+$)	CITE-seq	2024.04.03
Patient-31	42	Endometrial hyperplasia (simple hyperplasia)	CITE-seq	2024.04.11
Patient-32	47	Endometrial hyperplasia (simple hyperplasia)	CITE-seq	2024.03.07
Patient-33	52	Endometrial hyperplasia (simple hyperplasia)	CITE-seq	2024.04.26
Patient-34	34	Endometrial hyperplasia (simple hyperplasia)	CITE-seq	2024.04.03
Patient-35	49	Endometrial hyperplasia (simple hyperplasia)	CITE-seq	2024.04.02
Donor-14	51	Normal endometrial (proliferative phases)	CITE-seq	2024.03.12
Donor-15	41	Normal endometrial (proliferative phases)	CITE-seq	2024.04.30
Donor-16	26	Normal endometrial (proliferative phases)	CITE-seq	2024.03.29
Donor-17	32	Normal endometrial (proliferative phases)	CITE-seq	2024.03.29
Donor-18	41	Normal endometrial (proliferative phases)	CITE-seq	2024.04.01

1597

Supplementary Table 2. Antibodies and reagents used in this study.

REAGENT or RESOURCE	SOURCE	CAT number
Antibodies		
Rabbit polyclonal anti-NKCC1	Abcam	ab140986
Mouse monoclonal anti-myeloperoxidase	Abcam	ab90810
Rabbit monoclonal anti-myeloperoxidase	Abcam	ab208670
Rabbit monoclonal anti-CD45	Abcam	ab40763
Mouse monoclonal anti-β-actin	Abmart	M20011
Rabbit polyclonal anti-SLC12A2	Affinity Biosciences	DF2245
Rabbit polyclonal anti-neutrophil elastase	Bioss	bs-6982R
Mouse monoclonal anti-CD15	Cell Signaling Technology	4774
Anti-MPO capture antibody	R&D System	DY3174
Mouse monoclonal anti-NKCC1	Santa Cruz Biotechnology	sc-514774
Mouse monoclonal anti-neutrophil elastase	Santa Cruz Biotechnology	sc-55549
Mouse monoclonal anti-PCNA	Santa Cruz Biotechnology	sc-56
Mouse monoclonal anti-ERα	Santa Cruz Biotechnology	sc-8005
Rabbit monoclonal anti-Estrogen Receptor alpha	Abcam	ab32063
Mouse monoclonal anti-Cyclin D1	Santa Cruz Biotechnology	sc-8396
Goat anti-Rabbit IgG (H+L) Highly Cross-Adsorbed Secondary Antibody, Alexa Fluor™ 488	Thermo Fisher Scientific	A11034

Goat anti-Mouse IgG (H+L) Highly Cross-Adsorbed Secondary Antibody, Alexa Fluor™ 555	Thermo Fisher Scientific	A21424
Anti mouse Ly6G (Clone: 1A8)	bioXcell	BE0075-1
Anti human/monkey CD20 (Clone: 2H7)	bioXcell	BE0075-1
Fixable viability dye eFlour506 (E506) - BV510	Invitrogen	65-0866-18
Anti-human CD45 (Clone: HI30) - BUV395	BD	563792
Anti-human CD3 (Clone: SK7) - BV786	BD	563800
Anti-human CD19 (Clone: HIB19) - PE	Biolegend	302208
Anti-human CD11b (Clone: ICFR44) - PECF594	BD	562399
Anti-human CD14 (Clone: M5E2) - BV605	Biolegend	301834
Anti-human CD66b (Clone: G10F5) - APC	Biolegend	305110
Anti-human CD56 (Clone: B159) - AF700	BD	557919
Anti-human CD24 (Clone: ML5) - BV711	Biolegend	311136
Anti-mouse CD45 (Clone: REA737) – BV510	Miltenyi Biotec	130-110-665
Anti-mouse CD45 (Clone: 30-F11) - APC-Cy7	Biolegend	103116
Anti-mouse CD3 (Clone: BM10-37) - FITC	BD	553061
Anti-mouse CD19 (Clone: 1D3) - BV650	BD	563235
Anti-mouse Nkp46 (Clone: 29A1.4) - APC	eBioscience	50-3351-82
Anti-mouse CD11b (Clone: M1/70) - PE-Cy7	Biolegend	101216
Anti-mouse Ly6G (Clone: 1A8) - PerCP-Cy5.5	BD	560602
Anti-mouse Ly6C (Clone: HK1.4) – BV785	Biolegend	128041

Anti-mouse CD24 (Clone: M1/69) - PE	Biolegend	101807
Anti-Histone H3 (citrulline R17)	Abcam	ab219407
Anti-Neutrophil Elastase antibody	Abcam	Ab254178
PCNA (PC10) Mouse mAb	Cell Signaling Technology	2586
Anti-Myeloperoxidase antibody	Abcam	Ab208670
HMGN2 (D9B9) XP® Rabbit mAb	Cell Signaling Technology	9437S
Rabbit monoclonal anti-HMGN2	Abcam	ab124997
Anti-human CD45 (Clone: 2D1) - FITC	Biolegend	368507
Anti-human CD15 (Clone: MMA) - eFluor™450	eBioscience	48-0158-42
AbSeq Immune Discovery Panel	Biolegend	625970
Anti-Human CD45 (Clone: HI30) - FITC	BD	560976
Anti-Human CD3 (Clone: UCHT1) - BV510	BD	563109
Anti-human CD19 (Clone: SJ25C1) - BV605	BD	562654
Anti-human CD14 (Clone: M5E2)	BD	561029
Anti-human CD16 (Clone: 3G8) - BV421	BD	562878
Anti-Human CD15 (Clone: HI98) - PerCP-Cy5.5	BD	560828
Anti-Human CD66b (Clone: G10F5) - PE	BD	561650
Anti-Human CD44 (Clone: G44-26) - APC	BD	560890
Anti-Human CD24 (Clone: ML5) - PE-Cy7	BD	561646
Mouse monoclonal anti-Ac-lysine	Santa Cruz Biotechnology	Sc-32268
E-Cadherin(24E10) Rabbit mAb	Cell Signaling Technology	3195S

Rabbit Polyclonal anti-NKCC1	Proteintech	13884-1-AP
Chemicals, Peptides, and Recombinant Proteins		
Myeloperoxidase Activity Assay kit	Abcam	ab105136
Cell Surface Protein Isolation Kit	Abcam	ab206998
DAPI	Beyotime	C1002
Biotin 3' End DNA Labeling Kit	Beyotime	D3106
Phosphate Buffered Saline (PBS)	Biological Industries	02-024-1ACS
LumiGLO® Reagent	Cell Signaling Technology	7003
QuicKey Pro Human Pg(Progesterone) ELISA Kit	Elabscience Biotechnology Co.,Ltd	E-OSEL-H0011
Human Neutrophil Isolation Kit	Haoyang Biology	LZS11131
Lipopolysaccharides	MedChemExpress	HY-D1056
Estradiol	MedChemExpress	HY-B0141
GSK484 hydrochloride	MedChemExpress	HY-100514
Cl-amidine hydrochloride	MedChemExpress	HY-100574A
Prostaglandin E2	MedChemExpress	HY-101952
Insulin (human)	MedChemExpress	HY-P0035
Aspirin	MedChemExpress	HY-14654
Multi Tissue Dissociation Kit 1	Miltenyi Biotec	130-110-201
Sodium Assay Kit	Nanjing Jiancheng Bioengineering Institute	C002-1-1
Chlorine Assay Kit	Nanjing Jiancheng Bioengineering Institute	C003-2-1

Potassium Assay Kit	Nanjing Jiancheng Bioengineering Institute	C001-2-1
IHC Detect Kit for Rabbit/Mouse Primary Antibody	Proteintech Group Inc	PK10006
Human Myeloperoxidase DuoSet ELISA	R&D System	DY3174
Mouse Myeloperoxidase DuoSet ELISA	R&D System	DY3667
Mouse Neutrophil Elastase/ELA2 DuoSet ELISA	R&D System	DY4517-05
Human Neutrophil Elastase/ELA2 DuoSet ELISA	R&D System	DY9167-05
Cell Death Detection ELISA kit	Roche	11544675001
Hematoxylin solution	Servicebio	G1005
Monkey estrogen ELISA kit	Shanghai Jianglai Biotechnology Co., Ltd	JL21806-96T
Olive oil	Solarbio life science	O8320
Quant-iT™ PicoGreen™ dsDNA Assay Kit	Thermo Fisher Scientific	P7589
Multiple immunofluorescence kit	Shang Hai GuduoBio Technology Co. Ltd	HYDS0045
Dnase I	Roche	10104159001
Elacestrant	MedChemExpress	HY-19822
Neutrophil Isolation Kit, mouse	Miltenyi Biotec	130-097-658
Recombinant Human protein HMG-17 (HMGN2)	CUSABIO	CSB-EP010570HU
Protein A/G	Proteintech	PR40025
Recombinant Human protein SLC12A2	MedChemExpress	HY-P702022
Bumetanide	MedChemExpress	HY-17468
Nuclear Green	Beyotime	C1181S

DRAQ5	MedChemExpress	HY-D1742

Supplementary Table 3. Antibodies of CITE-seq in this study.

Antibody	clone	Sequence ID	Identifier (RRID)
CD3	UCHT1	AHS0231	BD Biosciences Cat# 625970
CD4	SK3	AHS0032	BD Biosciences Cat# 625970
CD8	SK1	AHS0228	BD Biosciences Cat# 625970
CD11c	B-Ly6	AHS0056	BD Biosciences Cat# 625970
CD14	MPHIP9	AHS0037	BD Biosciences Cat# 625970
CD16	3G8	AHS0053	BD Biosciences Cat# 625970
CD19	SJ25C1	AHS0030	BD Biosciences Cat# 625970
CD25	2A3	AHS0026	BD Biosciences Cat# 625970
CD27	M-T271	AHS0025	BD Biosciences Cat# 625970
CD28	L293	AHS0138	BD Biosciences Cat# 625970
CD45RA	HI100	AHS0009	BD Biosciences Cat# 625970
CD56	NCAM16	AHS0019	BD Biosciences Cat# 625970
CD62L	DREG-56	AHS0049	BD Biosciences Cat# 625970
CD127	HIL-7R-M21	AHS0028	BD Biosciences Cat# 625970
CD134	ACT35	AHS0013	BD Biosciences Cat# 625970
CD137	4B4-1	AHS0003	BD Biosciences Cat# 625970
CD161	HP-3G10	AHS0205	BD Biosciences Cat# 625970
CD183(CXCR3)	1C6/CXCR3	AHS0031	BD Biosciences Cat# 625970
CD185(CXCR5)	RF8B2	AHS0039	BD Biosciences Cat# 625970
CD186(CXCR6)	13B 1E5	AHS0148	BD Biosciences Cat# 625970
CD196 (CCR6)	11A9	AHS0034	BD Biosciences Cat# 625970
CD197 (CCR7)	2-L1-A	AHS0273	BD Biosciences Cat# 625970
CD272	J168-540	AHS0052	BD Biosciences Cat# 625970
CD278	DX29	AHS0012	BD Biosciences Cat# 625970
CD279	EH12.1	AHS0014	BD Biosciences Cat# 625970
CD357 (GITR)	V27-580	AHS0104	BD Biosciences Cat# 625970
CD366(TIM-3)	7D3	AHS0016	BD Biosciences Cat# 625970
HLA-DR	G46-6	AHS0035	BD Biosciences Cat# 625970
IgD	IA6-2	AHS0058	BD Biosciences Cat# 625970
IgM	G20-127	AHS0198	BD Biosciences Cat# 625970
CD36	CLB-IVC7	AHS0135	BD Biosciences Cat# 940224
CD206	19.2	AHS0072	BD Biosciences Cat# 940068
CD32	FLI8.26	AHS0073	BD Biosciences Cat# 940069
CD69	FN50	AHS0010	BD Biosciences Cat# 940019
CD141	1A4	AHS0083	BD Biosciences Cat# 940079
CD43	1G10	AHS0200	BD Biosciences Cat# 940278
CD102	CBR-IC2/2	AHS0155	BD Biosciences Cat# 940241
CD110	1.6.1	AHS0225	BD Biosciences Cat# 940302
CD140a	αR1	AHS0160	BD Biosciences Cat# 940246
CD59	p282 (H19)	AHS0224	BD Biosciences Cat# 940301

CD15	W6D3	AHS0196	BD Biosciences Cat# 940274
CD66	B1.1/CD66	AHS0094	BD Biosciences Cat# 940088

Supplementary Files

This is a list of supplementary files associated with this preprint. Click to download.

- NCResponseletter.pdf
- SupplementaryVideo3.mp4
- SupplementaryVideo1.mp4
- SupplementaryVideo2.mp4
- uncroppedGelsandBlotsimage.pdf
- SourcedatafileNCOMMS26085788.xlsx
- Quetal.reportingsummaryNCOMMS26085788.pdf